Thermodynamic Analysis and Numerical Modeling of Supercritical Injection

A thesis accepted by the Faculty of Aerospace Engineering and Geodesy of the Universität Stuttgart in partial fulfillment of the requirements for the degree of Doctor of Engineering Sciences (Dr.-Ing.)

by

Dipl.-Ing. Daniel Banuti

born in Marl

Committee chair:	Prof. Dr.-Ing. habil. Bernhard Weigand
Committee member:	Prof. Dr. rer. nat. Michael Pfitzner
Committee member:	Prof. Dr.-Ing. Klaus Hannemann
Date of defence:	November 25, 2014

Institute of Aerospace Thermodynamics
University of Stuttgart
2015

Acknowledgments

First, I would like to thank the members of the committee: my thesis supervisor Prof. Dr.-Ing. habil. Bernhard Weigand, for his support and for sowing the seed of doubt and asking critical questions at a critical time - which led to a much deepened understanding of the topic; Prof. Dr. rer. nat. Michael Pfitzner, for agreeing to be in the committee and for the valuable comments; Prof. Dr.-Ing. Klaus Hannemann, for providing the opportunity to work on this topic at the German Aerospace Center (DLR) in Göttingen, and for complete scientific freedom during this time; Prof. Dr. rer. nat. habil. Claus-Dieter Munz for chairing the examination panel.

I wish to acknowledge the support of all of my colleagues at DLR, but some deserve special mention. I am indebted to Javier Bartolomé Calvo for the foundation he laid and for guiding me towards real gas thermodynamics. I am grateful for the support I received from Volker Hannemann and Sebastian Karl, for providing insight to TAU, for always having time for discussions and for always being eager to help. Thank you Scott Beinke, fearless and stubborn PhD student, for pushing the model beyond my wildest dreams and encountering bugs beyond your wildest nightmares. I wish I could have provided you something better much faster. I am grateful for the discussions with and the support I received from Michael Oschwald. For proofreading of the thesis I would like to thank Rolf-Detlef Boettcher, Volker Hannemann, Sebastian Karl, and Martin Grabe. I would like to thank Jean-Pierre Hickey, whom I met too late to help me with my thesis, but who was there afterwards for productive discussions.

The cooperation with Airbus DS led to tough discussions and invaluable insight, for this I would like to thank particularly Manuel Frey and Blazenko Ivancic. I would like to thank Matthieu Masquelet, for having provided a pointer towards the 'Widom-line' - without ever having met! The hint turned out to be very fruitful and grew to become a central part of this thesis. I would like to express my very great appreciation to Gary Flandro, for teaching to keep the mind open and for preaching the scientific method. Thank you Lutz Blätte, for unintentionally helping me overcome the midthesis crisis by pointing me towards some royal skillness. I would like to thank the

band in the basement, Silvia Reuß, Martin Grabe, Sebastian Karl, for providing balance, fun, and beer, and for introducing me to my later wife. Sind wir etwa schneller geworden?

Finally, I want to express my gratitude towards my family, who was always there for me. My mother, Silvia Banuti, who made me the person I am today. She taught me the perseverance and spirit needed to finish this dissertation. Ich wünschte, Du wärst bei meiner Verteidigung dabeigewesen. My father Wolfgang Wallukat, who sparked my fascination with everything space and watched me to grow up to actually work in this field. Vielen Dank Oma Christa und Tante Ada für alles. Ich glaube, ich habe Euch nicht erklären können, was ich eigentlich arbeite, aber ich denke, Ihr seid zumindest froh, daß mich das jemand machen läßt! I am forever indebted to my wonderful wife Sophie, for all the support and the patience she had (and still has) with me. I am incredibly happy that my son Max is here now, a little stubborn researcher of his own.

Ultimately, two persons which were there when I started this thesis did not live to see its end: my mother Silvia Banuti and my colleague Rolf-Detlef Boettcher. On the other hand, there are three people more in my life whom I did not know when I started: my wife Sophie, my son Max, and a third person I am really looking forward to meeting in June! C'est la vie.

Daniel Banuti

Göttingen,
Friday, 13 February 2015

Contents

List of Figures

List of Tables

Nomenclature

Acronyms & Abbreviations

AFRL	Air Force research laboratory
AUSM	Advection upstream splitting method
BWR	Benedict-Webb-Rubin (EOS)
CARS	Coherent anti-Stokes Raman spectroscopy
CCD	Charge-coupled device
CFD	Computational fluid dynamics
CSP	Corresponding states principle
DNS	Direct numerical simulation
DLR	Deutsches Zentrum für Luft- und Raumfahrt (German Aerospace Center)
ECS	Extended corresponding states principle
EOS	Equation of state
GH2	Gaseous hydrogen
GOX	Gaseous oxygen
LES	Large eddy simulation
LOX	Liquid (-like) oxygen
LRE	Liquid propellant rocket engine
MBWR	Modified Benedict-Webb-Rubin (EOS)
MFM	Multi fluid mixing
PDF	Probability density function
PR	Peng-Robinson (EOS)
RANS	Reynolds averaged Navier-Stokes equations
RK	Redlich-Kwong (EOS)
scramjet	Supersonic combustion ramjet
SEE	Statistical Eulerian Eulerian
SEL	Statistical Eulerian Lagrangian
SFM	Single fluid mixing
SOS	Speed of sound
SRK	Soave-Redlich-Kwong (EOS)
TAU	DLR's Navier-Stokes flow solver
URANS	Unsteady Reynolds averaged Navier-Stokes equations
vdW	van der Waals (EOS or mixing rule)

Roman Symbols

a	speed of sound	m/s
	attractive potential EOS parameter	$m^5/(s^2kg)$
A	area	m^2
	Widom equation parameter	-
b	molecular volume EOS parameter	m^3/kg
B	pseudo-boiling parameter	-
B_n	virial coefficient	$(kg/m^3)^n$
c_p	isobaric specific heat capacity	J/(kgK)
c_c	isochoric specific heat capacity	J/(kgK)
C	generic constant parameter	/
D	diameter	m
e	specific inner energy	J/kg
E	TAU: specific total inner energy	J/kg
F	thrust	N
$\vec{F}$	flux vector	/
g	specific Gibbs free enthalpy	J/kg
	gravitational acceleration	$9.81\ m/s^2$
h	specific enthalpy	J/kg
H	enthalpy	J
H	TAU: specific total enthalpy	J/kg
$\dot{H}$	enthalpy flow	J/s
$\overline{\overline{I}}$	identity matrix	-
I_{sp}	specific impulse	s
J	momentum flux ratio	-
$\mathcal{M}$	molar mass	kg/mol
k	binary interaction parameter	-
	thermal conductivity	W/(mK)
	reaction rate	$m^3/mol;\ m^9/mol^2$
K	equilibrium constant	-
L	length	m
m	mass	kg
$\dot{m}$	mass flow	kg/s
N	number of time steps	-
N_A	Avogadro's number	6.022e+23 1/mol
p	pressure	Pa
$\overline{\overline{P}}$	viscous stress tensor	/
$\dot{q}$	volumetric heat addition rate	W/m^3
Q	heat	J

$\dot{Q}$	heat addition rate	W
Q_s	partition function	-
$\mathscr{R}$	universal gas constant	8314.46 J/(molK)
R	specific gas constant, $R = \mathscr{R}/\mathscr{M}$	J/(kgK)
s	specific entropy	J/(kgK)
$\vec{S}$	source term vector	/
t	time	s
T	temperature	K
u	velocity	m/s
U	inner energy	J
$\vec{U}$	vector of conservative variables	/
v	specific volume	m^3/kg
V	volume	m^3
x	molar concentration	mol/m^3
X	coordinate	m
X	species	-
y	mole fraction	-
Z	real gas factor	-
	coordinate	m

Superscripts and subscripts

+	upper bound
−	lower bound
0	reference
	reservoir (total) conditions
∞	farfield
act	actual
b	backward reaction
boundary	at numerical boundary (condition)
bu	break-up
C	core
cell	in computational cell
cr	critical point
eq	equilibrium
exit	value at nozzle exit
f	forward reaction
G	gaseous
i	species index for mixing
iG	ideal gas

in	in, injected, injection
int	integrated
inv	inviscid
j	species index for mixing
k	iteration counter
l	lower/left boundary
L	liquid
loss	loss
max	maximum
min	minimum
n	time step index / species index
nom	nominal
pb	pseudo-boiling
p	isobaric
r	reduced: divided by critical value
	upper/right boundary
	reaction
rel	relative
rG	real gas
s	species index
sat	saturation
st	structural, i.e. concerning intermolecular attraction
supplied	supplied
T	isothermal
th	thermal, i.e. heating
visc	viscous
v	isochoric
V	vapor

Greek symbols

α	attractive potential EOS parameter	$m^5/(s^2kg)$
	reactant stoichiometric coefficient	-
β	product stoichiometric coefficient	-
γ	ratio of specific heats	-
δ	LOX post thickness	m
	LOX injector diameter	m
θ	characteristic temperature	K
μ	dynamic viscosity	Pa s
ρ	density	kg/m^3
σ	surface tension	N/m
ω	Pitzer's acentric factor	–
ω_s	chemical source term	$kg/(m^3s)$

Abstract

Although liquid propellant rocket engines are operational and have been studied for decades, cryogenic injection at supercritical pressures is still considered essentially not understood. This thesis intends to approach this problem in three steps: by developing a numerical model for real gas thermodynamics, by extending the present thermodynamic view of supercritical injection, and finally by applying these methods to the analysis of injection.

A new numerical real gas thermodynamics model is developed as an extension of the DLR TAU code. Its main differences to state-of-the-art methods are the use of a precomputed library for fluid properties and an innovative multi-fluid-mixing approach. This results in a number of advantages: There is effectively no runtime penalty of using a real gas model compared to perfect gas formulations, even for high fidelity equations of state (EOS) with associated high computational cost. A dedicated EOS may be used for *each* species. The model covers all fluid states of the real gas component, including liquid, gaseous, and supercritical states, as well as liquid-vapor mixtures. Numerical behavior is not affected by local fluid properties, such as diverging heat capacities at the critical point. The new method implicitly contains a vaporization and condensation model. In this thesis, oxygen is modeled using a modified Benedict-Webb-Rubin equation of state, all other involved species are treated as perfect gases.

A quantitative analysis of the supercritical pseudo-boiling phenomenon is given. The transition between supercritical liquid-like and gas-like states resembles subcritical vaporization and is thus called pseudo-boiling in the literature. In this work it is shown that pseudo-boiling differs from its subcritical counterpart in that heating occurs simultaneously to overcoming molecular attraction. In this process, the dividing line between liquid-like and gas-like, the so called Widom line, is crossed. This demarcation is characterized by the set of states with maximum specific heat capacity. An equation is introduced for this line which is more accurate than previous equations. By analyzing the Clausius-Clapeyron equation towards the critical limit, an expression is derived for its sole parameter. A new nondimensional parameter evaluates the ratio of overcoming molecular attraction to heating: It

diverges towards the critical point but shows a significant pseudo-boiling effect for up to reduced pressures of 2.5 for various fluids.

It appears reasonable to interpret the Widom-line, which divides liquid-like from gas-like supercritical states, as a definition of the boundary of a dense supercritical fluid. This may be used to uniquely determine the radius of a droplet or the dense core length of a jet. Then, a quantitative thermodynamic analysis is possible. Furthermore, as the pseudo-boiling process may occur during moderate heat addition, this allows for a previously undescribed thermal jet disintegration mechanism which may take place within the injector.

This thermal jet break-up hypothesis is then applied to an analysis of Mayer's and Branam's nitrogen injection experiments. Instead of the constant density cores as predicted by theory, the majority of their cases show an immediate drop in density upon entering the chamber. Here, three different axial density modes are identified. The analysis showed that heat transfer did in fact take place in the injector. The two cases exhibiting a dense core are the cases which require the largest amount of power to reach the pseudo-boiling temperature. After this promising application of pseudo-boiling analysis, thermal break-up is tested numerically. By accounting for heat transfer inside the injector, a non dense-core injection can indeed be simulated for the first time with CFD.

Finally, the CFD model is applied to the A60 Mascotte test case, a reactive GH2/LOX single injector operating at supercritical pressure. The results are compared with experimental and other researcher's numerical data. The flame shape lies well within the margins of other CFD results. Maximum OH* concentration is found in the shear layer close to the oxygen core and not in the shoulder, in agreement with experimental data. The axial temperature distribution is matched very well, particularly concerning position and value of the maximum temperature.

Zusammenfassung

Obwohl Flüssigtreibstoffraketen bereits seit Jahrzehnten im Einsatz und Gegenstand umfangreicher Untersuchungen sind, gilt die Einspritzung kryogener Treibstoffe bei überkritischen Drücken als im Wesentlichen nicht verstanden. In der vorliegenden Arbeit wird auf drei unterschiedlichen Wegen auf diese Problematik eingegangen: durch die Entwicklung eines neuartigen numerischen Modells der Realgasthermodynamik, durch die Erweiterung der thermodynamischen Beschreibung überkritischer Treibstoffeinspritzung, sowie durch die Anwendung dieser Ansätze zur Analyse von Einspritzvorgängen.

Ein neues numerisches Modell der Thermodynamik realer Gase wird als Erweiterung des TAU Codes des DLR vorgestellt. Es unterscheidet sich von etablierten Lösern hauptsächlich durch zwei Aspekte: Zum Einen werden Stoffdaten im Vorfeld einer Simulation statt zur Laufzeit berechnet und in einer Bibliothek dem Verfahren bereitgestellt. Zum Anderen ermöglicht ein neuentwickeltes Multi-Fluid Mischungsmodell die Abbildung der jeweiligen Stoffdaten mittels unterschiedlicher Zustandsgleichungen. Dies führt zu einer Reihe von Vorteilen gegenüber herkömmlichen Verfahren: Der Rechenbedarf bei Einsatz der neuen Realgasthermodynamik steigt praktisch nicht im Vergleich zur Idealgasthermodynamik, selbst bei Benutzung numerisch teurer, aufwendiger Zustandsgleichungen. Es ist möglich, speziesspezifisch optimierte Zustandsgleichungen zu verwenden. Das Modell bildet sämtliche Fluidzustände, wie flüssig, gasförmig, überkritisch, bis hin zu Mehrphasengemischen, ab. Das numerische Verhalten wird nicht durch den Fluidzustand, bspw. divergierende spezifische Wärmekapazitäten, beeinflußt. Phasenwechsel wie Verdampfung oder Kondensation werden implizit durch das Modell abgebildet. Im Rahmen dieser Arbeit wird beispielhaft Sauerstoff durch eine modifizierte Benedict-Webb-Rubin Zustandsgleichung beschrieben, alle anderen Spezies werden als ideale Gase betrachtet.

Eine quantitative Analyse des Übergangs von überkritischem flüssig- zu gasähnlichem Fluid, Pseudosieden (pseudo-boiling), wird vorgestellt. Es wird gezeigt, daß im Gegensatz zu echtem (unterkritischem) isobaren Sieden, bei dem zugeführte Energie der isothermen Überwindung von intermolekularen Anziehungskräften dient, beim Pseudosieden gleichzeitig eine Tem-

peraturerhöhung stattfindet. Für das Verhältnis der bei beiden Prozessen benötigten Energiemengen wird eine dimensionslose Kennzahl eingeführt und der Wert für eine Reihe von Stoffen bestimmt. Es kann gezeigt werden, daß bis zu einem reduzierten Druck von 2,5 die Überwindung der intermolekularen Anziehungskräfte einen signifikanten Beitrag erfordert. Überkritische flüssig- und gasähnliche Zustände werden durch die sogenannte Widom-Linie getrennt, die durch ein Maximum der spezifischen Wärmekapazität und des isobaren Ausdehnungskoeffizienten charakterisiert werden kann. Eine Gleichung für diese Widom Linie wird vorgeschlagen, ihr einziger Parameter wird aus einer Grenzbetrachtung der Clausius-Clapeyron-Gleichung gegen den kritischen Punkt als Stoffgröße bestimmt.

Es wird gezeigt, daß das Erreichen des Pseudosiedepunktes auf der Widom-Linie als zweckmäßige Definition der Grenzfläche eines überkritischen flüssigähnlichen Fluids betrachtet werden kann. Damit ist der Radius eines überkritischen Tropfens oder die Länge des dichten Potentialkerns eines überkritischen Freistrahls zusammen mit dem thermodynamischen Zustand eindeutig bestimmt, was eine quantitative Analyse ermöglicht. Da Pseudosieden bereits bei geringer Wärmezufuhr auftritt, deutet dies einen bislang nicht betrachteten thermischen Strahlzerfallsmechanismus an, der bereits im Injektor initiiert werden kann.

Diese Hypothese eines thermischen Strahlzerfalls wird durch Analyse der Experimente zur überkritischen Stickstoffeinspritzung von Mayer und Branam gestützt: In diesen Experimenten wurde in der Mehrzahl der untersuchten Fälle keine Region konstanter Dichte hinter dem Injektor gefunden, wie man es in Theorie und CFD erwartet. Stattdessen werden in der vorliegenden Arbeit drei unterschiedliche Dichteprofile identifiziert, ein dichter Kern liegt nur vor, wenn die zur Erreichen des Pseudosiedepunktes erforderliche Enthalpie groß ist. Eine exemplarische CFD Rechnung unter Berücksichtigung von Wärmeübergang im Injektor konnte erstmalig den im Experiment beobachteten Dichteabfall reproduzieren.

Abschließend wird das Modell auf den A60 Mascotte Testfall angewandt, bei dem kryogener Sauerstoff mit gasförmigem Wasserstoff bei überkritischem Druck verbrennt. Ein Vergleich mit experimentellen Daten zeigt, daß die maximale OH* Konzentration korrekt in der Scherschicht hinter dem Injektor bestimmt wird, die Flammenform liegt innerhalb der Variation von CFD Ergebnissen anderer Gruppen. Die Temperaturverteilung, insbesondere Betrag und Position des Maximums, zeigt eine sehr gute Übereinstimmung mit dem Experiment.

" Is rocket propulsion therefore absolutely impossible because one cannot move the center of mass? No; but of course we find that to propel an interesting part of the rocket, an uninteresting part must be thrown away."

— Richard P. Feynman, *Lectures on Physics*

1 Introduction

1.1 A New Era in Spaceflight

A new era in spaceflight has begun. What used to be an endeavor of nations, is now achieved by private companies. When the first man-made object, the A4 rocket, reached space in 1942[1], it was supported by a nationwide war time research program. Sputnik, the first man-made object to orbit the earth in 1957[2], marked the Soviet Union's head start in the space race of the Cold War. The USA ultimately managed to win the race with the gigantic Apollo program, landing two astronauts on the moon in 1969[3]. Fast forward to 2004: Burt Rutan's SpaceShipOne[4] is the first commercial aircraft to cross the boundary of space, reaching Mach 3 while doing so. The first commercial object to orbit the earth (and to reenter earth atmosphere afterwards) is Elon Musk's Dragon Capsule[5] in 2010. Only two years later[6], it is the first commercial capsule to dock with the International Space Station. Both developments have been funded by people with no background in rocketry but who made money in the computer industry first: Microsoft's Paul Allen invested in the development of SpaceShipOne; PayPal's Elon Musk founded the rocket company SpaceX. Both endeavors have been able to commercialize on their developments in the meantime, selling flight tickets and satellite launches. They do not lack ambition either: ultimately, the goal of Musk's SpaceX is to establish settlements on other planets.

Whether the companies of the emerging private space industry will be able to advance the state of the art and to become economically successful remains to be seen. Nonetheless, they are the ones who took over developments that were prior only achievable by national efforts.

---

[1] October 3, 1942 - Aggregat 4 / V2
[2] October 4, 1957 USSR's Sputnik
[3] July 21, 1969, Neil Armstrong and Buzz Aldrin
[4] June 21, 2004 - Scaled Composites
[5] December 9, 2010 - SpaceX
[6] May 25, 2012 - SpaceX

1.2 Experiments and Models

All this would not have been possible without the groundbreaking work of the original pioneers. Hermann Oberth was ridiculed for his proposition of building a rocket into space just 20 years before the successful flight of the A4. Before his vision could be turned into reality, a lot of basic research was required. Designs based on theoretical approximations had to be tested extensively, new facilities needed to be invented and erected. Experiments, particularly on combustion chambers, remain difficult and expensive to this day. They remain dangerous - a failed engine test has cost the lives of two workers during the development of SpaceShipTwo, the successor to Rutan's SpaceShipOne. Finally, experiments have a slow turnaround time when it comes to testing and optimizing a multitude of configurations. With the advent of Computational Fluid Dynamics (CFD), i.e. simulation of flow phenomena, some of this work could be transferred to the computer. Physical processes can be modeled, insight into phenomena gained. The relationship between experiment and CFD is not a competition and beyond mere coexistence: during design, CFD is capable of rapid parameter studies; CFD can also serve to support experiments, helping to identify key questions to be answered. It can aid to analyze experimental results a posteriori: CFD provides full 3D access to all data where experiments are naturally limited by access to the facility and experimental methods. Ultimately, the experiment has the first and the final word; its results are required for validation of the CFD code.

1.2.1 Injection

All this is particularly true for the topic of this thesis: Injection of cryogenic propellants into high pressure rocket combustion chambers. Generally, the purpose of injection is to introduce the propellant into the combustion chamber. Side conditions encompass effective and efficient mixing, global mixture ratio, local mixture ratios (e.g. to achieve a film cooling effect near the wall), minimized stratification (e.g. homogeneous heat distribution over the cross section). To achieve this, a multitude of injectors has been developed, such as impinging jets, swirl, pintle, or coaxial injectors. Details can be found in textbooks such as Sutton and Biblarz [155] or Yang et al. [174]. Injectors have a particular importance as they are the last possibility to affect atomization and mixing directly. This thesis focuses on coaxial injectors, as can be found in typical cryogenic main stage engines such as the Space Shuttle Main Engine (SSME) or the European Vulcain2 engine of the Ariane 5

rocket. Figure 1.1 shows a schematic of such an injector. D_0 to D_3 are the different respective diameters, angle α denotes the taper, L_R is the recess length. For an injector without taper, $D_1 = D_0$. The LOX post thickness δ is $(D_2 - D_1)/2$. Cryogenic oxygen is injected through the center orifice, surrounded by a stream of gaseous hydrogen, GH2. For simplicity, cryogenic oxygen will be referred to as liquid oxygen, or LOX, regardless of whether the pressure is sub- or supercritical. In the Vulcain2 engine, 566 of these

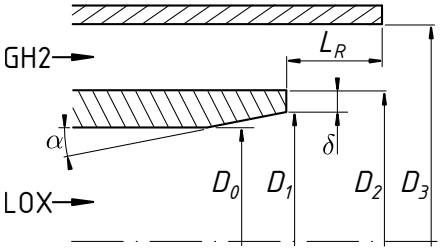

Figure 1.1: Coaxial injector.

coaxial injectors are combined into an injector plate, Fig. 1.2(a). The integration of the injector plate into the thrust chamber is shown in Fig. 1.2(b) for a Vulcain1 engine.

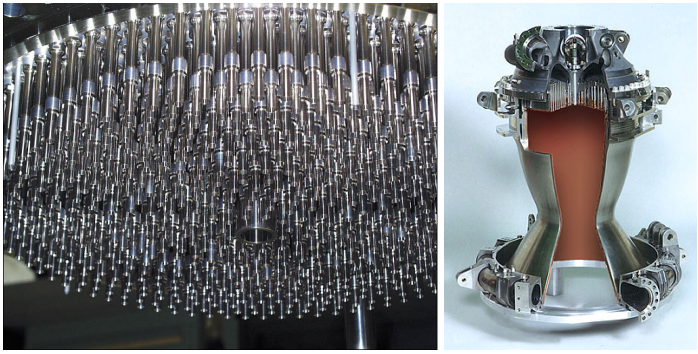

(a) Vulcain2 injector plate (Astrium GmbH [1]).

(b) Vulcain1 thrust chamber assembly (Astrium GmbH [2]).

Figure 1.2: Injector plate close-up (left) and in thrust chamber assembly (right).

1.2.2 Understanding and CFD

Experiments in high pressure, high temperature combustion chambers are extremely difficult. At temperatures exceeding 3600 K and pressures in excess of 10 MPa (Sutton and Biblarz [155]) one cannot simply insert a probe into the flow. Nonetheless, several break-through discoveries have been made in the last two decades, with profound impact on our view of injection. Not all phenomena are understood or even modeled. It is interesting to see how progress in experiments subsequently changed the image underlying the modeling.

1.2.3 Gas Combustor

In 1997, Schley and Hagemann from DLR, Tucker from NASA Marshall Space Flight Center, and Venkateswaran and Merkle from Penn State University published a paper concerned with the then state-of-the-art CFD prediction capabilities for rocket engines [141]. They noted certain difficulties in reaching a converged solution, such as numerically stiff chemistry, a low Mach number recirculation zone, an unspecified turbulence inflow boundary condition, and generally the lack of appropriate turbulence models. It was concluded that CFD single injector modeling is acceptable, as long as the flow field can be assumed axisymmetric. Ten years later, Tucker, Menon, Merkle, Oefelein, and Yang [160] applied their respective CFD codes again to the case of a single injector combustion chamber. Axisymmetry was no longer mandatory in terms of computational cost, contributions still cover RANS and URANS, but now reach up to unsteady LES on a 255 million point grid. However, with a range in fidelity between the applied models, the results showed a bigger variation than a decade before. Counterintuitively, the authors found that *"there was no monotonic convergence to the experimental data with respect to model fidelity."* I.e., LES did not systematically outperform URANS or even RANS computations. Furthermore, every single one of the problems identified ten years earlier was still an issue. Even worse: both papers are concerned with injection of *gaseous* hydrogen and *gaseous* oxygen only.

1.2.4 Lagrangian Multi Phase

In a liquid propellant rocket engine more complex phenomena take place. First attempts at visualization of processes inside a rocket combustion cham-

ber date back to early studies of combustion instabilities in the 1960s. The early cold flow liquid injection tests were carried out at subcritical pressures due to better accessibility. A report on the state of knowledge was compiled in the comprehensive NASA SP-194 by Harrje and Reardon in 1972 [60]. By 1994, subcritical injection had been studied to such an extent that it was reported to be essentially understood (Mayer and Tamura [102, 107], Villermaux [163]).

To that date, CFD models such as Astrium's ROCFLAM [174] had been designed based on the experience with low pressure liquid sprays: In 1998, Candel et al. [30] described cryogenic high pressure break up to be identical to liquid break up, with instabilities on the LOX surface forming ligaments, detaching as droplets and further disintegrating during secondary atomization. This view of break-up into individual Lagrangian particles is illustrated in Fig. 1.3. Bellan [18] reported in 2000 that most models of supercritical fluid injection had been designed for discrete droplets.

Figure 1.3: Liquid jet break-up into Lagrangian droplets.

Numerically, this is translated as follows: From an idealized liquid core, often a conical surface, particles are introduced into the gaseous carrier stream, see Fig. 1.4(a). The inflow boundary condition comprises a size and velocity distribution of injected droplets, often assumed or fitted to combustion data for inaccessible dense sprays (e.g. Babinsky and Sojka [10]). Once inside the computational domain, the movement of the individual particles is tracked between the cells, Fig. 1.4(b). The trajectory is determined by their inertia and external forces acting on them. The velocity difference between carrier phase and particle causes aerodynamic forces, Fig. 1.4(c). These lead to acceleration of the droplets and possibly further secondary atomization. Finally, as the droplet vaporizes, particle mass is decremented and added to the Eulerian carrier flow.

1.2.5 Eulerian Multi Phase

A first study of supercritical injection had been carried out by Newman and Brzustowski [114]. They described the break-up of a submerged supercritical carbon dioxide jet as a mixing rather than an atomization process. A vi-

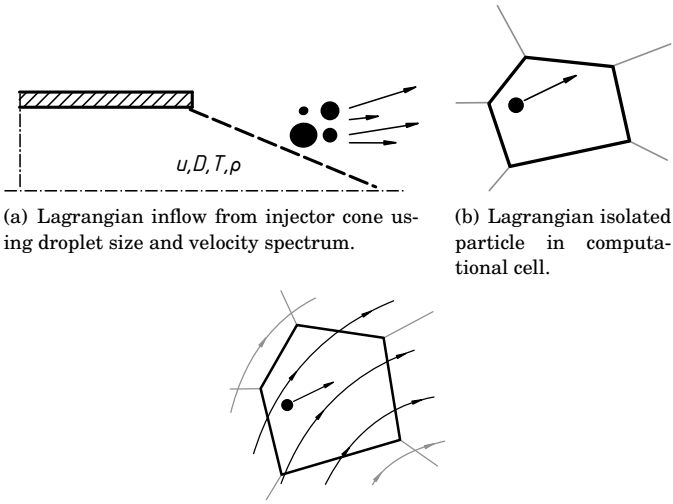

(a) Lagrangian inflow from injector cone using droplet size and velocity spectrum.

(b) Lagrangian isolated particle in computational cell.

(c) Lagrangian particle in carrier stream.

Figure 1.4: Numerical view of Lagrangian injection.

sualization of an experiment more representative for actual rocket engines, involving combustion and a coaxial injector, was still missing. Mayer and Tamura finally achieved this milestone in 1996 [107]. The experiments conducted at the German Aerospace Center (DLR) in Lampoldshausen, Germany, lead to a new understanding of cryogenic supercritical injection. Seventy years after the launch of the first liquid fueled rocket by Goddard, Mayer's and Tamura's seminal paper [107] revealed unexpected phenomena to be present in high pressure rocket combustion chambers. Figure 1.5 shows shadowgraphs of coaxial injection at three different pressures. For subcritical[7] injection they find that *"because of the rapid vaporization of droplets in a burning spray, the droplet number density is rather low compared to the cold flow case. Most of the droplets are non spherical."* Furthermore: *"In the cold flow case, fine oxidizer threads and droplets are visible. In the combusting case at low chamber pressures, the fine surface structures rapidly vaporize and droplets are never formed. No droplets can be observed in the vicinity of the injector."* For supercritical injection they found that *"upon approaching and exceeding supercritical pressure, droplets no longer exist. From the LOX jet core, schlieren- (stringy-) or thread-like structures develop and grow,*

[7] with respect to the critical pressure of oxygen

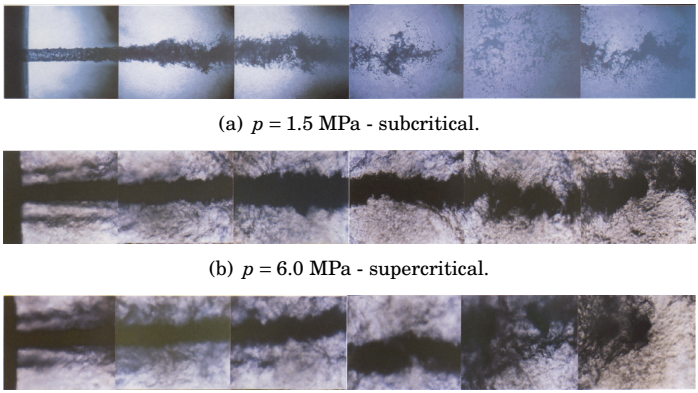

(a) $p = 1.5$ MPa - subcritical.

(b) $p = 6.0$ MPa - supercritical.

(c) $p = 10.0$ MPa - supercritical.

Figure 1.5: LOX break up region of LOX/GH2 coaxial injector at sub- and supercritical pressures (Mayer and Tamura [107]).

which do not detach, but rapidly dissolve and fade away. Several tens of jet diameters further downstream the LOX core breaks up into large LOX lumps, which dissolve in the same manner." Mayer and Tamura went on to describe the flame position: *"The interface between the propellants LOX and hydrogen is separated by a layer of reacting combustion gases. [...] The flame always attaches instantaneously after ignition at the LOX post. As indicated by the bright flame spot close to the LOX post tip, it seems that the strong recirculation zone behind the LOX post acts as a flameholder."*[8] Later, other researchers such as Bellan [18] supported the notion that injection at supercritical pressures resembles a turbulent mixing process much more than an atomization process.

To summarize, for both sub- and supercritical injection with combustion:

- Oxygen enters the chamber as a compact stream.
- No droplets are present in the vicinity of the injector. The stream breaks up into larger lumps several tens of diameters downstream of the injector.
- The break-up process resembles turbulent mixing rather than atomization.

[8] The photographs in Fig. 2.9 show this.

- The oxygen stream is effectively isolated from the hydrogen stream by the flame. The flame is anchored at the LOX post.

These experimental findings were justification enough to develop new numerical models which follow more closely the actual physical phenomena they are trying to describe. The acceptance of this change in understanding is perhaps best reflected in the shift of boundary conditions posed by the Rocket Combustion Modeling (RCM) workshops 2001 [56, 55] and 2006 [180, 164]. For the same configuration of a single injector combustion chamber (merely operated at a different oxidizer/fuel ratio) at supercritical pressures, the 2001 workshop specified a spectrum of oxygen droplets to be prescribed in the CFD calculation. Five years later, injection velocity and density were deemed appropriate injection boundary conditions. Only if the CFD solvers of the participants were incapable of representing the dense oxygen stream as a compact real gas phase should they resort to a *"simple representation"* of oxygen as disperse particles.

This new view of supercritical injection as a mixing process is visualized in Fig. 1.6. The velocity difference between the fast hydrogen and the slow cryogenic oxygen causes an unstable shear layer which will subsequently roll up. The numerical view is illustrated in Fig. 1.7. Fig. 1.7(a) shows how the fluid

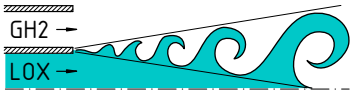

Figure 1.6: Injection and subsequent mixing of Eulerian continuum.

enters the computational domain characterized by the macroscopic variables velocity u, temperature T, density ρ. These are essentially the variables also controlled or measured in an experiment. Once inside the computational domain, the fluid is assumed to be a continuum, Fig. 1.7(b). Calculating the motion means to solve the Navier-Stokes equations that govern the flow.

Interestingly, not all of Mayer's findings have caught on. Exceptions are theoretical thermodynamic studies of mixing between hydrogen and oxygen, and studies of single droplet evaporation and combustion (Kuo [81], Oefelein and Yang [119], Yang [173]).

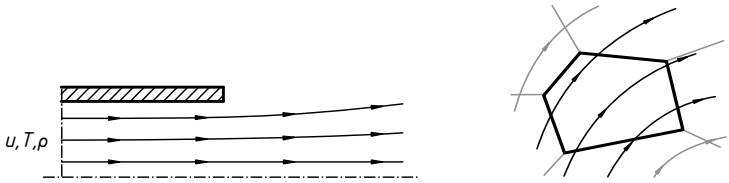

(a) Eulerian inflow from injector using physical fluid state and velocity.

(b) Eulerian continuous field.

Figure 1.7: Numerical view of Eulerian injection.

Name	T_{cr} in K	p_{cr} in MPa	ρ_{cr} in kg/m^3
Hydrogen	33.15	1.315	30.12
Nitrogen	126.19	3.396	313.28
Oxygen	154.60	5.043	436.11
Methane	190.56	4.592	162.65
Water	647.10	22.064	312.96

Table 1.1: Fluid properties at the critical point (Baehr and Kabelac [11]).

1.2.6 Eulerian Real Gas

Gas-gas combustors can be treated using an ideal gas equation to model the fluid's thermodynamic states. Liquids are typically assumed to have a constant density. None of these simplifications applies to supercritical fluids as encountered in rocket main stage engines. Critical properties for some species are compiled in Tab. 1.1. Oxygen and hydrogen are the typical propellants in main stage engines, nitrogen is often used as an oxygen substitute in inert experiments, water is the combustion product, methane is an alternative fuel.

Figure 1.8 shows how density changes with temperature for oxygen, nitrogen, and hydrogen. Real gas properties are taken from the NIST [94] database for oxygen (Schmidt and Wagner [142]), nitrogen (Span et al. [152]), and hydrogen (Leachman et al. [89]). The pressure is 6 MPa, exceeding the critical pressure of all shown species. Solid lines denote real gas, dotted lines ideal gas properties. For temperatures below 400 K, the ideal gas law deviates from real gas behavior for nitrogen and oxygen, below 200 K, the differences are too big to be neglected. Hydrogen can be treated as an ideal

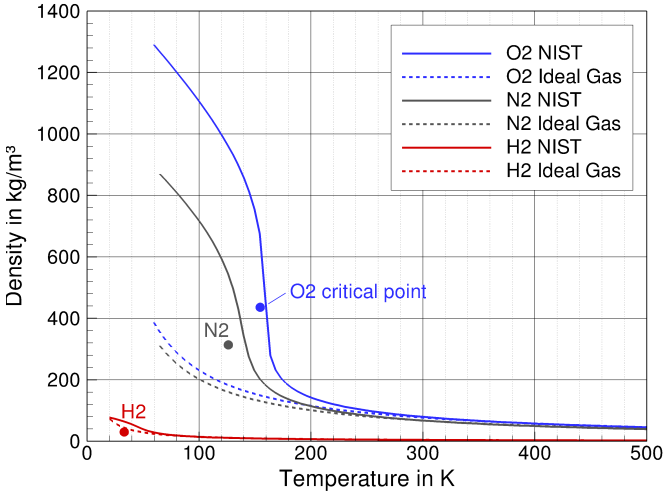

Figure 1.8: Ideal gas and real gas behavior (from the NIST database [94]) for oxygen, nitrogen, hydrogen at 6 MPa.

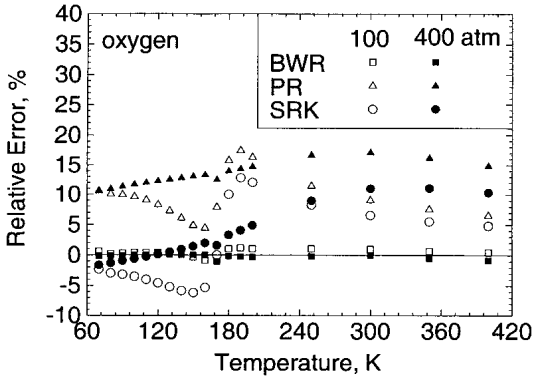

Figure 1.9: Density error made by SRK (Soave-Redlich-Kwong), PR (Peng-Robinson), and BWR (Benedict-Webb-Rubin) EOS, from Yang [173].

gas for temperatures higher than 100 K at this pressure.

In order to accurately treat fluid behavior at these states, i.e. high pressures and low temperatures, the perfect gas EOS is not sufficient anymore. Employing real gas equations of state has become mandatory - and state of the art. Typically, a representative equation of state for the mixture is determined by an approach called *single fluid mixing* (SFM). Evaluation during runtime makes numerical efficiency of the used equation important. Unfortunately, accuracy of the EOS is higher for more elaborate and thus more computationally costly EOS: Figure 1.9 compares errors in oxygen density for three different EOS[9]. The simple and most popular one, Peng-Robinson (PR), turns out to be the least accurate. Despite this, Masquelet et al. [99] reported that more than 20 % of CPU time in their model are required for evaluation of the PR EOS. On top of this, transport properties need to be computed.

It appears, one can either choose a numerically cheap *or* an accurate EOS.

[9] Equations of state will be discussed in more depth in Ch. 3.

1.3 Is something still missing?

Before numerically approaching the full complications encountered in a high pressure combustion chamber, it is desirable to study real gas injection in an isolated way first. Avoiding mixing and chemical reactions in a pure fluid case would allow this. Such a campaign was carried out by Mayer et al. [109] and Branam and Mayer [23]. In their experiments, cryogenic nitrogen at subcritical temperature was injected into a chamber filled with nitrogen at ambient temperature and supercritical pressure. Measurements of axial and radial density profiles and shadowgraphs were published for a test matrix of 4 MPa, 5 MPa, and 6 MPa chamber pressure, 100 K, 120 K, and 130 K injection temperature at 5 m/s and 2 m/s injection velocity. Analysis was carried out in terms of jet spreading angle and liquid core length. Figure 1.10 shows a compilation of all published axial density data.

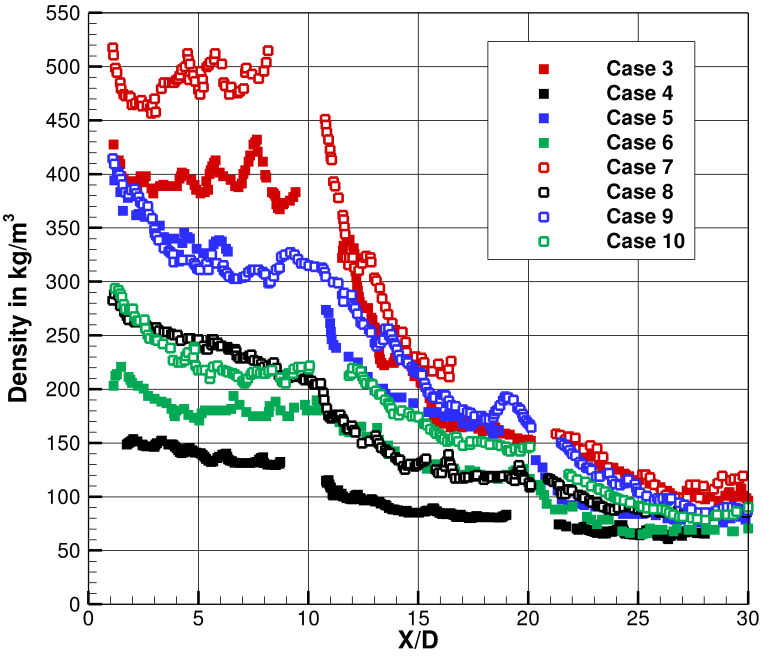

Figure 1.10: Axial density distributions of nitrogen injection experiments by Mayer et al. [109] and Branam and Mayer [23]. Case numbering follows Mayer.

There is a problem: Of the eight published distributions, only two exhibit a constant density core as expected from theory and experience. This feature, sometimes called potential core or liquid core, can be found only in cases 3 and 7. For all other cases, density can be seen to drop off immediately after injection.

What could cause the density drop-off? Flash atomization due to dramatic pressure drop after injection can be ruled out because of the quasi-isobaric nature of the experiment. A mechanical atomization process based on shear cannot be responsible for an immediate destruction of a potential core, as shear layers need to develop and spread before eventually affecting the centerline of the stream. Cavitation is unlikely, as the necessary pressure drop will be balanced out in the long injector at the occurring low flow velocities. Mayer himself suggested an explanation for his findings: the test cases in which the fluid had been injected above a certain temperature associated with a peak in specific heat capacity seemed to exhibit short to negligible cores. It appeared to him that heat transfer did in fact take place within the injector. And not taking this into account in CFD may have led to erroneous results.

Without naming it, Mayer effectively suggested an alternative atomization mechanism at supercritical pressures: thermal atomization. But why would there be a difference beyond the critical point where no liquid and no gas exist, much less vaporization? Are we missing some physical effect here?

1.4 Outline

The aim of this work is threefold, namely to

- develop a real gas mixture model using a high quality equation of state without penalty to computational efficiency and implement it into the DLR TAU code,
- investigate the thermodynamic process of injection in the vicinity of the critical point, as encountered in liquid propellant rocket engines,
- analyze the density anomaly in Mayer's inert cryogenic injection experiments.

The thesis is organized as follows: Chapter 2 gives an overview of injection in rocket engines and its mechanical classification. Chapter 3 summarizes and discusses a literature study on the heterogeneous nature of supercritical fluid properties. This theoretical body of knowledge is then extended by an investigation of a supercritical analogue to the subcritical latent heat of vaporization. This phenomenon is called pseudo-boiling in the literature. Finally, implications for injection in LRE are discussed. Chapter 4 gives an introduction to the DLR TAU code, the baseline CFD code used for this thesis. Chapter 5 covers the development of the new real gas numerical model for TAU. It is introduced in a top-bottom approach. The Euler-Euler methodology is the framework for the extension. Within, the design of the thermodynamics architecture is discussed. This is basically the arrangement of flow of information between the individual thermodynamic functions which solve the posed problems in a unique and consistent manner, desirably in a numerically robust and efficient fashion. The multi fluid mixing model then describes in detail the inner workings of these individual thermodynamic functions. The design of the library itself again requires efficiency and robustness and is discussed afterwards. The chapter concludes with a verification and validation of the developed model. Finally, the application of the theoretical and the numerical models is presented in Ch. 6. It consists of an analysis of the Mayer experiment, using the new pseudo-boiling theory introduced in Ch. 3. Results are employed to carry out a numerical simulation of a thermal jet break-up mechanism where density drop-off is caused by injector heat flux. To show the potential of the numerical model, a reactive single injector testcase is computed.

2 Injection Phenomena

2.1 Rocket Engine Performance

Why are we dealing with high pressure injection at all? It turns out a simple thermodynamic analysis of rocket engine flow can yield technical guidelines for improvement. Before a technical assessment or even an optimization of a rocket engine can be carried out, it is necessary to define specific figures of merit (Sutton and Biblarz [155]). The rocket engine's most immediate, and ultimately desired, action is the creation of thrust

$$F = \dot{m} u_{\text{exit}} + A_{\text{exit}} (p_{\text{exit}} - p_{\infty}). \tag{2.1}$$

Two components constitute thrust: the ejection of mass $\dot{m}$ accelerated to speed u_{exit} and the pressure difference between the nozzle exit (p_{exit}) and the environment (p_{∞}) acting over the nozzle exit area A_{exit}. A global measure of efficiency can be defined which evaluates how much propellant flow[1] is required to reach a given thrust F. This figure of merit is called specific impulse,

$$I_{\text{sp}} = \frac{F}{\dot{m} g}. \tag{2.2}$$

A simple thermodynamic analysis can provide insight into how the I_{sp} of a rocket engine can be improved. An adapted nozzle ($p_{\infty} = p_{\text{exit}}$) yields maximum thrust (Sutton and Biblarz [155]). Inserting Eq. (2.1) into Eq. (2.2) for this case leads to

$$I_{\text{sp,max}} = \frac{u_{\text{exit,max}}}{g}. \tag{2.3}$$

Thus, in order to maximize the specific impulse, the exit velocity needs to be maximized. The enthalpy balance for expansion from a stagnant reservoir is

$$h_0 = h_{\text{exit}} + \frac{u_{\text{exit}}^2}{2}. \tag{2.4}$$

[1] Strictly, $\dot{m} g$ is a weight flow. However, the acceleration of gravity g has historically been added to eliminate different units of length, mass, etc. to reach the internationally unambiguous unit *second*.

In a perfect gas $h = c_p T$ with $c_p = (\gamma R)/(\gamma - 1)$ where R is the specific gas constant and γ the isentropic exponent of the gas. Considering complete expansion ($T_{\text{exit}} = 0$ K) yields

$$u_{\text{exit,max}} = \sqrt{\frac{2\gamma R}{\gamma - 1} T_0} = \sqrt{\frac{2\gamma}{\gamma - 1} \frac{p_0}{\rho_0}}. \tag{2.5}$$

and

$$I_{\text{sp,max}} = \frac{1}{g} \sqrt{\frac{2\gamma}{\gamma - 1} \frac{p_0}{\rho_0}}. \tag{2.6}$$

The simple analysis provides actual design guidelines. Eq. (2.6) shows that an increase in chamber pressure will lead to a more efficient engine. Furthermore, the exhaust gas needs to be as light as possible (while maintaining a high γ). This is why we are dealing with high pressure, hydrogen rich combustion in liquid propellant rocket engines.

2.2 Jet Break-Up

Jet break-up generally means the disintegration of the injected jet. The break-up of the initially connected stream is called primary, further break-up of detached structures is called secondary atomization. In this thesis, primary atomization is the main concern. Bellan [18] suggests different terminology to differentiate between sub- and supercritical injection. In the presence of a phase equilibrium, the process is commonly called atomization, the phase change is called vaporization. In its absence she suggests to use instead the terms disintegration and emission, respectively. Instead of emission, gasification will be used in this thesis.

2.2.1 Classification of Jet Break-Up

Single Round Jet

In a brief historical overview, Eggers [41] pointed out that Savart was the first to make a step towards a classification of liquid jet break-up in 1833 - by realizing that it was governed by specific natural laws and hence *could* be classified. It took almost another five decades before Rayleigh succeeded in deriving a quantitative description, using linear stability analysis [134]. This early work was mainly concerned with the simplest possible configuration, injection of a round liquid jet into a stagnant environment. It was extended over the years, today's understanding is summarized in Reitz' and Bracco's [137] classical diagram, Fig. 2.1(a). Visualizations are compiled in Fig. 2.1(b).

Canonically[2], four regimes are distinguished: (a) *Rayleigh* where the droplets are larger than the initial jet, (b) *first wind induced* where droplet size is of same order as the jet diameter, (c) *second wind induced* where surface instabilities and droplet shedding occur downstream of the injection plane, and (d) *atomization* where droplets shed right from the beginning. The four regimes are characterized by two independent parameters, the liquid (subscript L) Reynolds number

$$\mathrm{Re}_\mathrm{L} = \frac{\rho_\mathrm{L} u_\mathrm{L} D_0}{\mu_\mathrm{L}} \tag{2.7}$$

is the ratio between inertial and viscous forces. It is comprised of density ρ, speed u, viscosity μ, and a characteristic length such as the jet diameter D.

[2] E.g. see textbooks by Warnatz et al. [166], Kuo and Acharya [82], Brauer [25].

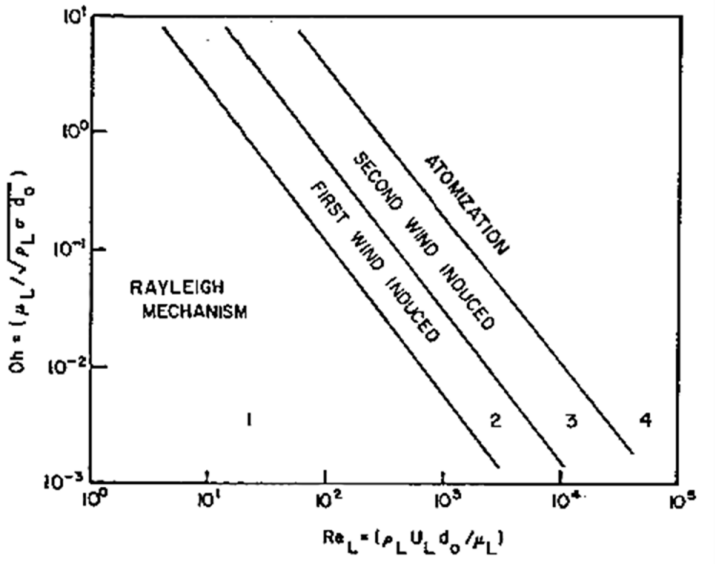

(a) Reitz diagram of break-up regimes, modified from Lefebvre [90].

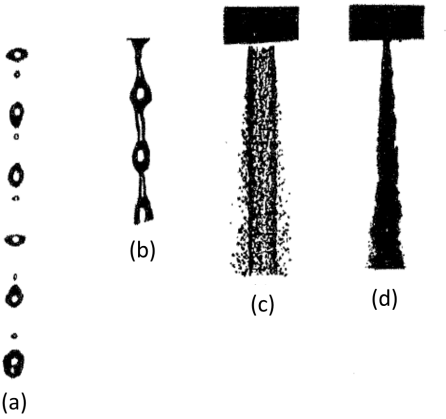

(b) Visualization of liquid jet break-up, from Kuo and Acharya [82].

Figure 2.1: Single liquid jet break-up.

The Ohnesorge number

$$\mathrm{Oh} = \frac{\mu_\mathrm{L}}{\sqrt{\rho_\mathrm{L}\sigma D_0}} \tag{2.8}$$

relates viscous and surface tension (σ) forces. An additional, dependent, parameter is the Weber number

$$\mathrm{We}_\mathrm{L} = \frac{\rho_\mathrm{L} u_\mathrm{L}^2 D_0}{\sigma}. \tag{2.9}$$

It represents the ratio between inertial and surface tension forces and is thus another important parameter in jet break-up. The relation between the three parameters is

$$\mathrm{Oh} = \frac{\sqrt{\mathrm{We}_\mathrm{L}}}{\mathrm{Re}_\mathrm{L}}. \tag{2.10}$$

Coaxial Injection

A more complex configuration is the liquid jet surrounded coaxially by a stream of gas. It is also representative of injection in cryogenic propellant rocket engines. The jet break-up encountered in these injectors is shown in Fig. 2.2.

It is classified in three main categories (Kuo and Acharya [82]): (a) and (b) *Rayleigh* type (steady and pulsating), again with droplets larger than the liquid stream, (c) *membrane* type break-up which forms sheets, and (d) *fiber* type break-up where ligaments peel off the jet. These regimes can be arranged in a Chigier diagram, Fig. 2.2(a).

Two determining parameters have been identified, the liquid Reynolds number, as in Eq. (2.7), and the aerodynamic Weber number

$$\mathrm{We} = \frac{\rho_\mathrm{G} D_0 \left|u_\mathrm{G} - u_\mathrm{L}\right|^2}{2\sigma}. \tag{2.11}$$

The latter is a variation of the liquid Weber number Eq. (2.9), in which the relative motion between gas (subscript G) and liquid is used for the characteristic velocity.

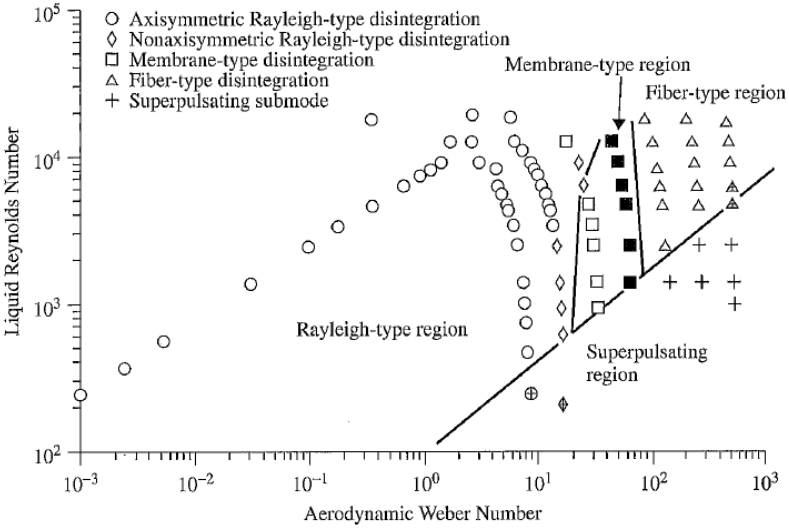

(a) Chigier diagram of coaxial break-up regimes.

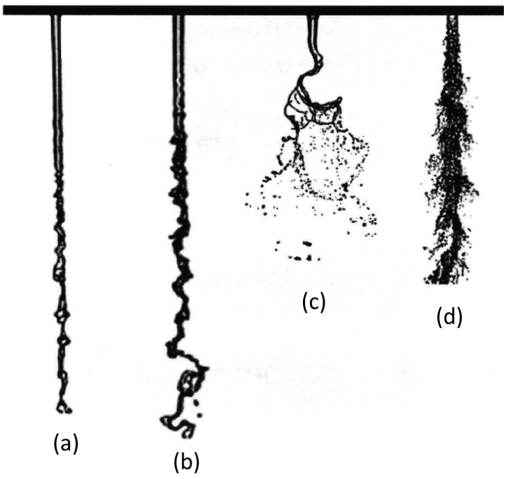

(b) Visualization of coaxial break-up.

Figure 2.2: Break-up of liquid jet coaxially surrounded by gaseous stream (Kuo and Acharya [82]).

2.2.2 Jet Core Length

There are several parameters that are commonly regarded when injection is characterized. Among them are the jet spreading angle, fractal dimension, and liquid core length. The latter, also called potential core length or intact core length, is of major interest in this thesis. A literature review shows that it has been researched extensively; an overview of correlations is given in this section.

The underlying mechanism of all equations discussed in this section is a mechanical interaction that starts where the inner stream first comes into contact with a surrounding stream, be it moving or stagnant. The region of influence then propagates downstream, spreading towards the center of the jet which has hitherto remained unperturbed (hence *potential* core). Subscripts G for gaseous and L for liquid will be used for the surrounding and the central flow, respectively. This is done to interpret the correlations with respect to liquid injection applications where it does not contradict the underlying theory.

Injection including surface tension

Several formulae are given in the literature which account for surface tension. Essentially, the droplets that are stripped from the jet surface constitute a mass flow. Different approaches for the estimation of this value are followed in the literature. Assuming a conical shape starting at the injector, the length of the cone can be estimated. The liquid core is understood as the bulk of connected liquid protruding from the injector, before it is severed by primary atomization, see Fig. 2.3. In the following correlations, factors C mean a generic constant parameter, its actual value might differ from equation to equation.

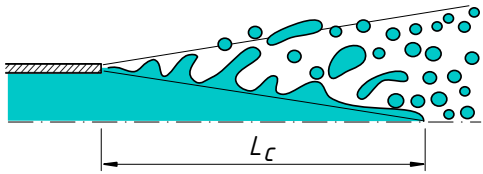

Figure 2.3: Schematic of subcritical injection. Stripping of ligaments from jet. Liquid core length L_{C}.

It is convenient to define an expression for the momentum flux ratio J between a central liquid and a surrounding gaseous stream

$$J = \frac{\rho_G u_G^2}{\rho_L u_L^2}. \tag{2.12}$$

For the case of mass flow through a conical surface being determined by Mayer's capillary wave theory [101], Lasheras and Hopfinger [87] estimated

$$\frac{L_C}{D} = \frac{1}{2CJ^{2/3}} \left(\frac{\sigma}{\mu_L u_L} \right)^{1/3}. \tag{2.13}$$

Reitz and Bracco [137] instead used Taylor's [156] result on the mass flow stripped from a liquid surface,

$$\frac{L_C}{D} = C \left(\frac{\rho_L}{\rho_G} \right)^{1/2} \cdot f\left(\frac{\rho_L}{\rho_G} \left(\frac{\mathrm{Re}_L}{\mathrm{We}_G} \right)^2 \right) \tag{2.14}$$

where alternative Weber and Reynolds numbers are used:

$$\mathrm{We}_G = \frac{\rho_G u_G^2 D_0}{\sigma} \tag{2.15}$$

$$\mathrm{Re}_L = \frac{\rho_L u_L^2 D_0}{\mu_L} \tag{2.16}$$

The function $f()$ approaches zero in the limit of vanishing surface tension, i.e. $\mathrm{We}_G \to \infty$. Eroglu et al. [44] and Lin and Reitz [93] suggested an equation of the form

$$\frac{L_C}{D} = C \frac{\mathrm{Re}_L^b}{\mathrm{We}_G^a}, \qquad 0.3 < a < 0.7, \quad b = 0.5. \tag{2.17}$$

For $a = b = 0.5$ this can be written

$$\frac{L_C}{D} = C \left(\frac{u_L \rho_L}{u_G \rho_G} \frac{\sigma}{\mu_L} \right)^{1/2}. \tag{2.18}$$

A dynamic pressure balance to account for the correct formation of ligament during break-up lead Lasheras [87] to

$$\frac{L_C}{D} = \frac{6}{J^{1/2}} \left(1 - \frac{C\sigma}{\mu_G u_G} \right)^{-1/2}, \quad C = 10^{-3}. \tag{2.19}$$

Injection without surface tension

While this seems like a special case of the previous section, Lasheras and Hopfinger [87] pointed out that both Eq. (2.13) and Eq. (2.18) do not hold in the vanishing surface tension limit where the predicted liquid core disappears altogether - which is inconsistent with the underlying view of mass stripped from the core. The same is true for Reitz' and Bracco's Eq. (2.14). Lasheras specifically took this limit into account. For $\sigma \to 0$, Eq. (2.19) reduces to

$$\frac{L_C}{D} = \frac{6}{J^{1/2}}. \tag{2.20}$$

In fact, most correlations specifically derived without surface tension are based on an estimation of the entrainment velocity into the jet. There is a strong overlap to free jet theory (Abramovich [5]). Figure 2.4 illustrates the concept. The core length is the point where the expanding shear layer interacts with the centerline, thus effectively breaking up the jet.

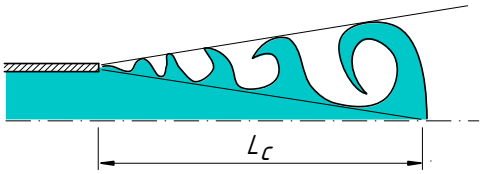

Figure 2.4: Schematic of mixing jet. Atomization by entrainment of surrounding flow. Liquid core length L_C.

Abramovich [5] derived for the case of an incompressible jet with coflow

$$\frac{L_C}{D} = \left| \frac{1 + u_G/u_L}{c(1 - u_G/u_L)\sqrt{0.214 + 0.144\, u_G/u_L}} \right|, \qquad c = 0.27. \tag{2.21}$$

From experiments of water-water coaxial jets, Rehab et al. [136] found the correlation

$$\frac{L_C}{D} = \frac{8}{u_G/u_L}. \tag{2.22}$$

He then went on to derive an equation based on the entrainment velocity for an incompressible jet

$$\frac{L_C}{D} = \frac{1}{2}\left(\frac{1}{C^2 \alpha^2 (u_G/u_L - 1)^2} - 1 \right)^{1/2}, \qquad \alpha = 0.17. \tag{2.23}$$

For large velocity ratio jets, i.e. $u_G \gg u_L$, he calculated

$$\frac{L_C}{D} = \frac{6}{u_G/u_L} \tag{2.24}$$

which is supported by his experimentally found Eq. (2.22). Lasheras and Hopfinger [87] suggested

$$\frac{L_C}{D} = \frac{6}{J^{1/2}} \left(\left| 1 - \frac{u_L}{u_G} \right| \right)^{-1}. \tag{2.25}$$

Villermaux [163] found that the entrained mass flow scales with $u_G(\rho_G/\rho_L)^{1/2}$ and derived

$$\frac{L_C}{D} = \frac{C}{J^{1/2}}, \qquad 6 < C < 8. \tag{2.26}$$

Villermaux explicitly stated this equation to hold for both water-water coaxial jets and for two phase conditions. Particularly, he suggested that surface tension and viscosity dependencies are often introduced merely for dimensional, not for physical reasons.

Injection without surface tension into stagnant environments

As before, the case for $u_G = 0$ represents a special case of the previous section. There are some correlations which still hold in this limit. For injection into stagnant environments, Villermaux suggests that Eq. (2.26) reduces to

$$\frac{L_C}{D} = C \left(\frac{\rho_L}{\rho_G} \right)^{1/2}. \tag{2.27}$$

Lasheras' Eq. (2.25) becomes

$$\frac{L_C}{D} = 6 \left(\frac{\rho_L}{\rho_G} \right)^{1/2}. \tag{2.28}$$

Also Abramovich's equation can be evaluated for $u_G = 0$ to

$$\frac{L_C}{D} \approx 4. \tag{2.29}$$

Equation (2.23) by Rehab simplifies to

$$\frac{L_C}{D} = \frac{1}{2} \left(\frac{1}{C^2 \alpha^2} - 1 \right)^{1/2} \tag{2.30}$$

which is constant, depending on the parameters α and C only. Based on an experimental determination of liquid core lengths measuring electric resistance in the spray, Chehroudi et al. [33] found their data to collapse to

$$\frac{L_C}{D} = C\left(\frac{\rho_L}{\rho_G}\right)^{1/2}, \qquad 7 < C < 16. \tag{2.31}$$

Summary

Given the number of different suggested equations, it is interesting that the authors arrive at few main parameters. For coaxial injection:

- $L_C/D = f(J^{-1/2})$: Lasheras and Hopfinger [87] and Villermaux [163]
- $L_C/D = f(u_L/u_G)$: Rehab et al. [136] and Abramovich [5][3]

For injection into stagnant environments:

- L_C/D = const: Rehab et al. [136] and Abramovich [5][3]
- $L_C/D = f(\rho_L/\rho_G)$: Chehroudi et al. [33] Villermaux [163]

[3] Rehab and Abramovich were mainly concerned with jets with a homogeneous density which might explain why the equations are not differentiated further.

2.3 Thermodynamic Classification of Injection

Can jet break-up in liquid propellant rocket engines be characterized in the same way as discussed in the previous section? Consider the two shadowgraphs in Fig. 2.5, taken by Mayer et al. [105]. In both cases, a coaxial injector is operated at rocket-chamber-like conditions with inert model fluids, i.e. oxygen is replaced by nitrogen, hydrogen by helium. Comparing Fig. 2.5(a) to Fig. 2.2(b) makes clear that the injection can be regarded as (d) fiber type break-up. This is consistent with the literature (Kuo and Acharya [82], Koschel [80]). However, we see that Fig. 2.5(b) does not bear such a resemblance with any of the jets of Fig. 2.2(b). No distinct surface is visible, the interface is fuzzy. Apparently, the surface tension which held together

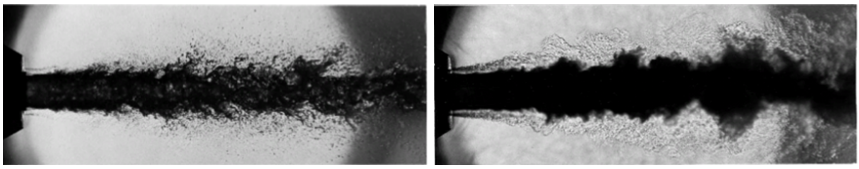

(a) Subcritical pressure, $p_\infty/p_{\mathrm{cr,N2}} = 0.3$. (b) Supercritical pressure, $p_\infty/p_{\mathrm{cr,N2}} = 1.8$.

Figure 2.5: Shadowgraphs of cryogenic nitrogen surrounded by gaseous helium stream, from Mayer et al. [105].

the small structures in Fig. 2.5(a) is no longer acting in Fig. 2.5(b). The reason for the difference between the two cases is the chamber pressure: with regards to the central nitrogen jet critical pressure, Fig. 2.5(a) shows injection into a chamber at subcritical pressure, Fig. 2.5(b) shows injection into a chamber at supercritical pressure[4]. The classification introduced in Ch. 2.2.1 is hence insufficient for our cases, as it does not take into account the thermodynamic state of the injection process.

First, nomenclature needs to be established. Almost 150 years after Andrews introduced the term *'critical point'* [7], there is still no common terminology concerning states and processes in its vicinity. For Bellan [18], a fluid is supercritical when the critical pressure *or* the critical temperature are exceeded. This corresponds to regions (e), (d), and (c) in Fig. 2.6(a). Her argument is that neither phase change nor coexistence is possible in any of

[4] As two species are present, the mixture critical pressure may be elevated compared to the pure fluid values. Still, vanishing surface tension, as shown in Fig. 2.5(b), is an indication for an effective supercritical pressure.

these regions. Younglove [176] and Yang [173] distinguish between a gas in (b), a liquid in (a) and (e) and consider everything exceeding the critical temperature a fluid, i.e. (d) and (c). In this thesis, the more widely used convention (e.g. Weigand et al. [167], Oschwald et al. [125], Oefelein [116]) is adopted after which a fluid is supercritical at *both* supercritical pressure *and* supercritical temperature. This corresponds to region (d) in Fig. 2.6(a). The *fluid at subcritical temperature and supercritical pressure* which is often encountered in cryogenic high pressure injection will henceforth be referred to as *transcritical*[5] *fluid*, following Oschwald et al. [125], Candel et al. [31], Oefelein [117]. This corresponds to region (e) in Fig. 2.6(a). Region (f) comprises states which show strong real gas effects due to proximity to the critical point. While Stotz et al. [154] call this transcritical, it will be called near-critical in this thesis to avoid ambiguity with the former definition of region (e). Generally, (a) is a liquid, (b) and (c) are gaseous phases.

Unfortunately, there is no commonly accepted view on a thermodynamic classification of injection processes either. Figure 2.6(b) will help to establish working definitions for use in this thesis. All break-up phenomena discussed in Ch. 2.2.1 correspond to the injection of a liquid into a gaseous environment and hence correspond to process type A. This will be called *subcritical* injection in accordance with Lamanna et al. [85]. They extend this regime to supercritical pressures as well: Lamanna argues that by injecting a fluid into a different environment, the local mixture may have a critical pressure exceeding the pure fluid critical pressure, effectively changing the process to type A. She adds this might be easily mistaken in shadowgraphs because of their inherent *'misleading nature'*, and/or droplets might be just too small to be discernible. Simplifying the picture by just regarding single fluid injection, process B can be regarded as a process different from A. This view is taken e.g. by Oschwald et al. [125] or Stotz et al. [154] and will be shared here. Following these latter authors, the term *transcritical* injection will be used. The transcritical process is called a state transition by Kuo [81] despite the supercritical pressure. Both Stotz et al. [154] and Lamanna et al. [85] complete the picture by suggesting two additional classifications. First they identify a *supercritical regime* where a supercritical fluid is injected into a fluid at supercritical temperature and either sub- (E) or supercritical (D) pressure. Second, they identify the *near critical flashing* regime C with barely subcritical temperatures where the fluid at supercritical pressure is injected into an environment at subcritical pressure. The remaining regimes mainly consist of cases where environment and injectant are very similar in density and no phase coexistence can occur, e.g. gas-gas, liquid-

[5] from Latin trans-, meaning *across*, *beyond* or *on the opposite side*

liquid, transcritical-liquid injection. As injectant and environment are thus very similar in their thermodynamic nature, a classification with regards to the thermodynamic states does not appear beneficial and is not pursued.

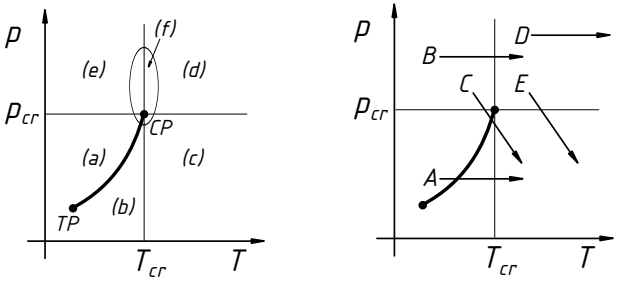

(a) Fluid states.

(b) Injection processes in p-T diagram.

Figure 2.6: States and processes in generic $p-T$ diagram, coexistence line between triple point (TP) and critical point (CP).

Figure 2.6 shows that the relation of the state to the critical point is essential. It is thus beneficial to express the state in terms of the critical values. State variables that are thus made dimensionless by the respective fluid critical variable are called reduced values, denoted by a subscript r:

$$p_\mathrm{r} = \frac{p}{p_\mathrm{cr}}, \tag{2.32}$$

$$T_\mathrm{r} = \frac{T}{T_\mathrm{cr}}, \tag{2.33}$$

$$\rho_\mathrm{r} = \frac{\rho}{\rho_\mathrm{cr}}, \tag{2.34}$$

$$v_\mathrm{r} = \frac{v}{v_\mathrm{cr}}. \tag{2.35}$$

Whether this classification is physically reasonable can be evaluated best when comparing exemplary injection visualizations. Figure 2.7 compiles shadowgraphs for each of the processes A to E from Fig. 2.6(b), conditions are shown in Tab. 2.1.

It appears that from the five cases visualized in Fig. 2.7, three groups can be distinguished: Case (A) is the classical liquid jet with a distinct surface. Cases (B) and (D) are similar but, lacking surface tension, exhibit a more convoluted and fuzzy interface. Cases (C) and (E) are remarkably different

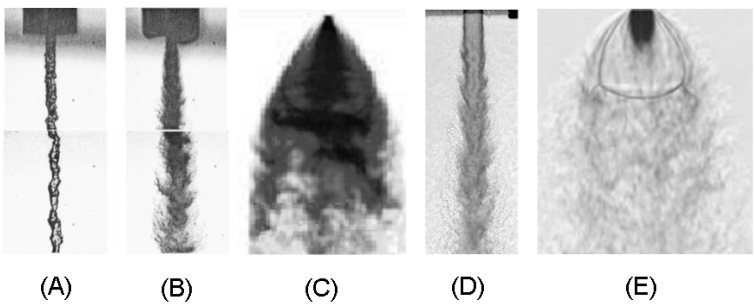

Figure 2.7: Visualizations of injection regimes from Fig. 2.6(b). Conditions in Tab. 2.1. A and B modified from Chehroudi et al. [34], C modified from Lamanna et al. [85], D from Branam and Mayer [23], E modified from Stotz et al. [154].

Type	$T_{r,in}$	$p_{r,in}$	$T_{r,\infty}$	$p_{r,\infty}$	Jet	Chamber
A	0.71-0.87	≈0.23	2.38	0.23	N_2	N_2
B	0.71-0.87	≈1.23	2.38	1.23	N_2	N_2
C	0.95	6.59	1.9	0.02	C_6H_{14}	Ar
D	1.05	≈1.77	2.36	1.77	N_2	N_2
E	1.09	6.59	1.9	0.16	C_6H_{14}	Ar

Table 2.1: Conditions of visualizations in Fig. 2.7. Reduced values with respect to injected pure fluid.[6]

from the previous cases, showing a high pressure jet expanding in a lower pressure environment. Similar results have been found for ideal gas expansion into vacuum: Ashkenas and Sherman [8] were able to theoretically analyze what Muntz [113] saw in his electron beam experiments, shown in Fig. 2.8.

[6] Cases A, B, and D are pure fluid cases, i.e. the pure fluid critical pressure is the effective critical pressure. While C and E technically comprise a mixture, the jet expands at supersonic velocity into the low pressure environment, mixing does not take place in the near-injector region. Figure 2.8 shows the same topology for an ideal gas case. It appears, this is not a real gas phenomenon but instead caused by the large pressure ratio.

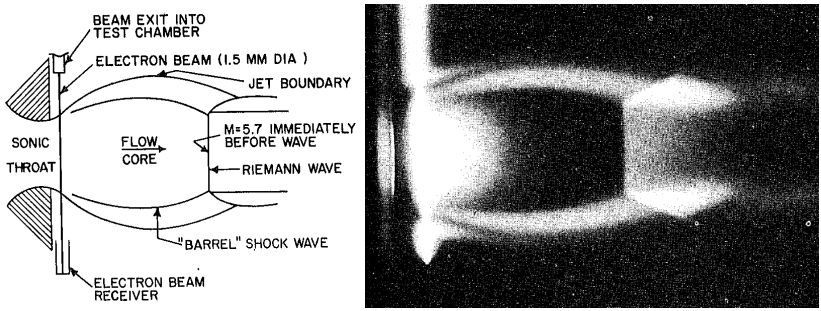

(a) Schematic of flow phenomeona.

(b) Electron beam visualization.

Figure 2.8: Helium expansion into near vacuum, reservoir to test section pressure ratio is 15.9, from Muntz [113].

2.3.1 Injection in Rocket Engines

Typically, in a cryogenic liquid propellant rocket engine, a central stream of oxygen is injected with 5 to 10 m/s. At temperatures below 100 K, its liquid-like density exceeds 1000 kg/m^3. The oxygen is surrounded by a hydrogen stream at 200 to 300 m/s. Used as a coolant for the combustion chamber before injection, the hydrogen is preheated to a gaseous state. Both fluids interact upon injection into the combustion chamber, forming a shear layer due to the difference in velocity. Surface instabilities grow, leading the oxygen stream to break up in face of the surrounding gas. It can be shown (Villermaux [163]) that in this shear layer instabilities of the interface between both streams tend to grow. Larger velocity differences tend to increase the growth rate and frequency, whereas higher density differences, viscosity, and surface tension tend to dampen growth rate and frequency of the instabilities. Figures 1.5 and 2.5 show that chamber pressure in relation to the oxygen critical pressure has profound impact on the jet break-up character. Hence. the difference between injection at sub- and at supercritical pressures will be discussed in the following.

2.3.2 Subcritical Pressures

Rocket injection at subcritical pressures has been called essentially understood (Mayer and Tamura [107]). In subcritical injection, the pressure of the combustion chamber is below the critical pressure of oxygen. Latent heat

of vaporization and surface tension are finite. In the cold flow case, growing instabilities in the shear layer will form as waves with ever increasing amplitude on the interface between the streams until they disconnect from the main stream, featuring well defined sharp boundaries (Habiballah et al. [54]). This is dubbed primary atomization. The stripping of mass will slowly work its way towards the centerline of the central jet, until the stream is no longer connected. The length of the compact oxygen stream is called liquid core length, see Fig. 2.3. The severed droplets will continue to move in the gaseous stream. If the aerodynamic forces due to velocity differences between disperse and carrier phase are large enough, the droplets will break up further, undergoing secondary atomization. Finally, the oxygen droplets vaporize, mix with the surrounding hydrogen stream, and react. The rate determining process is the jet break-up and atomization (Candel et al. [31]). In reactive cases, Mayer and Tamura [107] found that all stripped oxygen is consumed immediately, essentially no droplets are observed in the chamber.

2.3.3 Supercritical Pressures

Unlike subcritical injection, injection at supercritical pressures is presently considered not well understood (Oefelein [116], Gautam and Gupta [47]). Bellan [18] asked in 2000: *"Does a supercritical spray exist, and if so, what is it?"* Nevertheless, high pressure liquid propellant rocket engines remain technically highly relevant and are operated successfully.

The topic has received much interest in the last 15 years; experimental results have completely altered the view on the physical phenomena, as discussed in Ch. 1.2. In a 2006 special issue of Combustion Science and Technology, dedicated to transcritical injection, German, American, and French groups summarize the state of knowledge (Oschwald et al. [125], Candel et al. [31], Zong and Yang [179], Oefelein [117], Bellan [19], Habiballah et al. [54]). Researchers by and large agree on the observed phenomena. Figure 2.9 shows the near injector region of a representative single injector experiment by Mayer and Tamura [107]. In shadowgraphs, no droplets or ligaments are visible (Mayer and Tamura [107], Habiballah et al. [54], Oschwald et al. [125]). Compared to low pressure injection, the interface looks diffuse (Habiballah et al. [54]), stringy features separate from the core, the interface dissolves (Oschwald et al. [125]). In fact, the process is described to resemble turbulent mixing rather than liquid jet break up (Newman and Brzustowski [114], Habiballah et al. [54], Candel et al. [31], Oschwald et

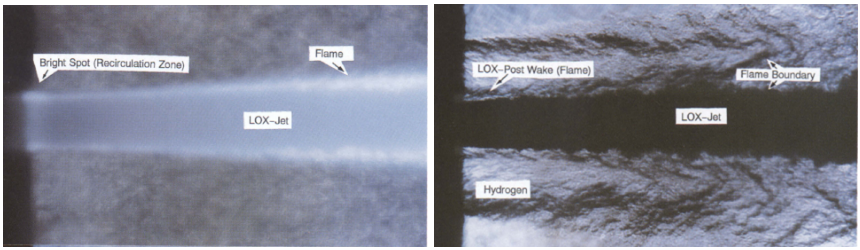

(a) Chemiluminescence. (b) Shadowgraph.

Figure 2.9: High pressure H_2/O_2 flame near coaxial injector, from Mayer and Tamura [107].

al. [125], Bellan [18]). The time scales of the mixing process also form the rate determining step of flame spreading, the momentum flux ratio of aerodynamic break up loses its significance (Candel et al. [31]). Comparison with numerical computations suggests that observed length scales are related to the turbulent Taylor scale (Oschwald et al. [125]). For common LOX post thicknesses, the flame is anchored in a small recirculation zone behind it, Fig. 2.9(a). This has been observed experimentally by Mayer and Tamura [107], Ivancic [67], Candel et al. [30, 31] and numerically (Oefelein and Yang [119]). In typical hydrogen rich injection, the flame encloses the oxygen stream. Experimentalists (Mayer et al. [107, 106], Candel et al. [31]) and numericists (Yang [173], Oefelein and Yang [119, 116]) report that the flame essentially isolates oxygen from hydrogen. Hydrogen and oxygen react in the hot mixing layer (Oefelein [117]).

Quantitative data remain scarce. OH* emission images (Candel et al. [31], Juniper et al. [73], Ivancic [67], Smith et al. [148]) suggest the main chemical reaction zone in the shear layer close to the LOX core. Local temperature measurements using CARS have been carried out at high pressures but not much data is available (Klimenko et al. [78], Grisch et al. [53]). Results are inconclusive: Measured temperatures do not exceed 2000 K, staying well below the expected stoichiometric adiabatic flame temperature of ≈ 3600 K. Also, CFD results typically predict higher temperatures exceeding 3000 K. Yang [173] and Oefelein [116] find that combustion occurs at near stoichiometric conditions. Masquelet et al. [99] and Oefelein [116] calculate local temperatures exceeding 4000 K in their LES of injection shear layers. The reasons for the discrepancy remain unclear. Habiballah et al. [54] suggest that a different combustion mode at high pressures might exist.

2.3.4 Mixture Critical Pressure

There is still debate about whether the oxygen break up occurs supercritically or subcritically. While the pure oxygen critical pressure is exceeded, this might not be true of the local mixture critical pressure when oxygen comes into contact with other species. This effect has been demonstrated in experiments as shown in Fig 2.10: Woodward and Talley [170] observed the transition to surface tension dominated break up at twice the critical pressure of the injected nitrogen when the environment was enriched more and more with helium.

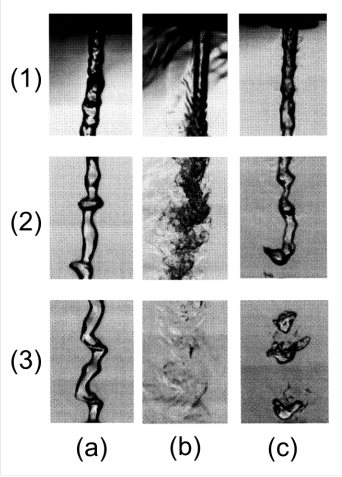

Figure 2.10: Shadowgraph images of transcritical nitrogen injection, injector diameter 0.25 mm. (a) and (b) into pure nitrogen at $p_{\mathrm{r}} = 0.83$ and $p_{\mathrm{r}} = 2.03$; (c) into mixture of nitrogen and helium at $p_{\mathrm{r,N2}} = 2.03$. Taken at axial locations downstream of injector exit (1) 0.0 to 1.9 mm; (2) 7.4 to 9.5 mm; (3) 15.0 to 17.1 mm. Modified from Woodward and Talley [170].

The reason is that a mixture critical point differs from the component critical points (Pfennig [128]): In a binary mixture, the critical temperature will lie between the individual critical temperatures while the mixture critical pressure can exceed the pure fluids critical pressure significantly.[7] Figure 2.11 demonstrates this. Yang et al. [175] performed calculations of phase equilibria in a hydrogen-oxygen binary system. Figure 2.11(a) is a boiling point diagram, evaluated for various reduced pressures (with respect to oxygen)

[7] The actual mixing rules which show this are presented in Ch. 3.1.4.

between 0.1 and 5. At the oxygen critical pressure, $p_r = 1$, the mixture critical point corresponds to pure oxygen. However, at supercritical pressures, the pure fluids do not exist in a multiphase form anymore, the mixture region curve detaches from the pure oxygen ordinate. At $p_r = 1.6$, the mixture critical point, beyond which vapor and liquid may no longer coexist, corresponds to a temperature of 145 K at an oxygen mole fraction of 0.8. For even higher pressures, such as $p_r = 5$, the critical temperature and oxygen mole fraction are further reduced. The set of mixture critical points is shown in Fig. 2.11(b) in a $p - T$ diagram as an extension of the oxygen boiling line.

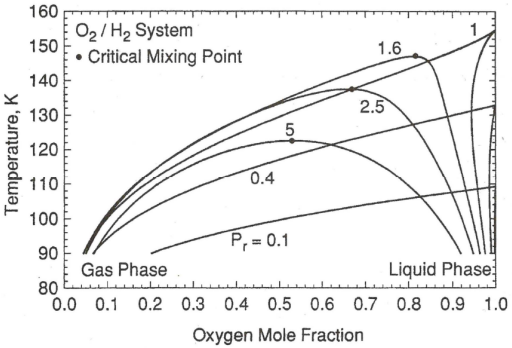

(a) Boiling point diagram for various pressures.

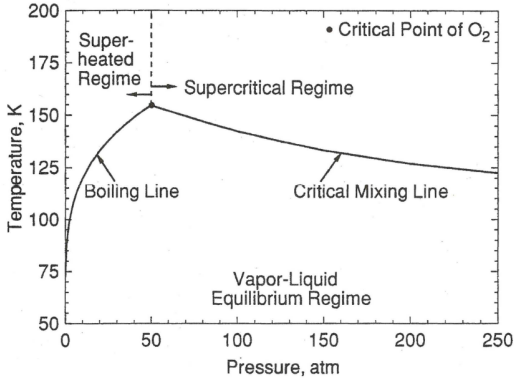

(b) Pressure-temperature diagram with critical mixing line.

Figure 2.11: Phase equilibrium of H_2/O_2 mixture, from Yang et al. [175].

2.3.5 Multiphase Mixtures in Rocket Engines?

It is in fact very common to analyze the effect of oxygen-hydrogen mixing on surface tension and critical point when analyzing flow in rocket engines (Mayer et al. [104], Kuo [81], Yang et al. [174], Oschwald et al. [125], Poschner and Pfitzner [131], Jarzcyk [70]). In addition to calculating vapor-liquid equilibria, as shown in Fig. 2.11, Dahms and Oefelein [40] suggested to use a Knudsen number based evaluation to determine the existence of residual surface tension under these conditions. They found that the calculated mixture critical pressure of some cryogenic oxygen-hydrogen compositions does indeed exceed the pressure found in combustion chambers, turning the injection process subcritical again. Jarzcyk [70] extended the equilibrium investigations by analyzing the timescales of homogeneous nucleation in a cryogenic oxygen-hydrogen mixture. She found that condensation was likely to occur.

Figures 2.9(b) and 2.5(b) do not show any droplets, but, as Lamanna et al. [85] and Habiballah et al. [54] suggested, droplets might just be too small to be detected at the used CCD resolution[8]. However, the jet structure in Fig. 2.5(b) appears different from Fig. 2.5(a), and different from the first wind induced type break-up shown in Fig 2.10(c). Furthermore, significant differences in flame spreading, flame stability, fractal dimensions of the jet structure, characteristic break up times, significance of aerodynamic forces compared to heat transfer, *have* been found when exceeding the oxygen critical pressure (Candel et al. [31], Oschwald et al. [125], Mayer et al. [174]). For the very high pressure of 20 MPa, Harstad and Bellan [61] found that only a single phase is present throughout droplet lifetime in numerical simulations of transcritical oxygen drop vaporization at 100 K in a hot hydrogen environment at 1000 K .

The picture changes again when taking into account chemical reactions. A cryogenic jet of oxygen is isolated by an enclosing flame from the surrounding gaseous hydrogen (Mayer and Tamura [107]). Oefelein [116] reports real gas behavior in the cold core, ideal gas characteristics in reaction and product zones. Cheng and Farmer [36, 35] use ideal mixing rules for their computation of reactive single injector flows and find very good agreement to experimental data. Jarczyk [70] compares ideal and real thermodynamic mixing models and finds almost no influence on flame shape.

Are these numerical artifacts or is it physics? To quantify the extent to which real gas behavior, such as vapor-liquid equilibria, play a role, it is convenient

[8] 20 μm as stated by Habiballah et al. [54]

to define the compressibility (or real gas) factor Z

$$Z = \frac{p}{\rho R T}. \tag{2.36}$$

For ideal gases, $Z \equiv 1$, for real gases $Z < 1$. Now, consider Fig. 2.12 from Oefelein [117]. Plotted are radial profiles extracted from LES results of reactive coaxial injection at 0.03 LOX jet diameters downstream of the injector. The central LOX jet enters the chamber with a temperature of $T = 100$ K, the surrounding gaseous hydrogen stream with $T = 150$ K. The chamber pressure is 10.1 MPa.

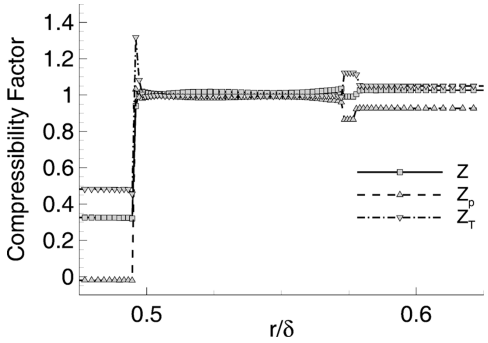

(a) Compressibility factor.

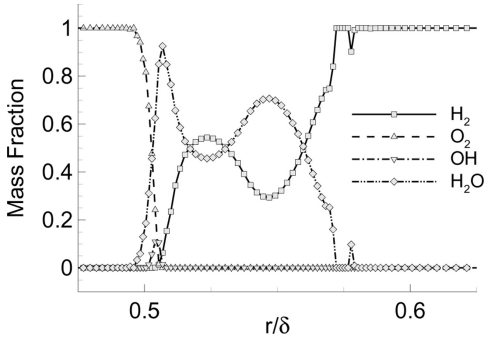

(b) Mass fraction.

Figure 2.12: Instantaneous radial profiles extracted from LES results of reactive coaxial injection. δ is the LOX jet diameter, axial position is 0.03δ downstream of injector. Central LOX jet $T = 100$ K, gaseous hydrogen jet $T = 150$ K, $p = 10.1$ MPa. From Oefelein [117].

Figure 2.12(a) pinpoints the position of real-gas to ideal-gas transition at approximately 0.4975 diameters. At this position essentially pure oxygen is present in the flow; other species appear in the mixture only where Z has already reached unity, i.e. in the form of ideal gases.

A second set of results of cryogenic nonpremixed flames has been computed by Lacaze and Oefelein [83]. They investigated elementary counterflow diffusion flames at various pressures and injection temperatures. A result for a pressure of 7 MPa, corresponding to a reduced pressure for oxygen of 1.4, is shown in Fig. 2.13. Plotted is the compressibility factor against the mixture fraction Z_H, a normalized mass fraction of fuel, reaching 1 in pure fuel and 0 in pure oxidizer. It can be seen that the compressibility factor reaches unity at a mixture fraction of 0.004. I.e., significant mixing occurs only when the involved fluids have converted to ideal gases.

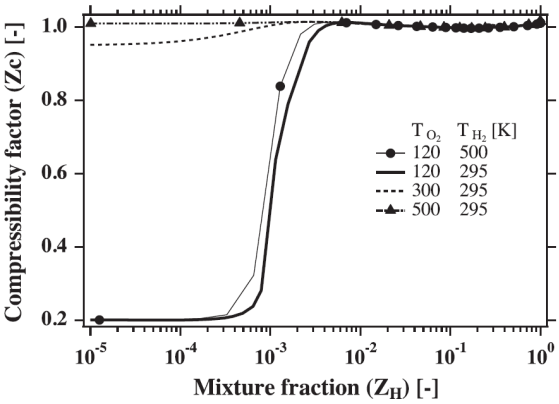

Figure 2.13: Stagnation line profiles of compressibility factor in a counterflow diffusion flame, $p = 7$ MPa. In mixture fraction space; the mixture fraction Z_H is a normalized mass fraction of fuel, reaching 1 in pure fuel and 0 in pure oxidizer. From Lacaze and Oefelein [83].

While the evidence is numerical, it points towards a physical phenomenon: Mixing in cryogenic high pressure nonpremixed flames, as encountered in rocket engines, takes place as an ideal gas phenomenon.

2.4 Summary

Theoretical approaches can be compared to actual jet break-up phenomenology as encountered in rocket engine representative experiments. The phenomenological reasoning of liquid mass shedding seems best suited to subcritical injection, as shown in Fig. 2.5(a). Entrainment on the other hand matches transcritical injection, see Fig. 2.5(b).

Injection at subcritical and at supercritical pressures differ substantially. Bellan [18] goes so far to suggest a different naming: subcritical evaporation and atomization correspond to supercritical emission and disintegration, respectively.

Experiments of injection into stagnant environments are highly relevant for fundamental studies of rocket injection. For representative cases, a second wind induced break-up mode is witnessed (Oschwald et al. [125]). In actual cryogenic rocket engine coaxial injection, fiber type break-up is expected (Kuo and Acharya [82], Koschel [80]). Both mechanisms resemble each other strongly.

Main stage rocket combustion chambers operate at pressures exceeding the critical pressure of oxygen, the surface tension of pure oxygen is naught. Several authors discuss the possible existence of surface tension or discrete droplets in presence of another species, mostly hydrogen (e.g. Dahms and Oefelein [40], Oefelein and Aggarwal [118], Yang [173]). The rationale is that while exceeding the oxygen critical pressure, the critical pressure of the oxygen-hydrogen *mixture* is not reached. In any way, it is safe to assume that injection takes place in a high Weber number limit in main stage engines. Thus, the correlations assuming vanishing surface tension appear appropriate for these kinds of flows.

For cryogenic coaxial reactive injection, a literature study suggests that mixing occurs as an ideal gas phenomenon.

3 Modeling and Behavior of Real Fluids

3.1 Thermodynamic Description of Fluids

The question arises of how fluid behavior can be described quantitatively. In order to appropriately cover the thermodynamics of a fluid, a model

$$F(p, \rho, T) = 0 \tag{3.1}$$

is needed which relates pressure p, density ρ (the inverse specific volume v), and temperature T. Typically, models are sought that simplify a numerical solution.

3.1.1 Simple Models

For incompressible flow, such as flow of liquids or gaseous flow at a low Mach number, density can be assumed constant,

$$\rho = \text{const.} \tag{3.2}$$

This greatly simplifies the numerical solution of a flow problem, as now the energy equation is decoupled from the momentum and species transport equations and can be solved independently (Anderson [6]). The pressure is then computed from a Poisson equation to ensure conservation of mass, or, mathematically speaking, to ensure the flow field is divergence free. If density cannot be assumed constant anymore, e.g. in a compressible flow with shocks or expansion through a nozzle, often the assumption of an ideal gas is sufficient. In this case, where molecules are understood to be point-masses which do not interact with each other, the ideal gas equation

$$p = \rho R T \tag{3.3}$$

holds. Here, R is the specific gas constant formed as the ratio of the universal gas constant and the molecular weight of the gas in question $R = \mathscr{R}/\mathscr{M}$. Allowing for a variable density requires the simultaneous solution of all transport equations, as the temperature, density, and pressure fields are closely

coupled. Given those two models, i.e. constant density for a liquid, and ideal gas, subcritical injection can already be computed using efficient models.

3.1.2 Real Gas Equations of State

Extending the state space of the regarded fluids towards low temperatures and high pressures, intermolecular forces and the size of molecules can no longer be neglected. The real gas factor Z is a dimensionless measure of deviation from ideal gas behavior. It is defined as

$$Z = \frac{p}{\rho R T}. \tag{3.4}$$

For ideal gases, $Z \equiv 1$. There are two main classes of simple equations of state to account for real gas effects: cubic and virial.

Cubic Equations of State

The first equation of state (EOS) capable of predicting real gas behavior is van der Waals' [161] EOS

$$p = \frac{RT}{v-b} - \frac{a}{v^2}. \tag{3.5}$$

Van der Waals extended the ideal gas EOS by two new constants, a and b: The acting pressure is reduced by an attractive potential between the particles proportional to a, the available volume is reduced by the molecular volume b. The parameters are fluids specific and depend on the respective critical parameters. Equations of this type are cubic in terms of the specific volume and are hence called cubic EOS. More elaborate and accurate equations have been developed since, but the van der Waals equation in its simplicity already qualitatively exhibits key characteristics, such as a liquid vapor coexistence region or a critical point.

The first simple yet accurate EOS was developed by Redlich and Kwong [135] (RK). The main improvement over the van der Waals (vdW) equation was to turn the constant parameter a into a temperature dependent function $\alpha(T)$. Additionally, the low volume behavior has been adapted (Pfennig [128]):

$$p = \frac{RT}{v-b} - \frac{\alpha(T)}{v(v+b)} \tag{3.6}$$

with

$$\alpha(T) = \frac{a}{\sqrt{T}}, \tag{3.7}$$

$$b = \frac{2^{1/3}-1}{3}\frac{RT_{\mathrm{cr}}}{p_{\mathrm{cr}}}. \tag{3.8}$$

Its successor, the Soave-Redlich-Kwong [149] EOS (SRK), is still widely used today. It additionally includes Pitzer's acentric factor ω to account for non-spherical molecules. Here, $\alpha(T)$ is now expressed as

$$\alpha(T) = \frac{1}{9(2^{1/3}-1)}\frac{(RT_{\mathrm{cr}})^2}{p_{\mathrm{cr}}}\left[1+m(1-\sqrt{T_{\mathrm{r}}})\right]^2 \tag{3.9}$$

with

$$m = 0.480 + 1.574\omega - 0.176\omega^2 \tag{3.10}$$

and the acentric factor

$$\omega = -\log_{10}\left(\frac{p_{\mathrm{sat}}}{p_{\mathrm{cr}}}\right)_{T_{\mathrm{r}}=0.7} - 1.0. \tag{3.11}$$

The Peng-Robinson (PR) EOS is similar in structure to the SRK equation but has been fitted particularly to match the compressibility factor Z at the critical point better [126]:

$$p = \frac{RT}{v-b} - \frac{\alpha(T)}{v^2+2bv-b^2} \tag{3.12}$$

with

$$\alpha(T) = 0.457236\frac{(RT_{\mathrm{cr}})^2}{p_{\mathrm{cr}}}\left[1+m(1-\sqrt{T_{\mathrm{r}}})\right]^2 \tag{3.13}$$

$$m = 0.3746 + 1.54226\omega - 0.26992\omega^2 \tag{3.14}$$

$$b = 0.077796\frac{RT_{\mathrm{cr}}}{p_{\mathrm{cr}}}. \tag{3.15}$$

Comparing the RK, SRK, and PR equations of state, Pfennig [128] summarizes that while all EOS are acceptably accurate for low densities, only Peng-Robinson and Soave-Redlich-Kwong equations of state can be used for higher densities. PR better matches the density along the critical isotherm up to twice the critical density, RK and SRK are better suited to determine phase equilibria and vapor pressure curves.

Virial Equations of Sate

An alternative approach to develop a real gas equation of state is followed in virial EOS: They constitute a series expansion in terms of density of the compressibility factor Z:

$$\frac{p}{\rho RT} = Z = 1 + B_2\rho + B_3\rho^2 + \ldots \tag{3.16}$$

The coefficients B_i are functions of temperature only[1]. However, these pure virial equations of state do not represent fluids in a sufficient accuracy over a sufficient range of states for engineering purposes (Pfennig [128]).

A remedy was discovered by Benedict, Webb, and Rubin [20] who added an additional exponential and a ρ^5 term to account for sufficient pressure gradients in the liquid phase:

$$\begin{aligned} Z = 1 \quad &+ \quad \left(B_0 - \frac{A_0}{RT} - \frac{C_0}{RT^3}\right)\rho \\ &+ \quad \left(b - \frac{a}{RT}\right)\rho^2 \\ &+ \quad \frac{a\alpha}{RT}\rho^5 \\ &+ \quad \frac{c(1+\gamma\rho^2)}{RT^3}\rho^2 e^{-\gamma\rho^2}. \end{aligned} \tag{3.17}$$

The parameters A_0, B_0, C_0, a, b, c, α, γ are fluid dependent. An extended and further improved version is the Modified-Benedict-Webb-Rubin (MBWR) EOS by Younglove [176],

$$p\left(\rho, T\right) = \sum_{n=1}^{9} \rho^n F_{n-1} + e^{-\delta^2} \sum_{n=10}^{15} \rho^{2n-17} F_{n-1}. \tag{3.18}$$

The functions F_n are listed in Tab. 3.1 to illustrate the complexity of the EOS in comparison with the other equations discussed in this section. Coefficients G_i are fluid dependent parameters.

[1] B_2 is called the second virial coefficient, B_3 is the third, and so on. The first virial coefficient is B_1=1 and has already been replaced in the shown equation.

n	F_n
0	RT
1	$G_1T + G_2T^{0.5} + G_3 + G_4/T + G_5/T^2$
2	$G_6T + G_7 + G_8/T + G_9/T^2$
3	$G_{10}T + G_{11} + G_{12}/T$
4	G_{13}
6	G_{16}/T
7	$G_{17}/T + G_{18}/T^2$
8	G_{19}/T^2
9	$G_{20}/T^2 + G_{21}/T^3$
10	$G_{22}/T^2 + G_{23}/T^4$
11	$G_{24}/T^2 + G_{25}/T^3$
12	$G_{26}/T^2 + G_{27}/T^4$
13	$G_{28}/T^2 + G_{29}/T^3$
14	$G_{30}/T^2 + G_{31}/T^3 + G_{32}/T^4$

Table 3.1: Functions F_n of the Modified Benedict-Webb-Rubin equation of state.

3.1.3 Corresponding States Principle

How general are these EOS? While each set of parameters is specifically suited to a certain species, the overall structure of the fluid state plane is similar between simple substances. One such commonality is the existence of a critical point. Figure 2.6 already suggested the introduction of reduced variables, Eqs. (2.32)-(2.35), effectively expressing fluid properties in terms of the critical values. A case for the relevance of reduced values can also be made by looking at the properties of the critical point in the framework of the simple van der Waals equation of state. At the critical point, as discussed by Andrews [7], differences in properties between the gaseous and the liquid phase vanish. Mathematically, it is characterized by an inflection of the critical isothermal (Weigand et al. [167]),

$$\left(\frac{\partial p}{\partial v}\right)_T = 0 \tag{3.19}$$

and

$$\left(\frac{\partial^2 p}{\partial v^2}\right)_T = 0 \tag{3.20}$$

for $T = T_{cr}$ and $v = v_{cr}$. Applying this to the van der Waals equation Eq. (3.5) leads to parameters a and b which are expressed solely in terms of the critical values:

$$a = \frac{27}{64}\frac{(RT_{cr})^2}{p_{cr}} \tag{3.21}$$

$$b = \frac{1}{8}\frac{RT_{cr}}{p_{cr}}. \tag{3.22}$$

This means it is no longer necessary to fit parameters for each fluid - instead, knowledge of the critical values is sufficient. Expressed differently: It implies that all fluids can be described by a single EOS when states are expressed in dimensionless form, i.e. in terms of the critical values. This concept is called *corresponding states principle* (CSP). The question arises whether this is an effect of the mathematical structure of the vdW EOS or of the underlying fluid behavior that is modeled. Figure 3.1 shows reduced data for argon, nitrogen, methane, and propane in a p_r-v_r diagram. For molecules that can be assumed near spherical, i.e. argon, nitrogen, methane, reduced fluid data collapses very well.

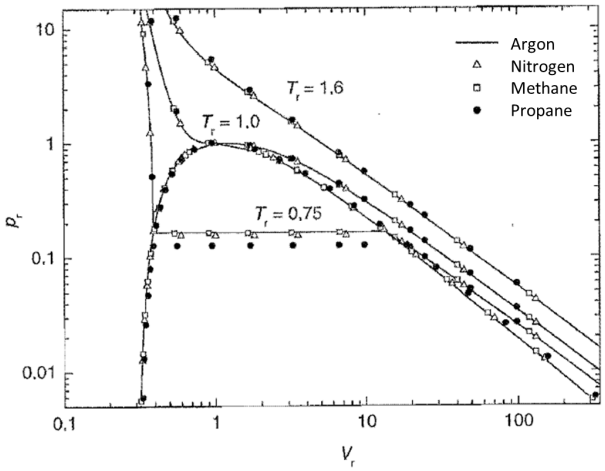

Figure 3.1: Corresponding states principle: $p_r - v_r$ diagram for selected fluids, modified from Pfennig [128].

The extended corresponding states principle (ECS) then accounts for deviations, e.g. due to the nonsphericity of molecules such as hydrocarbons, by

using Pitzer's acentric factor ω (e.g. Harstad et al. [62], Ely and Hanley [42], Yang [173], Oefelein and Yang [119]).

3.1.4 Mixture Rules

So far only pure fluids have been discussed. In a combustion chamber, however, mixtures are encountered. It is impractical to develop specific models of every conceivable mixture composition. Instead, mixture models are required which build on pure fluid data.

Single Fluid Mixing

The underlying assumption behind single- or one-fluid models, is that *"the configurational properties of a single-phase mixture can be equated to those of a hypothetical pure fluid"* (Ely and Hanley [42]). Applying appropriate rules to determine the critical point properties of the mixture, the ECS can be used to evaluate the mixture $p-v-T$ behavior by mapping the properties of a well known reference fluid. The following rules are used by several authors (e.g. Harstad et al. [62], Ely and Hanley [42, 43], Yang [173], Pfennig [128], Poschner and Pfitzner [131]):

$$T_{\mathrm{cr},i,j} = \left(T_{\mathrm{cr},i} \cdot T_{\mathrm{cr},j}\right)^{1/2}, \tag{3.23}$$

$$v_{\mathrm{cr},i,j} = \left(\frac{1}{2}\left(v_{\mathrm{cr},i}^{1/3} + v_{\mathrm{cr},j}^{1/3}\right)\right)^3, \tag{3.24}$$

$$Z_{\mathrm{cr},i,j} = \frac{1}{2}\left(Z_{\mathrm{cr},i} + Z_{\mathrm{cr},j}\right), \tag{3.25}$$

$$p_{\mathrm{cr},i,j} = \frac{Z_{\mathrm{cr},i,j} R T_{\mathrm{cr},i,j}}{v_{\mathrm{cr},i,j}}, \tag{3.26}$$

$$\omega_{i,j} = \frac{1}{2}\left(\omega_i + \omega_j\right). \tag{3.27}$$

If, additionally to the hypothetical pure fluid assumption, one assumes that all involved fluids *"obey two parameter classical corresponding states formalism"*, Ely and Hanley [42] summarize that mixing rules for these parameters can be derived. The set of mixture rules is commonly called van der Waals mixing and provides parameters a and b to be applied to vdW, PR, SRK and

similar equations:

$$a = \sum_{i=1}^{N}\sum_{j=1}^{N} y_i y_j \sqrt{a_i a_j}(1-k_{i,j}) \tag{3.28}$$

$$b = \sum_{i=1}^{N} y_i b_i \tag{3.29}$$

$$\omega = \sum_{i=1}^{N} y_i \omega_i \tag{3.30}$$

The binary interaction parameter $k_{i,j}$ is not known for many pairings and often assumed to be zero (Okong'o and Bellan [121]).

Limits to Single Fluid Mixing Models

Ely and Hanley [42, 43] discussed the conditions of applicability of a thus derived single fluid model:

1. The mixture exists as a single phase.
2. The mixture properties can be expressed via a hypothetical pure fluid.
3. All fluids involved in the mixture are similar, i.e their critical parameters are within a factor of two.
4. The reference fluid should be similar to the involved fluids.
5. If the single fluid model is used to evaluate the mixture viscosity, the involved fluids must not be polar.

Ely and Hanley specifically emphasized the third condition, noting that *"the one-fluid model breaks down"* if this criterion is violated.

Two Fluid Mixing

In a two fluid mixing model, an equation of state is solved for each component (Pfennig [128])[2]. This is fundamentally different from mapping reference fluid properties to a hypothetical pure fluids EOS. Alas, there is no established mixing rule, the approach is apparently hardly used in the literature. Two exceptions were found, Cheng and Farmer [36, 35] and Poschner and

[2] For a multi species mixture this will henceforth be called multi fluid mixing.

Pfitzner [131], who reported to use an additive partial volumes rule without going into more details. Overall results were very good. However, Poschner and Pfitzner are critical of its applicability and commented it might violate the conservation of momentum in a pressure based solver.

The difficulty lies in defining a formulation for fluid interaction - which the ECS based single fluid mixing so elegantly has avoided. A simple mixing rule is to *neglect* all molecular interaction. This is essentially equivalent to the model view of an ideal gas mixture, the multi fluid mixing rule then is known: Dalton's law, stating that the mixture pressure equals the sum of the components partial pressures. Similarly, Raoult's law states that the vapor pressure of an ideal solution equals the sum of the individual component vapor pressures (Baehr and Kabelac [11]).

3.1.5 Real Gas Departure Functions

Deviations of the real gas from ideal gas behavior can be calculated exactly when a thermal EOS is known. The derivations are found in textbooks, such as Baehr and Kabelac [11], only the results are summarized here. The specific enthalpy is

$$\begin{aligned} h\left(\rho,T\right) = h_0\left(T_0\right) + \int_{T_0}^{T} c_{p,0}\left(T\right)\,\mathrm{d}T \\ + \frac{p-\rho RT}{\rho} + \int_0^{\rho}\left[\frac{p}{\rho^2} - \frac{T}{\rho^2}\left(\frac{\partial p}{\partial T}\right)_\rho\right]_T \mathrm{d}\rho. \end{aligned} \tag{3.31}$$

Here, h_0 is the ideal gas reference specific enthalpy at T_0 = 298.15 K. The integral on the first line covers the change in specific enthalpy due to heating using the ideal gas isobaric specific heat capacity $c_{p,0}$. The second line calculates the departure from ideal gas behavior from a thermal EOS. The specific inner energy can be computed from the definition of enthalpy as a function of specific enthalpy, pressure, and density as

$$e\left(\rho,T\right) = h\left(\rho,T\right) - \frac{p}{\rho}. \tag{3.32}$$

The isochoric specific heat capacity can be obtained as the differential of specific inner energy with respect to temperature at constant volume

$$c_v\left(\rho,T\right) = c_{v,0}\left(T_0\right) + \int_0^\rho \left[\frac{T}{\rho^2}\left(\frac{\partial^2 p}{\partial T^2}\right)_\rho\right]_T \mathrm{d}\rho \tag{3.33}$$

where $c_{v,0}$ is the ideal gas isochoric specific heat capacity. Calculating instead the differential of the specific enthalpy yields the isobaric specific heat capacity

$$c_p\left(\rho,T\right) = c_v\left(\rho,T\right) + \frac{T}{\rho^2}\frac{\left(\frac{\partial p}{\partial T}\right)_\rho^2}{\left(\frac{\partial^2 p}{\partial \rho^2}\right)_T}. \tag{3.34}$$

The specific entropy of a real fluid is given by

$$\begin{aligned} s\left(\rho,T\right) = s_0\left(T_0\right) &+ \int_{T_0}^T \frac{c_{p,0}\left(T\right)}{T}\,\mathrm{d}T - R\ln\left(\frac{RT\rho}{p_0}\right) \\ &+ \frac{p-\rho RT}{\rho} - \int_0^\rho \frac{1}{\rho^2}\left[\left(\frac{\partial p}{\partial T}\right)_\rho - R\rho\right]_T \mathrm{d}\rho \end{aligned} \tag{3.35}$$

where s_0 is the ideal gas specific entropy at T_0 = 298.15 K. The speed of sound is calculated from

$$a^2\left(\rho,T\right) = \frac{c_p\left(\rho,T\right)}{c_v\left(\rho,T\right)}\left(\frac{\partial p}{\partial \rho}\right)_T, \tag{3.36}$$

the ratio of specific heats is

$$\gamma = \frac{c_p}{c_v}. \tag{3.37}$$

3.2 Properties of Supercritical Fluids

Thermodynamic concepts such as phase coexistence and equilibrium, surface tension, or enthalpy of vaporization, on which subcritical terminology and methods are based, are not applicable beyond the critical point: there is no equilibrium coexistence between a dense and a dilute phase, every supercritical state is homogeneous. But does this mean in turn that the supercritical state *space* is homogeneous? Can concepts of subcritical injection be transferred to injection at supercritical pressures, in particular to transcritical injection?

3.2.1 Pseudo Surface-Boiling in Heat Transfer

A first discussion of supercritical phenomena which resemble certain subcritical observations can be found in 1960s studies of heat transfer to fluids, carried out at that time especially with regard to coolant flow in power plants. Kafengauz and Federov [74, 75] investigated pressure oscillations in forced convection through heated pipes. For subcritical pressures, they found the wall temperature reaching a limit value with increasing heat flux. Reaching this temperature also marks the onset of flow oscillations which could be attributed to surface boiling. However, as the pressure exceeded the fluid critical pressure, they again found a temperature at which oscillations and anomalous heat transfer was witnessed. Clearly, beyond the critical point this could not be a phase change phenomenon. But, as the symptoms were identical to (subcritical) surface boiling, they dubbed the phenomenon *pseudo-(surface) boiling*[3]. While in 2003, Okamoto et al. [120] still called pseudo-boiling a theoretical problem to be solved, the idea was outright rejected by Hall in 1971: In a book chapter on heat transfer near the critical point [57], he called the concept of pseudo-boiling *"irrational and unnecessary because, clearly, two distinct phases do not exist at supercritical pressures"*. He insisted that the scale of the phenomenon will usually be small.

3.2.2 Structure of the Supercritical State Space

But how can a state transition be found in a homogeneous supercritical state space? The p-T diagram describing a fluid state of a sufficiently simple

[3] from greek pseudo, meaning *false, not genuine*

substance is limited to the triple point and the critical point as ends of the coexistence line. What happens beyond the critical point is merely referred to as supercritical[4]. As Simeoni and coworkers put it in their 2010 article in Nature Physics [147] *"according to textbook definitions, there exists no physical observable able to distinguish a liquid from a gas beyond the critical point, and hence only a single fluid phase is defined"*. And, to quote Hall [57], *"clearly, two distinct phases do not exist at supercritical pressures"*.

Consider the process in Fig. 3.2 in which a liquid in (a) is isothermally compressed to (e), then isobarically heated to (d), until, outside (f), it is isothermally expanded to (c). The fluid has been transformed from a classical liquid (a) to a gas (c). The most obvious change will be the drastically reduced density. But where does this happen? Increasing the pressure of a liquid - typically regarded as quasi-incompressible - will not change the density significantly. It appears implausible that suddenly, when p_{cr} is exceeded, the incompressible fluid will suddenly collapse, and indeed, fluid (e) is also called 'liquid' by some researchers (e.g. Younglove [176]), as pointed out in Ch. 2.3. Does this resemblance end with densities or can other typical liquid properties be found among transcritical fluids (e)? Furthermore, does something similar exist between (c) and (d)? And finally, is there a distinct point between (e), (f), (d), and (c), where the density drops again? Are there different kinds of supercritical fluids? How does a liquid differ from a gas, how can both be distinguished from a supercritical fluid?

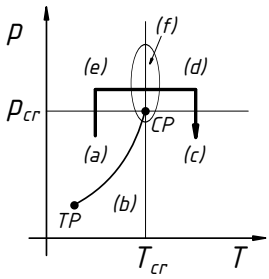

Figure 3.2: Classical structure of fluid states.

It turns out, such a property has been investigated and finally found experimentally by Gorelli, Santoro and coworkers in 2006 for oxygen [51] and by Santoro and Gorelli in 2008 for Argon [140]. Dispersion, i.e. dependence of the speed of sound on frequency, is a characteristic of a liquid but is not seen in a gas. Using inelastic X-ray scattering, they measured dispersion of

[4] As discussed in Ch. 2.3 the actual definitions differ between researchers.

oxygen to see if liquid-like properties can be found beyond the critical point. And indeed, they found dispersion at pressures as high as 1000 p_r at supercritical temperatures. They concluded that *"the extension of the coexistence line beyond the critical point splits the $p-T$ phase diagram of simple fluids into a gas-like and a liquid-like domain, respectively, which differ in the local structure, resembling the subcritical behaviors"*. Figure 3.3 illustrates this. Supplemented with numerical studies and further data from the literature, these results were summarized by Simeoni et al. [147] and commented by McMillan and Stanley [111] in the same issue of Nature Physics.

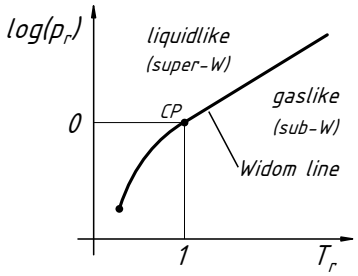

Figure 3.3: Division of the supercritical domain into gas-like and liquid-like, separated by the Widom line.

3.2.3 The Widom Line

The general nature of lines of demarcation beyond a critical point has been studied with a completely different question in mind. Research conducted in the 1990s at Boston University lead to the hypothesis of the existence of a liquid-liquid critical point in supercooled water (additional to the gas-liquid critical point). The group around Stanley [153] was interested in the molecular structure of supercooled water in their study of phase changes and critical phenomena. In 1992, Poole et al. [130] performed molecular dynamics simulations and found first evidence for two distinct liquid phases in supercooled water. This was later supported with additional numerical work by Harrington et al. [59]. Recently, also experimental evidence has been found by Liu et al. [97]. Stanley and coworkers discussed how the existence of a critical point as the end of a phase coexistence line can be inferred from data in the *super*critical region. After all, as Hall [57] had pointed out, there are no distinct phases. However, Sciortino et al. [146] identified a line start-

ing at the critical point[5] and reaching into the supercritical domain which is characterized by the isothermal compressibility reaching a maximum. This supercritical state of high, albeit finite, values for thermodynamic response functions values bears strong similarities to what Oschwald et al. [124] and Zong et al. [178] discussed later.

Stanley suggested this extension of the coexistence line be called Widom line, in honor of Benjamin Widom who first proposed fluid density fluctuation near the critical point [27]. Originally defined as the locus of maximum correlation length (Simeoni et al. [147], May and Mausbach [100]), the concept is interpreted differently by different researchers and furthermore applied to the gas-liquid critical point as well. Generally, all response functions[6] have been considered by Liu et al. [97] and Xu et al. [172]. Other authors distinguished between response functions, e.g. heat capacity c_p: Xu et al. [172], Santoro and Gorelli [140], Ruppeiner at al. [139]; isothermal compressibility K_T: Sciortino et al. [146], Abascal and Vega [4]. The maximum density gradient $(\partial\rho/\partial T)_p$ was considered by Okamoto et al. [120]. Only Brazhkin et al. [26] found that Widom line and specific heat maxima should exactly coincide with the isochore for all fluids, a result different from the other authors, further discussed by May and Mausbach [100]. The latter also criticized that there exists no formal way of determining the Widom line as maximum of correlation length from response functions. They suggested a method of determining the Widom line and found that its proximity to the line of $c_{p,\max}$ is only valid in immediate neighborhood to the critical point. Ruppeiner et al. [139] found there is only marginal deviation farther away.

So far, the notion of an extension of the gas-liquid coexistence line has merely been a qualitative assessment. Gorelli et al. [51] were the first to propose a mathematical description, the Plank-Riedel equation

$$\ln\left(\frac{p}{p_{\mathrm{cr}}}\right) = a + b\frac{T_{\mathrm{cr}}}{T} + c\ln\left(\frac{T}{T_{\mathrm{cr}}}\right). \tag{3.38}$$

Classically a fit of the coexistence line, Gorelli suggests to extrapolate it beyond the critical point. Here, $a = 4.270, b = -4.271$, and $c = 1.141$ were fit to neon, oxygen, and nitrogen fluid data.

Points of distinct supercritical fluid properties in the near critical region had

[5] in fact at each of the discussed critical points: the hypothesized liquid-liquid and the well known liquid-gas critical point

[6] The response functions describe the answer of the thermodynamic system to a stimulus, e.g. the heat capacity relates the change in temperature to added heat, the compressibility characterizes the change in volume when the pressure changes (Stanley [153]).

been reported before, such as the maximum density gradient $(\partial\rho/\partial T)_p$ by Zong and Yang [178], or a maximum thermal diffusivity α by Zong and Yang [178] as well as by Oschwald and Micci [124]. However, they had not been understood to be linked to a demarcation between two different supercritial fluid states.

3.2.4 Pseudo-boiling – Crossing the Widom Line

Little has been published on an actual process where a fluid state passes through the Widom-line and changes its properties from liquid-like to gas-like (or vice versa), illustrated in Fig. 3.4. Sciortino et al. [146] hypothesized that crossing the line of maximum isothermal compressibility could exhibit characteristics similar to a real, subcritical phase transition. Santoro and Gorelli [140] finally went beyond the notion that the Widom line only marks the boundary between liquid-like and gas-like supercritical behavior: Somewhat reluctantly, they stated that it might mark a *"sluggish liquidlike-gaslike transformation mimicking the subcritical liquid-gas phase transition"*.

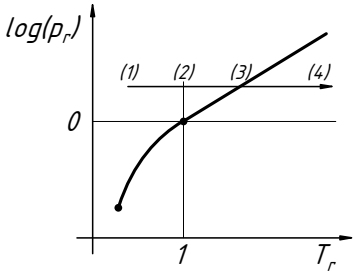

Figure 3.4: Transcritical injection from (1) to (4), passing through the critical (2) and the pseudo-boiling (3) temperature.

Further evidence of a process resembling a state transition in the supercritical domain has been discussed by Oschwald and Micci in 2002 [124]. In their study of transcritical injection of pure nitrogen, they discussed a supercritical continuation of the coexistence line along the set of points of maximum specific heat capacity. Oschwald and Micci suggested crossing this line may explain differences in centerline density distributions dependent on the injection temperature. Zong and Yang [178] independently discuss the same hypothesis. Analyzing nitrogen fluid data, they found that density decreases

sharply close to the critical point when the temperature is increased. Additionally, at the point of maximum $(\partial\rho/\partial T)_p$, a distinct minimum of thermal diffusivity and a maximum of isobaric specific heat capacity can be found. The latter diverges towards the critical point. Zong and Yang even speculated that more thermal energy should be needed to heat up a jet at pressures closer to the critical pressure. However, this thought was not followed further, nor was the position of $c_{p,\max}$ realized to differ from the critical temperature. Mayer et al. [109] suggested that a jet injected at a temperature below maximum c_p might exhibit a denser core than one injected at a higher temperature. Finally, Oschwald et al. are the first to reintroduce the term pseudo-boiling with respect to injection in a 2006 comprehensive review article on experiments carried out at DLR and the AFRL[125]. Here, the pseudo-boiling point is characterized by a maximum in specific heat capacity at supercritical pressures.

So far, no quantitative analysis has been carried out.

3.2.5 Summary

While first evidence has been found in the 1960s pointing towards a supercritical process resembling subcritical boiling, conclusive data supporting these initial guesses could only be achieved with combined numerical and experimental efforts during the last twenty years.

It appears that different sources discussed the same phenomenon from different angles and in different scales since the 1960s. Kafengauz reported on a technical process at supercritical pressure exhibiting properties resembling its subcritical counterpart, 'pseudo-boiling', without knowing anything about its physical nature. Oschwald adopted the term when he described the existence of a line of extremal supercritical fluid properties, without going into details about implications, or the nature of this line, or the nature of the states the line divided. Zong hinted at possible implications of extremal supercritical fluid properties on a heating process, without discussing where or why these extremes be found. Gorelli investigated the molecular nature of supercritical fluids, found that they exhibit liquid-like and gas-like properties, depending on their position relative to an extension of the coexistence line, without discussing process effects or the nature of this boundary. Stanley studied the nature of the line and dubbed it Widom line, without discussing process implications. Finally, Gorelli suggested that crossing from

liquid-like to gas-like through the Widom line might be comparable to a subcritical phase change without discussing implications. At this point we have come full circle to ‘pseudo-boiling’.

3.3 A Quantitative Theory of Pseudo-Boiling

The views discussed in Ch. 3.2 can now be unified. Regard Fig. 3.3. There exists a Widom line as an extension of the coexistence line into the supercritical domain. Super- and sub-Widom fluids behave liquid-like and gas-like, respectively. As these fluids exhibit different physical properties, they can be regarded as different phases, even though the transition is continuous. Along the Widom line, the density gradient with respect to temperature and the specific heat capacity exhibit maxima. A fluid which follows a process passing through the Widom line, Fig. 3.4, thus experiences a significant increase in specific volume while it takes large amounts of energy to change its temperature. This closely resembles subcritical boiling. Whether it can be expected to have a macroscopic effect on technical processes and systems requires a quantitative study of the pseudo-boiling process[7]. A process as illustrated in Fig. 3.4, in which the Widom line is crossed will henceforth be called dia-Widom[8] process.

3.3.1 Choosing a Widom Line Definition

There are a number of definitions in use for the Widom line, as discussed in in Ch. 3.2.2. In this work, the main question is the existence of a supercritical state transition resembling subcritical vaporization. One prime characteristic of the latter is the ability of the fluid to adsorb heat without significantly changing the temperature, the other being the dramatic increase in specific volume at the same time. Thus, for the purpose of this work, the locus of maxima of isobaric specific heat capacity is used to define the Widom line. This coincides with the line of $(\partial\rho/\partial T)_{\max}$ according to Zong and Yang [178]; Fig. 3.5 shows the example of oxygen (data from NIST by Schmidt and Wagner [142]). As this line is also called pseudo-boiling line in the literature, both expressions will be used synonymously. E.g., the supercritical temperature where the isobaric specific heat capacity is maximum, may be called pseudo-boiling temperature T_{pb} or Widom temperature of a certain pressure.

[7] A summary is given in [12].

[8] from greek dia-, meaning *across, through*

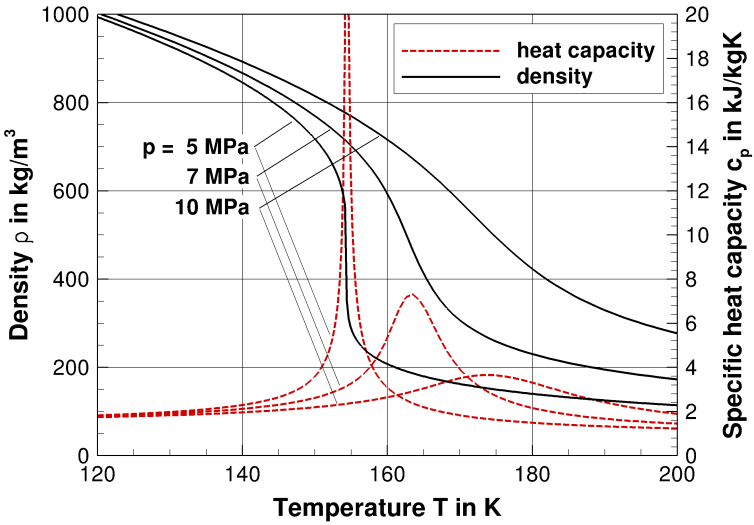

Figure 3.5: Oxygen density and specific heat capacity for sub- (5 MPa) and supercritical (7 and 10 MPa) pressures.

3.3.2 Clausius-Clapeyron Equation in the Critical Limit

Along the coexistence line from triple point to critical point, liquid (subscript L) and gaseous vapor (subscript V) phase can coexist in an equilibrium. The equilibrium conditions then read

$$T_\mathrm{L} = T_\mathrm{V} \tag{3.39}$$

$$p_\mathrm{L} = p_\mathrm{V} \tag{3.40}$$

$$g_\mathrm{L} = g_\mathrm{V} \tag{3.41}$$

where g is the specific Gibbs free enthalpy. It can be expressed in differential form:

$$\mathrm{d}g = v\,\mathrm{d}p - s\,\mathrm{d}T. \tag{3.42}$$

When variables are equal, their respective differentials are equal. Thus,

$$v_\mathrm{L}\,\mathrm{d}p - s_\mathrm{L}\,\mathrm{d}T = v_\mathrm{V}\,\mathrm{d}p - s_\mathrm{V}\,\mathrm{d}T. \tag{3.43}$$

This leads to the Clausius-Clapeyron[9] equation

$$\frac{\mathrm{d}p}{\mathrm{d}T} = \frac{s_\mathrm{V} - s_\mathrm{L}}{v_\mathrm{V} - v_\mathrm{L}} = \frac{1}{T}\frac{h_\mathrm{V} - h_\mathrm{L}}{v_\mathrm{V} - v_\mathrm{L}}. \tag{3.44}$$

The last equality holds as T remains constant during the transition from liquid to gaseous state. The latent heat of vaporization is $\Delta h = h_\mathrm{V} - h_\mathrm{L}$, the increase in specific volume and entropy are $\Delta v = v_\mathrm{V} - v_\mathrm{L}$ and $\Delta s = s_\mathrm{V} - s_\mathrm{L}$, respectively.

For the example of nitrogen ($p_\mathrm{cr} = 3.39$ MPa), Fig. 3.6 shows the development of entropy s and specific volume v across a phase transition; the branches from the bottom left represent liquid fluid data, the branches from the top right correspond to vapor data. Same color means equal pressure. Then, the gap between the liquid and vapor branches of 3.2 MPa and 3.35 MPa, respectively, represents the change Δs and Δv during phase change. Figure 3.6 shows how Δs and Δv decrease when the pressure is increased from 3.20 MPa to 3.35 MPa and 3.50 MPa. Approaching and exceeding the critical point, the process changes from discontinuous to continuous. The heat of vaporization Δh vanishes. No discontinuous increase in volume occurs anymore, i.e. Δv also vanishes. In summary: the discontinuous phase change seizes to exist and is replaced by a continuous, gradual change in properties for isobaric heating at supercritical pressures. How can this be interpreted thermodynamically? Can the Clausius-Clapeyron equation be evaluated when the heat of vaporization has vanished? Watching Δs and Δv as the critical point is approached and passed, both approach zero, i.e. $\Delta s \to 0$ and $\Delta v \to 0$. While evaluating a zero Δh or Δv alone does not make sense, evaluating the ratio of the two does. In the limit of the Clausius-Clapeyron equation Eq. (3.44) towards the critical point, the equation does not become meaningless. Instead, the mathematical limiting procedure turns the difference fraction into a differential,

$$\left(\frac{\mathrm{d}p}{\mathrm{d}T}\right)_\mathrm{sat} = \left(\frac{\Delta s}{\Delta v}\right)_\mathrm{sat} \xrightarrow[\Delta s, \Delta v \to 0]{p, T \to p_\mathrm{cr}, T_\mathrm{cr}} \left(\frac{\mathrm{d}p}{\mathrm{d}T}\right)_\mathrm{cr} = \left(\frac{\mathrm{d}s}{\mathrm{d}v}\right)_\mathrm{cr}, \tag{3.45}$$

where the subscript 'sat' denotes saturation conditions along the coexistence line. The right hand side of the limit Clausius-Clapeyron equation is no longer the ratio of the finite differences between the phases but has become

[9] The naming follows Weigand et al. [167] or Landau and Lifschitz [86]. Some authors refer to Eq. (3.44) as *Clapeyron* equation (Atkins and de Paula [9], Pfennig [128]), and use the term *Clausius-Clapeyron* equation to denote $\mathrm{d}(\ln p)/\mathrm{d}T = \Delta h/(RT^2)$ which can be obtained from Eq. (3.44) assuming that the vapor follows the ideal gas law, and $v_\mathrm{V} >> v_\mathrm{L}$.

the slope instead. The point at which the branches in Fig. 3.6 meet, i.e. where the differences between liquid and vapor seize to exist, is the critical point. At the critical point, thermodynamic response functions, such as the specific heat capacity, diverge (Stanley [153]). Thus, the point where the branches meet is characterized by a maximum in specific heat capacity, $c_{p,\max}$ in Fig. 3.6. The set of points of $c_{p,\max}$ at supercritical pressures is hence a logical continuation of the coexistence line.

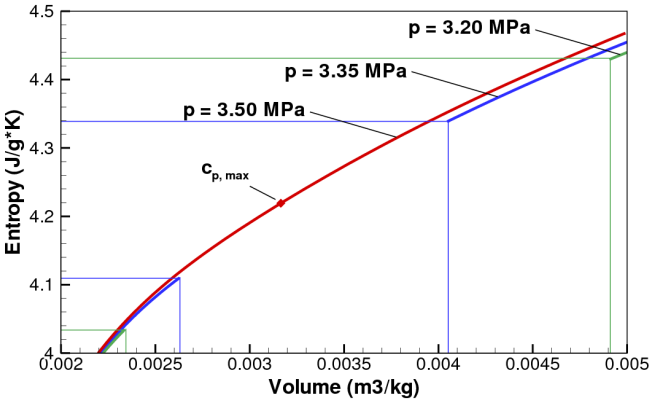

Figure 3.6: Change of specific entropy and specific volume along coexistence line towards and beyond the critical point; nitrogen data from NIST (Span et al. [152]).

3.3.3 Extension of the Coexistence Line

The set of states of $c_{p,\max}$ is not only a logical continuation of the coexistence line, furthermore it is also the chosen definition of the Widom or pseudo-boiling line in this thesis. It is now necessary to investigate these points further away from the critical point. Figure 3.7(a) shows the specific isobaric heat capacity of nitrogen as a function of temperature for a subcritical and three supercritical pressures. A distinct maximum can be seen in the three supercritical curves, reducing in magnitude, moving to higher temperatures, and spreading over a wider temperature range for increasing pressure. Figure 3.7(b) shows how these points of maximum specific isobaric heat capacity are arranged in the fluid p-T diagram[10]: they follow a linear distribution

[10]This has been discussed by the author in 2011 [15].

when plotted in terms of $\log(p)$-T. This distribution is thus of the form

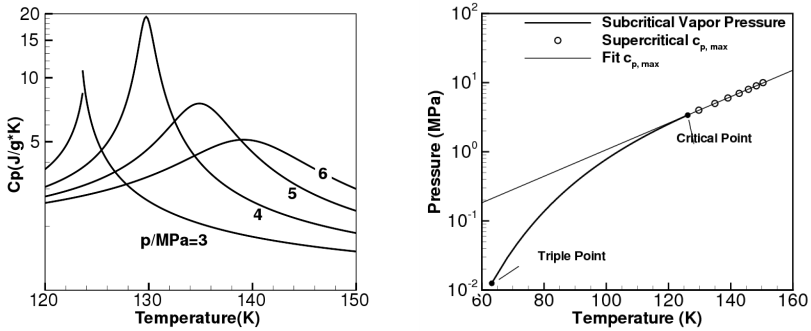

(a) Nitrogen specific heat capacity at subcritical (3 MPa) and supercritical pressures (4, 5, 6 MPa).

(b) Nitrogen vapor pressure curve and supercritical states of maximum specific heat capacity.

Figure 3.7: Nitrogen specific heat maxima beyond the critical point, data from the NIST webbook [94], Span et al. [152].

$$p_{\mathrm{pb}} = p_{\mathrm{cr}} \exp\left(\frac{1}{\theta_{\mathrm{cr}}}\left(T_{\mathrm{pb}} - T_{\mathrm{cr}}\right)\right). \tag{3.46}$$

Here, subscript pb denotes a pseudo-boiling state, i.e. a state on the Widom line. For dimensional reasons, the integration constant $1/\theta_{\mathrm{cr}}$ can be interpreted as the inverse of a characteristic temperature. The equation can be rewritten using dimensionless pairs of temperature and pressure,

$$\frac{p_{\mathrm{pb}}}{p_{\mathrm{cr}}} = \exp\left[\frac{T_{\mathrm{cr}}}{\theta_{\mathrm{cr}}}\left(\frac{T_{\mathrm{pb}}}{T_{\mathrm{cr}}} - 1\right)\right]. \tag{3.47}$$

3.3.4 A New Equation for the Widom Line

So far, a promising equation with one parameter, Eq. (3.47), could be suggested. How can Eq. (3.45) be used to determine θ_{cr} from first principles? Going back to Fig. 3.7(b), one more thing can be found: while the slope $(\,\mathrm{d}\log p/\,\mathrm{d}T)_{\mathrm{sat}}$ is gradually decreasing in the subcritical region, it is constant upon entering a supercritical state and equal to the slope at the critical

point

$$\left(\frac{\mathrm{d}\ln p}{\mathrm{d}T}\right)_{\mathrm{pb}} = \left(\frac{\mathrm{d}\ln p}{\mathrm{d}T}\right)_{\mathrm{cr}} = \frac{1}{\theta_{\mathrm{cr}}} = \text{const.} \tag{3.48}$$

Furthermore, from calculus,

$$\frac{\mathrm{d}\ln p}{\mathrm{d}T} = \frac{1}{p}\frac{\mathrm{d}p}{\mathrm{d}T}. \tag{3.49}$$

Combining Eqs. (3.45), (3.48), and (3.49) leads to an expression for θ_{cr},

$$\frac{1}{\theta_{\mathrm{cr}}} = \left(\frac{\mathrm{d}\ln p}{\mathrm{d}T}\right)_{\mathrm{cr}} = \left(\frac{1}{p}\frac{\mathrm{d}p}{\mathrm{d}T}\right)_{\mathrm{cr}} = \left(\frac{1}{p}\frac{\mathrm{d}s}{\mathrm{d}v}\right)_{\mathrm{cr}}. \tag{3.50}$$

Inserting this into Eq. (3.47) yields a new equation for the Widom line

$$\frac{p_{\mathrm{pb}}}{p_{\mathrm{cr}}} = \exp\left[\frac{T_{\mathrm{cr}}}{p_{\mathrm{cr}}}\left(\frac{\mathrm{d}s}{\mathrm{d}v}\right)_{\mathrm{cr}}\left(\frac{T_{\mathrm{pb}}}{T_{\mathrm{cr}}} - 1\right)\right] \tag{3.51}$$

or

$$\frac{p_{\mathrm{pb}}}{p_{\mathrm{cr}}} = \exp\left[\frac{T_{\mathrm{cr}}}{p_{\mathrm{cr}}}\left(\frac{\mathrm{d}p}{\mathrm{d}T}\right)_{\mathrm{cr}}\left(\frac{T_{\mathrm{pb}}}{T_{\mathrm{cr}}} - 1\right)\right]. \tag{3.52}$$

Note that Eqs. (3.51) and (3.52) do not contain any fitted parameters. All terms can be calculated from thermodynamic fluid data. Furthermore, variables are not expressed in an absolute form but always with respect to critical values. This suggests the equations hold for all fluids within the applicability of the corresponding states principle.

Figure 3.8 is a summary of these results. Points of maximum heat capacity have been extracted from the NIST [94] database for argon (Tegeler et al. [157], water (Wagner et al. [165]), nitrogen (Span et al. [152]), and oxygen (Schmidt et al. [142]). These data have then been compiled in the diagram. The coefficient of the inner brackets $A = (T_{\mathrm{cr}}/\theta_{\mathrm{cr}})$ in Eq. (3.51) has been determined using NIST data for nitrogen as

$$A = \frac{T_{\mathrm{cr}}}{\theta_{\mathrm{cr}}} = \frac{T_{\mathrm{cr}}}{p_{\mathrm{cr}}}\left(\frac{\mathrm{d}s}{\mathrm{d}v}\right)_{\mathrm{cr}} = 5.55. \tag{3.53}$$

Equation (3.51) is found to be accurate for nitrogen for pressures of up to 3 p_{cr}. Furthermore, the accuracy for oxygen and argon supports the notion of generality assumed from the nondimensionality of the equation. Apparently, A is not only a species constant but appears to be valid for a range of fluids. The polar substance water, chosen for its irregular properties, de-

viates stronger. Gorelli's Eq. (3.38) has been included. The new equation Eq. (3.51) is found to be more accurate than the extrapolated Plank-Riedel fit in the shown range.

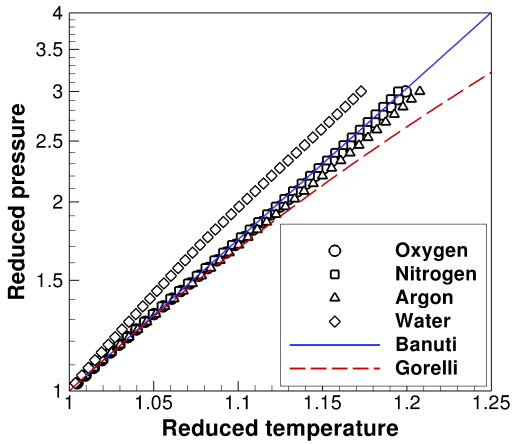

Figure 3.8: Comparison of Eq. (3.51) (Banuti), Eq. (3.38) (Gorelli) with states of maximum isobaric specific heat capacity for oxygen, nitrogen, argon, and water.

3.3.5 Supercritical Heat of Vaporization

Now that a quantitative description of the Widom line is established in Eq. (3.51), it is time to look at the isobaric process crossing it. Figure 3.9 shows, for the example of oxygen, the evolution of enthalpy through a temperature interval. For oxygen, $T_{\mathrm{cr}} = 154.6$ K, $p_{\mathrm{cr}} = 5.0$ MPa. Shown are the data at sub- (4 MPa) and supercritical (6 MPa) pressure. The similarity between both processes in the immediate vicinity of the critical point is apparent. The difference at supercritical pressure is that the changes are smooth rather than discontinuous, and take place within a temperature range instead of being isothermal.

Up front, suitable definitions for the beginning and the end of the transition process need to be established. This can again be split into two main questions: How can an analogue to the enthalpy of vaporization be defined? At which temperature does the transition start, at which does it end?

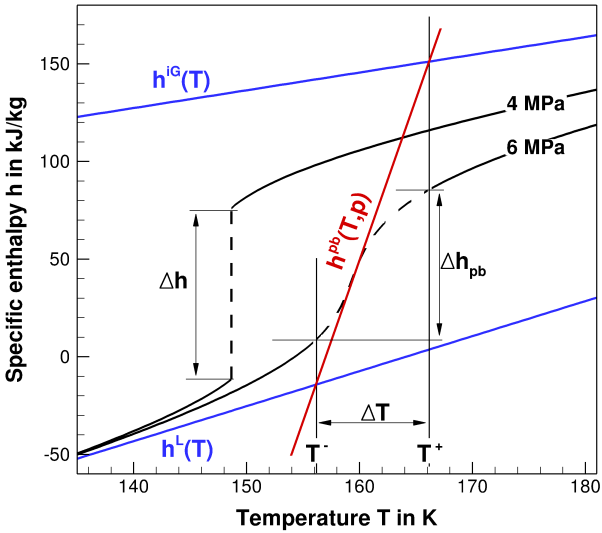

Figure 3.9: Specific enthalpy vs temperature of oxygen at sub- and supercritical pressure. Definition of supercritical phase change enthalpy Δh_{pb} and temperature interval ΔT. Oxygen data from NIST, Schmidt and Wagner [142].

Let T^- be the (lower) onset temperature of the transition, T^+ is the end temperature. Then, $\Delta T = (T^+ - T^-)$ is the interval, over which the transition takes place. Correspondingly, $h^- = h(T^-)$, $h^+ = h(T^+)$ are the associated respective specific enthalpies, $\Delta h_{\mathrm{pb}} = (h^+ - h^-)$ is the specific enthalpy difference. This difference Δh_{pb}, with subscript pb for pseudo-boiling, is understood here as the supercritical analogue to the subcritical latent heat of vaporization. Before finding suitable definitions for T^+, T^-, the involved specific enthalpy contributions will be analyzed.

Heating Enthalpy vs. Vaporization Enthalpy

While a subcritical phase change takes place isothermally, this is no longer true for the supercritical counterpart. An important realization is thus that in the supercritical case, supplied energy is used for two processes: First, to overcome intermolecular attraction. Second, supplied energy is also required

to raise the fluid temperature from T^- to T^+. The former contribution will be called *structural*, subscript st, the latter *thermal*, subscript th. Figure 3.10 illustrates the reasoning.

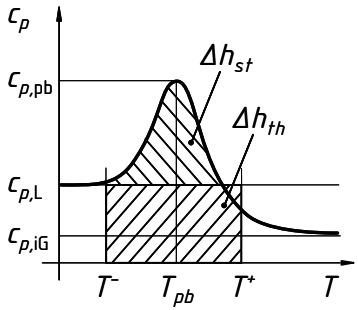

Figure 3.10: Specific isobaric heat capacity and pseudo-boiling specific enthalpy contributions.

The pseudo-boiling specific enthalpy difference Δh_{pb} encompasses both the heating and the structural contribution when raising the temperature isobarically across the Widom-line from T^- to T^+:

$$\Delta h_{\mathrm{pb}} = h(T^+) - h(T^-) = \int_{T^-}^{T^+} c_p(T)\,\mathrm{d}T. \tag{3.54}$$

This corresponds to the area under the thickly drawn c_p distribution between T^- and T^+ in Fig. 3.10. In order to characterize the structural effect of the Widom line crossing, the heating contribution needs to be removed from the treatment. The liquid heat capacity $c_{p,\mathrm{L}}$ is taken as a convenient reference, as it can be considered almost constant over a wide pressure range for a given simple fluid, even when no theoretical expression is known (Hirschfelder et al. [64]). For all practical purposes here,

$$c_{p,\mathrm{L}} = c_p\left(p = p_{\mathrm{cr}},\, T = \frac{3}{4}T_{\mathrm{cr}}\right). \tag{3.55}$$

If the fluid were to remain the reference liquid, with a constant $c_p(T) \equiv c_{p,\mathrm{L}}$, the specific enthalpy needed to heat the fluid from T^- to T^+ would be

$$\Delta h_{\mathrm{th}} = c_{p,\mathrm{L}}\Delta T. \tag{3.56}$$

This is the area below $c_{p,\mathrm{L}}$ between T^- and T^+. The remaining structural contribution, needed to overcome intermolecular attraction, is then the difference between the complete specific enthalpy difference and the thermal contribution,

$$\Delta h_{\mathrm{st}} = \Delta h_{\mathrm{pb}} - \Delta h_{\mathrm{th}}. \tag{3.57}$$

This is the area between the horizontal $c_p = c_{p,\mathrm{L}}$ and the specific heat capacity distribution.

Asymptote-Based Temperature Interval

Actual values for the temperature interval need to be found. The process is continuous, any definition of an onset and termination temperature is to some extent arbitrary. Here, an approach based on intersections of specific enthalpy asymptotes will be introduced[11]. This is best explained using Fig. 3.10. Approaching the pseudo-boiling temperature T_{pb}, c_p diverges from its liquid value $c_{p,\mathrm{L}}$. By definition, $c_{p,\max} = c_{p,\mathrm{pb}}$ is reached at $T = T_{\mathrm{pb}}$. For further increasing temperatures, an ideal gas heat capacity $c_{p,\mathrm{iG}}$ is approached. Figure 3.9 shows how this affects the specific enthalpy, being the temperature integral of the specific isobaric heat capacity: for lower and higher temperatures, the liquid and ideal gas limiting slopes are approached, respectively. The biggest change occurs at the pseudo-boiling temperature where the slope of $h(T)$ is maximum. Thus, three characteristic specific heat capacities can be identified in this process, corresponding to the slopes of three tangents in the $h(T)$ diagram. These will be denoted with superscripts to avoid ambiguities. The asymptotic function of the low temperature reference liquid heat capacity, Eq. (3.55), i.e. the liquid reference specific enthalpy function, is

$$h^{\mathrm{L}}(T) = c_{p,\mathrm{L}} T + h_{0,\mathrm{L}}, \tag{3.58}$$

where $h_{0,\mathrm{L}} = h\left(p = p_{\mathrm{cr}},\, T = \frac{3}{4} T_{\mathrm{cr}}\right)$, consistent with Eq. (3.55). The ideal gas asymptote $h^{\mathrm{iG}}(T)$ can be calculated from the isobaric specific heat capacity of a calorically perfect gas

$$c_{p,\mathrm{iG}} = \frac{\gamma R}{\gamma - 1}. \tag{3.59}$$

[11] Alternative definitions are possible, e.g. reaching a certain fraction of the maximum heat capacity or the temperature at which the fluid heat capacity falls below the liquid value after the peak.

The asymptote function then is

$$h^{\mathrm{iG}}(T) = \frac{\gamma R}{\gamma - 1} T. \tag{3.60}$$

The third specific enthalpy function is the tangent at the pseudo-boiling point. Its slope $(\partial h/\partial T)_p = c_p$ is the maximum $c_{p,\max} = c_{p,\mathrm{pb}}$ used to characterize the pseudo-boiling or Widom line. The corresponding function can then be written as

$$h^{\mathrm{pb}}(T) = c_{p,\mathrm{pb}}(T - T_{\mathrm{pb}}) + h_{\mathrm{pb}}. \tag{3.61}$$

where $h_{\mathrm{pb}} = h(T_{\mathrm{pb}})$. Now, let the temperature interval be defined by the intersection of the specific enthalpy functions, compare to Fig. 3.9:

$$T^- = \left\{ T \,\middle|\, h^{\mathrm{L}}(T) = h^{\mathrm{pb}}(T) \right\}, \tag{3.62}$$

$$T^+ = \left\{ T \,\middle|\, h^{\mathrm{iG}}(T) = h^{\mathrm{pb}}(T) \right\}. \tag{3.63}$$

Values for the temperatures can be readily calculated by equating Eqs. (3.58) and (3.61) for T^-

$$T^- = \frac{h_{0,\mathrm{L}} - h_{0,\mathrm{pb}} + c_{p,\mathrm{pb}} T_{\mathrm{pb}}}{c_{p,\mathrm{pb}} - c_{p,\mathrm{L}}} \tag{3.64}$$

and Eqs. (3.60) and (3.61) for T^+

$$T^+ = \frac{h_{0,\mathrm{pb}} - c_{p,\mathrm{pb}} T_{\mathrm{pb}}}{\frac{\gamma R}{\gamma - 1} - c_{p,\mathrm{pb}}}. \tag{3.65}$$

The definition is consistent with subcritical phase changes: At subcritical pressures $c_{p,\mathrm{pb}} \to \infty$, thus

$$T^- = T^+ = T_{\mathrm{sat}} \tag{3.66}$$

and

$$\Delta h_{\mathrm{pb}} \equiv \Delta h \tag{3.67}$$

where Δh is the subcritical latent heat of vaporization. Finally, this approach also suggests a maximum temperature at which this behavior might seize to play a role, namely the intersection of the ideal gas and the liquid asymptote

$$T_{\max} = \frac{h_{0,\mathrm{L}}}{\frac{\gamma R}{\gamma - 1} - c_{p,\mathrm{L}}}. \tag{3.68}$$

A Pseudo-Boiling Parameter

A mere difference in enthalpy is insufficient to characterize a supercritical state transition, as it spreads over a finite temperature range: given a large enough temperature range, drastic changes in enthalpy are also possible in ideal gases. The pseudo-boiling phenomenon, however, relies on an exceptionally large change in enthalpy over a small temperature interval. The structural contribution is of primary interest. A parameter thus needs to be a measure of this ratio in order to evaluate the amount of irregularity. This specific heat capacity of supercritical pseudo-boiling can be written

$$B_1^{\mathrm{dim}} = \frac{\Delta h_{\mathrm{st}}}{\Delta T}. \tag{3.69}$$

A dimensionless supercritical boiling parameter can be formulated by choosing the liquid specific heat capacity as reference,

$$B_1 = \frac{\Delta h_{\mathrm{st}}/\Delta T}{c_{p,\mathrm{L}}}. \tag{3.70}$$

The denominator $c_{p,\mathrm{L}}$ suggests an alternative formulation based solely on a ratio of specific heats. In order to emphasize the structural contribution of the state transition over mere heating, the excess specific heat $c_{p,\mathrm{pb}} - c_{p,\mathrm{L}}$ is used instead of just the maximum specific heat. This parameter then reads

$$B_2 = \frac{c_{p,\mathrm{pb}}}{c_{p,\mathrm{L}}} - 1. \tag{3.71}$$

Finally, a third formulation can be introduced, comparing the structural enthalpy difference to the thermal contribution

$$B_3 = \frac{\Delta h_{\mathrm{st}}}{\Delta h_{\mathrm{th}}} = \frac{\Delta h_{\mathrm{pb}}}{\Delta h_{\mathrm{th}}} - 1. \tag{3.72}$$

It turns out Eqs. (3.70) and (3.72) are in fact equivalent because of having chosen $c_{p,\mathrm{L}}$ as constant reference; compare to Eqs. (3.55) and (3.56):

$$B_1 = \frac{\Delta h_{\mathrm{st}}}{c_{p,\mathrm{L}}\Delta T} = \frac{\Delta h_{\mathrm{st}}}{\Delta h_{\mathrm{th}}} = B_3. \tag{3.73}$$

The second parameter B_2 can also be related to the others:

$$B_2 = \frac{c_{p,\mathrm{pb}}}{c_{p,\mathrm{L}}} - 1 = \frac{c_{p,\mathrm{pb}}\Delta T}{c_{p,\mathrm{L}}\Delta T} - 1 \sim \frac{\bar{c}_p \Delta T}{c_{p,\mathrm{L}}\Delta T} = \frac{\Delta h_{\mathrm{pb}}}{\Delta h_{\mathrm{th}}} = B_1. \tag{3.74}$$

when $\bar{c}_p$ is understood as the average of $(c_p(T) - c_{p,\mathrm{L}})$ over the interval ΔT. As Fig. 3.7 shows, the heat capacity distribution widens for higher pressures while the peak value is reduced. Thus, the integral of c_p over the appropriate temperature interval, i.e. enthalpy difference, is implicitly contained in the value of the heat capacity peak. The parameters B_1 and B_2 are shown in Fig. 3.11.

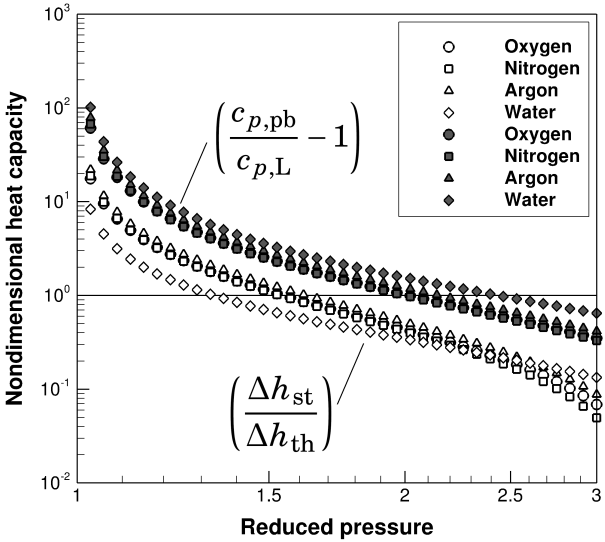

Figure 3.11: Supercritical boiling parameters. Open symbols correspond to enthalpy based evaluation B_1 and B_3, Eqs. (3.71) and (3.72); filled symbols correspond to heat capacity based evaluation, B_3, Eq. (3.71).

Both parameters, the enthalpy based B_1 and the heat capacity based B_2, share the same general trend. They diverge when approaching the critical point as the thermal contribution vanishes at subcritical conditions; they approach zero for higher reduced pressures when the peak in c_p is less and less pronounced. It is striking that the values for each parameter are almost identical for a range of simple fluids. Again, the polar water deviates most. Up to a reduced pressure of 2.5,

$$B_2 \approx 5B_1. \tag{3.75}$$

Quantitatively, Fig. 3.11 shows that the pseudo-boiling phenomenon does indeed have a pronounced effect: in the regarded range, the enthalpy needed to raise the real fluid temperature through the Widom temperature exceeds the enthalpy required to merely heat the reference liquid significantly. At reduced pressures as high as 1.5, thermal and structural contribution are identical, i.e. *twice* the amount of energy is required to pass through the Widom line as could be expected from mere liquid heating alone. At $p_\mathrm{r} = 3$, the surplus still amounts to 10%.

Summarizing, when energy is added, it is used for

$$B_1 \rightarrow \begin{cases} < 0 & : \text{heating,} \\ 1 & : \text{heating and molecular attraction equally,} \\ \infty & : \text{overcoming molecular attraction.} \end{cases} \tag{3.76}$$

Unfortunately, the determination of the enthalpy based B_1 is rather involved, it requires the determination of the pseudo-boiling state, the liquid reference state, the determination of the temperature interval. It thus appears that B_2, the pseudo-boiling ratio of specific heats, is probably the more convenient formulation for practical evaluation. It greatly simplifies the calculation of the parameter, as only two values need to be looked up: the liquid limit heat capacity and the maximum heat capacity for a given pressure. Then, estimating the enthalpy ratio B_1 using Eq. (3.75), the significance of the pseudo-boiling effect for a given process can be assessed.

3.4 Implications for Transcritical Injection

3.4.1 Transcritical Fluid Boundary

Classical injection processes have been discussed in Ch. 2.2.1. These consisted of heterogeneous (liquid-gas), and homogeneous (gas-gas and liquid-liquid) injection. Classical quasi-isobaric jet break-up is a purely mechanical phenomenon where the shear layer between injectant and surroundings spreads until it reaches the center of the jet. Constant or mildly changing properties (e.g. obeying the ideal gas law) are assumed.

In homogeneous injection, homogeneous properties are assumed throughout the flow field. The potential core is the unperturbed region inside the jet. Dye can be used to distinguish the jet from its surroundings (see Villermaux [163]) in liquid-liquid injection. In liquid-gas injection, the surface of the liquid is a distinct and well defined boundary. At any point, the properties are either liquid or gaseous. A smooth decline in axial density is owed to the *temporal* mean flow: As the jet breaks up and the spray dilutes, less and less liquid particles are seen at a particular point in space.

In transcritical injection, no clear demarcation exists anymore. In pure fluid injection, the fluid is chemically identical throughout the flow field. At supercritical pressure, no phase equilibrium can exist, and thus no interface, no surface tension, no heat of vaporization. Instead, a smooth transition between liquid-like high density and gas-like low density fluid develops (Kuo [81], Yang [173]). This can be an actual physical occurrence instead of an artifact of temporal averaging.

The question remains, also in the analysis of experiments, of how the boundary of the jet can be determined. In experiments, shadowgraphs are often analyzed; the position of a distinct change between dark and light marks the outline of the jet. In numerics, the actual density distribution is known quantitatively. Often, the radial position at a given axial slice where the density has dropped to half the maximum value at the centerline is used to determine jet spreading (full width at half maximum, FWHM), or the arithmetic mean of injection and chamber density (e.g. Jarczyk [70]). The resulting discrepancies between computation and measurement make comparison difficult. Bellan [18] introduced a different definition of the boundary to remedy this. She suggested to use the location of the maximum density gradient *"because this is what is optically measured in an experiment"*.

3.4.2 Thermodynamic Meaning

The density gradient Bellan referred to is a spatial density gradient, $(\partial\rho/\partial x)$. In this thesis, the thermal density gradient $(\partial\rho/\partial T)$ has been discussed as a characteristic of the Widom line. Both are related via the spatial temperature gradient,

$$\frac{\partial \rho}{\partial x} = \frac{\partial \rho}{\partial T}\frac{\partial T}{\partial x}. \tag{3.77}$$

Determining the position where the gradient becomes maximum requires the spatial derivative of the spatial density gradient

$$\frac{\partial}{\partial x}\left(\frac{\partial \rho}{\partial x}\right) = \frac{\partial}{\partial x}\left(\frac{\partial \rho}{\partial T}\frac{\partial T}{\partial x}\right) = \frac{\partial T}{\partial x}\frac{\partial}{\partial x}\left(\frac{\partial \rho}{\partial T}\right) + \frac{\partial \rho}{\partial T}\frac{\partial}{\partial x}\left(\frac{\partial T}{\partial x}\right). \tag{3.78}$$

Assuming a linear temperature profile, e.g. through the shear layer,

$$\frac{\partial T}{\partial x} = \mathscr{C}, \tag{3.79}$$

then leads to

$$\frac{\partial}{\partial x}\left(\frac{\partial \rho}{\partial x}\right) = \mathscr{C}\frac{\partial}{\partial x}\left(\frac{\partial \rho}{\partial T}\right), \tag{3.80}$$

i.e., the maxima in spatial and thermodynamic density gradient will exactly coincide.

But how appropriate is this assumption? Figure 3.12 shows contour plots of computations performed by Jarczyk[12] [70], treating injection of cryogenic nitrogen into a nitrogen environment at supercritical pressure. The cases correspond to experiments performed by Mayer et al. [109] which will be discussed in detail in Ch. 6.1.

Figure 3.12(a) shows an outline of a jet as the isosurface (in red) of the arithmetic mean density of injected and surrounding fluid. Figure 3.12(b) shows the spatial density gradient, i.e. the outline of the jet corresponds to the maxima (in black) according to Bellan [18]. Figure 3.12(c) shows the position of the maximum heat capacity, i.e. the position at which the injected fluid has reached the pseudo-boiling state with an associated maximum thermal density gradient, i.e. the criterion suggested here. Finally, Fig. 3.12(d) shows a superposition of spatial density gradient and heat capacity plots Figs. 3.12(b) and 3.12(c). It reveals that these criteria do indeed coincide for

[12] née Poschner

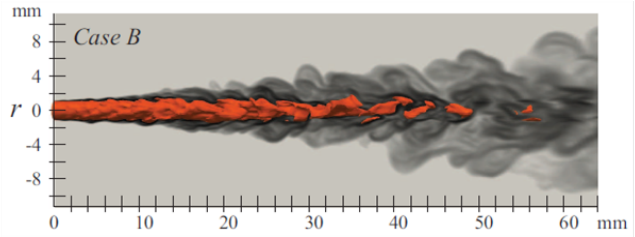

(a) Contour of density gradient, black is maximum, grey is the minimum value. Isosurface (red) of arithmetic mean of injected and surrounding density, from Jarczyk [70].

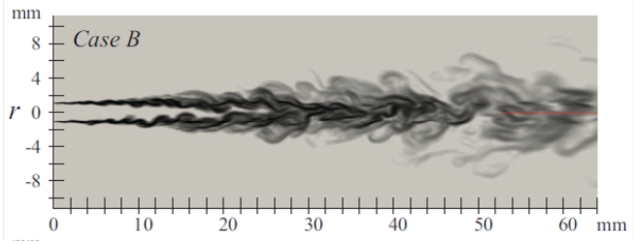

(b) Density gradient, from Jarczyk [70]. Black is maximum, grey is the minimum value.

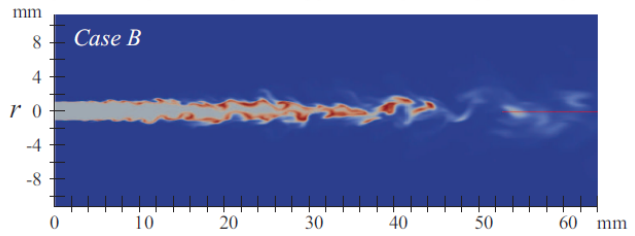

(c) Isobaric specific heat capacity, from Jarczyk [70]. Red is maximum, blue is the minimum value.

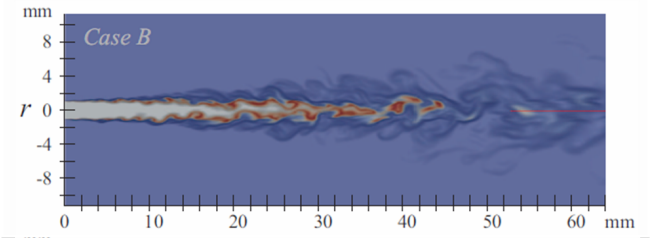

(d) Superposition of specific heat capacity and density gradient plots, Figs. 3.12(c) and 3.12(b). Modified, from Jarczyk [70].

Figure 3.12: Snapshots of cryogenic pure fluid injection, Jarczyk [70]. N_2 at 126.9 K injected into N_2 at 298 K, chamber pressure is 3.97 MPa.

the shown case; the thus determined outlines of the jet are a bit smaller than the average density position, Fig. 3.12(a).

Using the pseudo-boiling state as a criterion to define a supercritical fluid boundary is not only a unique definition: It has inherent thermodynamic meaning. As discussed in Ch. 3.2.2, pseudo-boiling occurs across the Widom line, the demarcation between supercritical liquid-like and gas-like states. A supercritical heat capacity of vaporization has been attributed to a dia-Widom process in Ch. 3.3.5. Thus, Bellan's definition actually cut to the core of the thermodynamic problem: It associates the visual boundary to the actual supercritical transition. Linking the boundary to the pseudoboiling state furthermore allows for a very efficient determination, as only temperatures need to be evaluated and no gradients computed.

Applying Bellan's definition to the problem of transcritical injection, the boundary of the jet is hence the position where the pseudo-boiling temperature T_{pb} is reached. Accordingly, the dense core ends where this temperature is attained on the centerline. This in turn implies yet something more: while classical break-up of isobaric injection was characterized by growing shear layers, i.e. mechanical interaction, transcritical injection also depends on the thermodynamic behavior of the injectant. The main difference is: mechanical interaction starts at the injector plane, thermal interaction, i.e. heating to T_{pb}, can start in the injector *before even entering* the chamber.

3.4.3 A Thermal Break-Up Mechanism

The picture of transcritical injection has changed: The initial Eulerian view is sketched in Fig. 3.13(a). Strictly, this corresponds to a shear layer between immiscible, isolated fluids. However, diffusion and heat conduction act in the boundary of the jet, illustrated in Fig. 3.13(b). The transition is gradual, no distinct surface exists. Now, it has been argued that reaching the pseudo-boiling temperature T_{pb} distinguishes a supercritical boundary and thus indicates the end of the core. Unlike build up of a shear layer, heating of the jet can already start within the injector. Fig. 3.13(c) illustrates this. If the jet is sufficiently heated before entering the chamber, the end of the dense core L_{D} can be reached before the mechanical interaction reaches the centerline. In cases with high heat loads inside the injector, L_{D} may therefore be significantly shorter than L_{C}. This thermal break-up is effectively a novel jet break-up mechanism, relevant for transcritical injection.

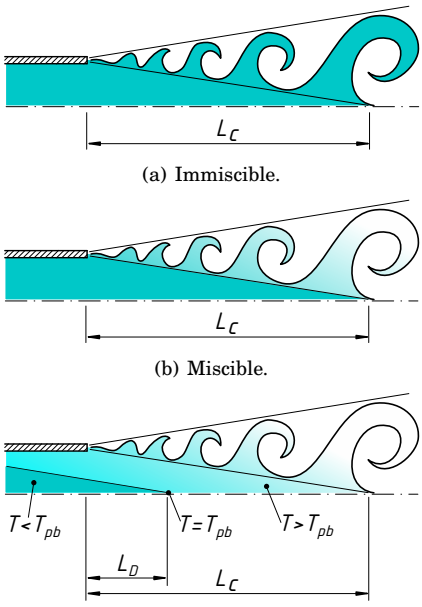

(a) Immiscible.

(b) Miscible.

(c) Thermal.

Figure 3.13: Supercritical break-up.

Associating the pseudo-boiling temperature with the boundary of a supercritical fluid allows a quantitative thermodynamic analysis. The specific enthalpy required to heat a fluid from T_{in} to T_{pb} and thus cause a break-up (subscript bu) is then

$$\Delta h_{\mathrm{bu},T_{\mathrm{in}}} = h(T_{\mathrm{pb}}) - h(T_{\mathrm{in}}) = \int_{T_{\mathrm{in}}}^{T_{\mathrm{pb}}} c_p(T)\,\mathrm{d}T. \tag{3.81}$$

For a discrete mass m, such as a droplet, the required enthalpy is

$$\Delta H_{\mathrm{bu},T_{\mathrm{in}}} = H(T_{\mathrm{pb}}) - H(T_{\mathrm{in}}) = m \int_{T_{\mathrm{in}}}^{T_{\mathrm{pb}}} c_p(T)\,\mathrm{d}T. \tag{3.82}$$

Finally, for continuous injection of a mass flow $\dot{m}$, the enthalpy per unit time

required to heat a stream from T_{in} to T_{pb} is

$$\Delta\dot{H}_{\mathrm{bu},T_{\mathrm{in}}} = \dot{H}(T_{\mathrm{pb}}) - \dot{H}(T_{\mathrm{in}}) = \dot{m} \int_{T_{\mathrm{in}}}^{T_{\mathrm{pb}}} c_p(T)\,\mathrm{d}T. \tag{3.83}$$

The initial temperature T_{in} may be the injection temperature of a cryogenic jet, or the initial bulk temperature of a droplet. Figure 3.11 shows that the pseudo-boiling parameter B_1, Eq. (3.70), decreases for growing pressures. Does this mean that less energy is required to reach the pseudo-boiling state for a given injection temperature? Figure 3.14 shows that this conclusion is wrong. Plotted is the specific enthalpy $\Delta h_{\mathrm{bu},T_{\mathrm{in}}}$ required to heat the fluid to pseudoboiling conditions as a function of the injection temperature T_{in}, for a number of supercritical pressures (data from NIST). For a given injection temperature T_{in}, the required specific enthalpy $\Delta h_{\mathrm{bu},T_{\mathrm{in}}}$ grows for increasing pressure: While the c_p peak to overcome gets flatter with rising pressure, the associated temperature T_{pb} at which this occurs, rises. The fluid then has to be heated more, before the Widom line is actually reached. Injection in the vicinity of the pseudo-boiling temperature (in this diagram the temperature at which the abscissa is intersected) is very sensitive to minor temperature variations, at least for $p_{\mathrm{r}} < 2$, corresponding to 10 MPa.

This is in essence what the pseudo-boiling parameter B_1, shown in Fig. 3.11, measures: an enthalpy difference per temperature interval. A non vanishing B_1 thus goes along with a large change in slope in Fig. 3.14 when intersecting the $\Delta h_{\mathrm{bu},T_{\mathrm{in}}} = 0$ line. In Figs. 3.14(a) and 3.14(b) virtually no inflection point is discernible for the respective highest pressure when passing through the abscissa. This corresponds to $p_{\mathrm{r}} = 14./5. = 2.8$ for oxygen and $p_{\mathrm{r}} = 10./3.5 = 2.86$ for nitrogen. Figure 3.11 shows that this corresponds to $B_1 \approx 0.2$. As insinuated before, this is apparently small enough for a pseudo-boiling effect to be neglected.

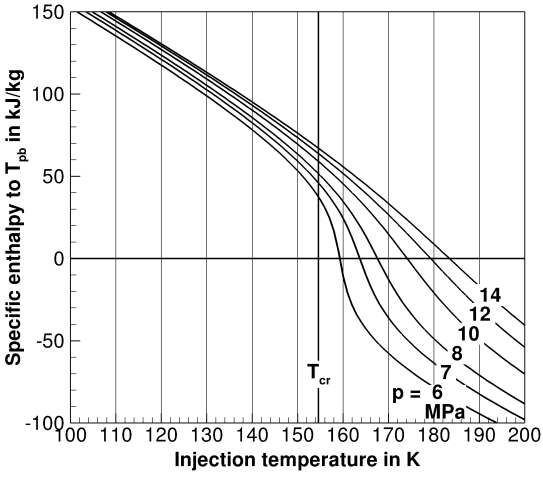

(a) Oxygen.

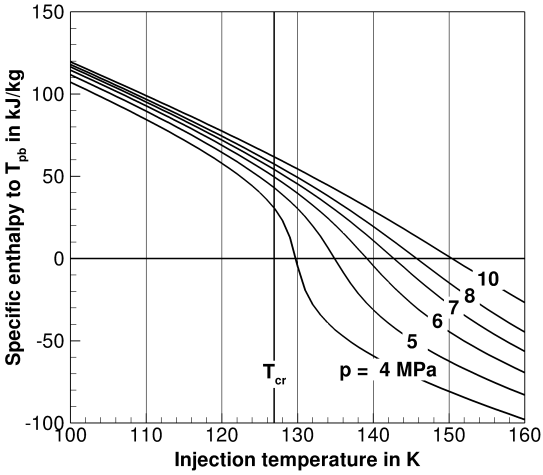

(b) Nitrogen.

Figure 3.14: Specific enthalpy required to reach the pseudo-boiling state, associated with the supercritical fluid boundary. Data from NIST, nitrogen (Span et al. [152]), and oxygen (Schmidt and Wagner [142]).

3.5 Conclusion

A literature survey showed that, for pure fluids, substantial property differences exist between supercritical liquid-like and gas-like states, divided by the Widom or pseudo-boiling line. In this chapter, a new equation Eq. (3.51) for this demarcation has been introduced utilizing a generalization of the Clausius-Clapeyron equation towards the critical point[13]. It is more accurate than previously published equations and does not require fitted parameters.

The first quantitative analysis of pseudo-boiling, the transition between liquid-like and gas-like supercritical states, has been carried out. It has been shown that this phenomenon increases the expected amount of energy to heat a fluid across the Widom line. Changes when passing through the critical temperature or pressure are negligible compared to the changes found for pseudo-boiling. Hence, T_{cr} as a marker of a state transition loses its significance beyond the critical point as may be replaced by T_{pb}, the temperature at pseudo-boiling. Pseudo-boiling becomes less pronounced for higher pressures and is negligible for $p_{\mathrm{r}} > 2.8$.

By adopting the maximum density gradient as a condition for the boundary of a supercritical fluid, a thermodynamic condition of supercritical state change can be given: the boundary is situated where pseudo-boiling occurs at T_{pb}. This is equivalent to reaching the Widom line where the heat capacity exhibits a maximum. Using this definition, the radius or the lifetime of a supercritical droplet are uniquely describable. The criterion is process independent and only depends on the thermodynamic state of the fluid, much like at subcritical pressures. The criterion's inherent thermodynamic meaning, i.e. nonlinear pseudo-boiling, becomes less pronounced towards higher pressures, becoming negligible for $p_{\mathrm{r}} > 2.8$. Typically operated at lower pressures, it remains highly relevant for current rocket engines and injection experiments as main application of the work described in this thesis. Furthermore, the line of maximum density gradients remains useful as a unique reference state beyond the critical point.

Finally, this can be used to suggest conditions for a novel jet disintegration mechanism: thermal break-up. As heat transfer can already act on the jet inside the injector, the bulk jet might reach the pseudo-boiling temperature T_{pb} and dissolve before the potential core is consumed by the expanding shear layer.

[13] This is an extension of earlier work by the author [15].

4 The DLR CFD Code TAU for Ideal Gases

4.1 Overview

The baseline ideal gas flow solver is the DLR TAU Code. Only a brief overview is given here. More detailed and comprehensive descriptions can be found on the DLR TAU code website [3] and in Gerhold et al. [48], Mack and Hannemann [98], Hannemann [58], and Karl [76]. TAU is a hybrid grid, Godunov-type finite volume, compressible flow solver. It has been verified for a variety of steady and unsteady flow cases, ranging from sub- to hypersonic Mach numbers.

A wide range of models and options is available, here only a discussion of the used model will be given.

4.2 Equations

4.2.1 Navier-Stokes

A mixture of chemically reacting ideal gases is governed by the Navier-Stokes equations. In integral form, they read

$$\frac{\partial}{\partial t}\iiint\limits_{V}\vec{U}\,\mathrm{d}V+\iint\limits_{\partial V}\vec{F}_{\mathrm{inv}}\,\mathrm{d}\vec{A}=\iint\limits_{\partial V}\vec{F}_{\mathrm{visc}}\,\mathrm{d}\vec{A}+\iiint\limits_{V}\vec{S}\,\mathrm{d}V\,. \tag{4.1}$$

Here, $\vec{U}$ is the vector of conservative variables

$$\vec{U}=\begin{pmatrix}\rho_s\\ \rho\vec{u}^{\mathrm{T}}\\ \rho E\end{pmatrix}. \tag{4.2}$$

The inviscid Euler fluxes can be written

$$\vec{F}_{\text{inv}} = \begin{pmatrix} \rho_s \vec{u}^{\,\mathrm{T}} \\ \rho \vec{u}\vec{u}^{\,\mathrm{T}} \\ \rho H \vec{u} \end{pmatrix} + \begin{pmatrix} 0 \\ p\overline{\overline{I}} \\ 0 \end{pmatrix}, \tag{4.3}$$

accompanied by the viscous Navier-Stokes fluxes

$$\vec{F}_{\text{visc}} = \begin{pmatrix} \rho D \nabla^{\mathrm{T}} \frac{\rho_s}{\rho} \\ \overline{\overline{P}} \\ k\nabla^{\mathrm{T}} T + \rho D \sum_s h_s \nabla^{\mathrm{T}} \frac{\rho_s}{\rho} + (\overline{\overline{P}}\vec{u})^{\mathrm{T}} \end{pmatrix}. \tag{4.4}$$

The viscous stress tensor $\overline{\overline{P}}$ is modeled according to the Stokes hypothesis,

$$\overline{\overline{P}} = \mu\left(\nabla\vec{u}^{\,\mathrm{T}} + (\nabla\vec{u}^{\,\mathrm{T}})^{\mathrm{T}}\right) - \frac{2}{3}\mu(\nabla^{\mathrm{T}}\vec{u})\overline{\overline{I}}. \tag{4.5}$$

The Dufour effect (thermal diffusion due to concentration gradient) is thus taken into account. The source terms $\vec{S}$ include the chemical contribution to the species transport equations ω_s as well as a volumetric heat source $\dot{q}$,

$$\vec{S} = \begin{pmatrix} \omega_s \\ \vec{0} \\ \dot{q} \end{pmatrix}. \tag{4.6}$$

The system is closed with the ideal gas equation

$$p = \sum_s \rho_s R_s T. \tag{4.7}$$

4.2.2 Transport Coefficients

Blottner et al. curve fits [21] are used to calculate species laminar viscosity,

$$\mu_s = 1\left(\frac{\mathrm{Ns}}{\mathrm{m}^2}\right)\exp(C_s)T^{(A_s\ln(T)+B_s)}. \tag{4.8}$$

The individual values are then combined using Wilke's mixing rule [169]

$$\mu = \sum_s \frac{n_s\mu_s}{\sum_m n_s \phi_{s,m}} \tag{4.9}$$

with

$$\phi = \frac{1}{\sqrt{8}}\left(1+\frac{M_s}{M_m}\right)^{-1/2}\left[1+\left(\frac{\mu_s}{\mu_m}\right)^{1/2}\left(\frac{M_m}{M_s}\right)^{1/4}\right]^2. \tag{4.10}$$

Thermal conductivity is computed using a modification of the Eucken correction by Hirschfelder et al. [64]

$$k = \mu_s\left(\frac{5}{2}(c_v)_s^{\mathrm{t}} + \frac{(c_v)_s^{\mathrm{rot}} + (c_v)_s^{\mathrm{vib}} + (c_v)_s^{\mathrm{e}}}{\mathrm{Sc}}\right). \tag{4.11}$$

The mixture heat conductivity is then determined following Zipperer and Herning [177],

$$k = \sum_s \frac{n_s k_s}{\sum_m n_s\sqrt{M_m/M_s}}. \tag{4.12}$$

The diffusion fluxes are calculated from viscosity and a constant Schmidt number using Fick's law. Then, the diffusion coefficient D reads

$$D = \frac{\mu}{\rho}\frac{1}{\mathrm{Sc}} \tag{4.13}$$

4.2.3 Chemical Reactions

Now, values for the chemical source term need to be computed. Generally, a chemical reaction can be expressed as

$$\sum_s \alpha_s^r \mathrm{X}_s \xrightarrow{k_r^f;k_r^b} \sum_s \beta_s^r \mathrm{X}_s. \tag{4.14}$$

Here, X_s represents the species symbol, α_s^r and β_s^r are the stoichiometric coefficients (often called ν_s in the literature), and k_r^f and k_r^b are the forward and backward reaction rate, respectively, Applying the law of mass action over all equations, the chemical source term ω_s, representing the temporal change of the partial density of species s can be expressed as

$$\omega_s = M_s\sum_r(\beta_s^r - \alpha_s^r)\left[k_r^f\prod_s(x_s)^{\alpha_s^r} - k_r^b\prod_s(x_s)^{\beta_s^r}\right], \tag{4.15}$$

with $x_s = \rho_s / M_s$, the concentration. The forward reaction rate is evaluated using the modified Arrhenius law

$$k_r^f = a_r^f \left(\frac{T}{1\mathrm{K}} \right)^{b_r^f} \exp\left(-\frac{c_r^f}{T} \right). \tag{4.16}$$

The backward reaction rate can be expressed in terms of the equilibrium constant

$$k_r^b = \frac{k_r^f}{K_r^{eq}}, \tag{4.17}$$

which in turn is calculated from partition functions within TAU,

$$K_r^{eq} = \prod \left(\frac{Q_s}{V N_A} \right)^{\beta_s^r - \alpha_s^r}. \tag{4.18}$$

Hannemann [58] gives a thorough overview of the use of partition functions in the TAU code.

An important metric in combustion is the occurrence of the OH^* radical. Typically, its spontaneous emissions are associated with the position of heat release in the flame. As an intermediate product, OH^* is used to mark the spatial distribution of the flame. Fiala and Sattelmeyer [46] point out that there are two ways the radical is produced, chemically as a dedicated reaction product, and thermally as an excitation of OH at ground state. According to them, chemical excitation is negligible in the conditions of a high pressure rocket combustion chamber. Then, OH^* concentration can be estimated from the OH and the temperature distribution,

$$\frac{x_{OH^*}}{x_{OH}} = K_p(T) = \exp\left(\frac{-\Delta g_{mf}^0}{RT} \right). \tag{4.19}$$

Thus, evaluation of reaction mechanisms using finite rate chemistry and an additional species transport equation are not necessary: evaluation of computations of rocket engines reduces to a mere postprocessing step.

4.2.4 Finite Volume Method

The system of equations is solved using a Godunov type finite volume method. An illustrative one-dimensional scheme with first order forward Euler time integration is discussed. Starting from the Navier-Stokes equations Eq. (4.1),

neglecting viscous fluxes leads to

$$\iiint_{\mathrm{V}} \frac{\partial \vec{U}}{\partial t} \mathrm{d}V + \iint_{\partial V} \vec{F} \mathrm{d}\vec{A} = \iiint_{V} \vec{S} \mathrm{d}V. \tag{4.20}$$

The integral conservation law (4.20) can be interpreted as follows. The temporal change of $\vec{U}$ in the volume V equals the flux $\vec{F}$ over the boundaries $\vec{A}$ of V and change due to local sources $\vec{S}$. Applying Gauss' divergence theorem, the flux integral can be converted from a surface to a volume integral

$$\iiint_{\mathrm{V}} \frac{\partial \vec{U}}{\partial t} \mathrm{d}V + \iiint_{\partial V} \frac{\partial \vec{F}}{\partial x} \mathrm{d}V = \iiint_{V} \vec{S} \mathrm{d}V. \tag{4.21}$$

The basic finite volume prerequisite is that the variables are constant within the regarded constant volume (e.g. a grid cell). Then,

$$V \frac{\partial}{\partial t} \vec{U} + V \frac{\partial}{\partial x} \vec{F} = \vec{S} V. \tag{4.22}$$

Finally, the computational domain is discretized spatially and temporally, i.e. the differentials are replaced by differences:

$$V \frac{\vec{U}^{n+1} - \vec{U}^{n}}{\Delta t} + V \frac{\vec{F}_{\mathrm{out}} - \vec{F}_{\mathrm{in}}}{\Delta x} = \vec{S} V. \tag{4.23}$$

Solving for the state at time step $n+1$:

$$\vec{U}^{n+1} = \vec{U}^{n} + \frac{\Delta t}{\Delta x} \left[\vec{F}_{\mathrm{in}} - \vec{F}_{\mathrm{out}} \right] + \Delta t \vec{S} \tag{4.24}$$

Hence, in order to update the domain from $\vec{U}^{n}$ to $\vec{U}^{n+1}$, the fluxes $\vec{F}$ and the sources $\vec{S}$ need to be evaluated.

The fluxes are determined using the classical Godunov approach. At each cell interface, the states of the left cell U^{-} and the right cell $\vec{U}^{+}$ encounter each other in the form of a discontinuous jump at the interface. Godunov realized that this is the well known Riemann problem, which can be solved exactly for the inviscid Euler equations. However, this solution requires iterative algorithms which are numerically expensive. Today, approximative Riemann solvers, such as Liou's AUSM family [95] are used as they provide sufficient accuracy at a fraction of the computational cost. For the low Mach numbers encountered in combustion chambers dedicated schemes are avail-

able, such as Liou's AUSM+up [96] or Rossow's MAPS+ [138].

The spatial accuracy can be further increased using a second order MUSCL reconstruction (van Leer [162]) of the states at the interface. This effectively replaces the constant values with linear distributions, taking into account more cells. Temporal accuracy can be improved by e.g. replacing the first order time integration shown here by a more sophisticated Runge-Kutta scheme. The main steps of a FV method can be summarized as

1. Conservative variable values are distributed constant in each cell of the computational domain.
2. A reconstruction algorithm determines the left and right state at each cell interface.
3. The flux across each interface is evaluated by solving the Riemann problem for the reconstructed states.
4. Source terms are integrated.
5. Fluxes and sources are added as residuals.
6. The computational domain is updated to the new time step.

4.3 Thermodynamics Structure

The main task for the thermodynamics model is to answer the question *given two state variables, what is the value of the remaining variables?* The given variables depend on the problem within the solver[1]:

$f(\rho,e) \rightarrow p, (T,a,\mu,k,c_v)$
$f(\rho,T) \rightarrow e$
$f(\rho,p) \rightarrow h, (a,s)$
$f(h,s) \rightarrow \rho,p$

The structure then pinpoints in which way and in which order the unknowns are determined from these given variables. Clearly, it has to fulfill several conditions: The solutions to the problems need to be unique, consistent, numerically efficient. The functions $f(\rho,e)$, $f(\rho,T)$, and $f(\rho,p)$ are used during transformation between conservative and primitive variables, $f(\rho,T)$ is furthermore used at isothermal wall boundary conditions. The $f(h,s)$ problem is solely used in the reservoir inflow boundary condition.

[1] TAU nomenclature designates a function $f(\rho,\bullet)$ as '*rho-•-problem*' - also for mixtures. Thus, for consistency, ρ in this context denotes the vector of all partial densities.

4.4 The TAU Code for Combustion Applications

In the present work, TAU's finite rate chemistry model is used. The mechanism is Jachimowski's [69] 8 species, 17 reaction model, as reported by Gerlinger et al. [49]. Regarded species are H_2, O_2, OH, H_2O, H_2O_2, O, H, HO_2. The elementary reactions and associated rate constants for Eq. (4.16) in Ch. 4.2.3 are tabulated in App. 4.

4.4.1 Validation of TAU for Combustion of Ideal Gases

The finite rate model and the mechanism have been validated systematically and extensively by Karl [76]. Fundamental 0D computations successfully reproduce ignition delay times and explosion limits of hydrogen-oxygen combustion. The very challenging[2] problem of lift-off height of a supersonic combustion flame is also matched. Scramjet engine pressure distribution (Karl [76]) as well as OH* distributions and transient phenomena have successfully been computed using TAU (Laurence et al. [88]) and agree very well with both experiments and more elaborate LES simulations (Chapuis et al. [32]).

TAU has successfully been applied to reactive coaxial gas-gas injection in the PennState burner test case used in the RCM modeling workshop 2006 as RCM1 [180]. It could be shown (Ivancic et al. [68]) that wall heat flux distributions obtained with TAU agree well with experiments. Furthermore, results are well in the range of results obtained with other codes (Ivancic et al. [68]), including more elaborate models, such as compiled by Tucker et al. [160].

4.4.2 Turbulent Combustion

A note is necessary on turbulence-combustion-interaction, a topic well discussed in the literature (e.g. Peters [127], Poinsot and Veynante [129], Kuo and Acharya [82]). In a RANS context, the averaged flow field is computed, the actual physical instantaneous flow values oscillate around this mean

[2] Convective time scales in a scramjet engine at supersonic velocities are much smaller than in a rocket combustion chamber at M< 0.3.

value. This is also true for the temperature which determines the reaction rate. Consider again the Arrhenius equation

$$k_r^f = a_r^f \left(\frac{T}{1\mathrm{K}} \right)^{b_r^f} \exp\left(-\frac{c_r^f}{T} \right) \tag{4.16}$$

which shows the nonlinear dependence of the reaction rate on the temperature T. This means that mathematically, evaluating Eq. (4.16) with the averaged temperature will not yield the corresponding averaged reaction rate.

The question from an engineering point of view is then: how large is the deviation? Karl [76] carried out comprehensive studies on the influence of turbulence model, turbulent Prandtl and Schmidt numbers in the aforementioned studies of scramjet flow. He found that any of these parameters has a higher impact on the flow than the difference between a laminar and a PDF based turbulent combustion model. Lempke et al. [92] compared laminar and turbulent combustion in unsteady RANS simulations of the PennState gas-gas burner. Figure 4.1 shows temperature isocontours for both cases. They are practically indistinguishable.

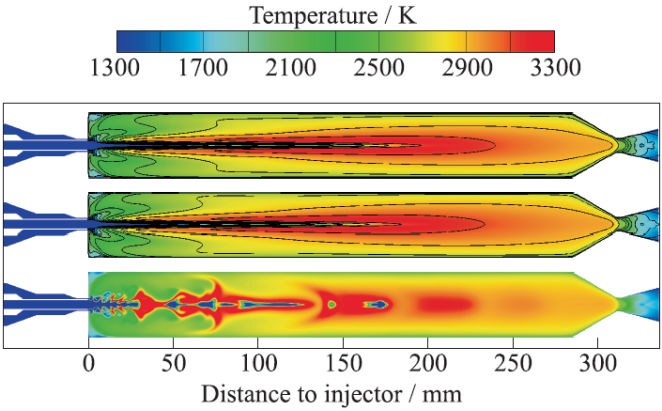

Figure 4.1: Averaged temperature contours estimated using laminar chemistry (top), assumed PDF approach (middle); temperature snapshot using PDF (bottom). From Lempke et al. [92]

It is hence concluded that, while envisioned for future work, treatment of turbulent combustion will be neglected for the present thesis.

5 Real Gas Extension of TAU

5.1 Introduction

In this chapter, the development of a new real gas model will be described which has been implemented into the DLR TAU code[1]. The purpose of this model is to correctly model real gas behavior and to treat mixtures of real and ideal gases. The application initially envisioned is combustion in rocket combustion chambers.

Chapters 1.2 and 2.3.1 discussed the physical processes involved in high pressure injection, as present in rocket combustion chambers during steady operation. This can be summarized with regards to a numerical model:

- Droplets do not exist at all or are consumed immediately. The movement of droplets in the flow can be neglected.
- The injected oxidizer can be regarded as a continuous stream rather than a cloud of dispersed droplets. It is thus most appropriately treated as an Eulerian continuum.
- Oxidizer fluid states might range from sub- to supercritical pressures for different engines. An appropriate treatment of real gas thermodynamics of oxygen is necessary.
- No mixture of oxygen and hydrogen is formed in the chamber before combustion. Instead, a diffusion flame is found which is anchored at the LOX post tip. Hydrogen and oxygen stream are effectively isolated from each other by the flame.
- Mixing occurs in the hot reaction zone where fluids behave as ideal gases.

The baseline real gas model was introduced into the TAU code by Calvo [28], which used a precomputed library to store fluid properties. Intended to be used for the computation of hydrogen flow in cooling channels, the implementation was limited to strictly supercritical states of a pure fluid in a

[1] This has first been discussed in [16].

Function	Knowns	Iteration
$p,T = f(\rho,e)$	-	2D-Newton
$e = f(\rho,T)$	T	1D-Newton
$h = f(\rho,p)$	p	1D-Newton

Table 5.1: Numerics for baseline p,T library (Calvo [29], Calvo and Hannemann [28]).

sufficient distance to the critical point. Furthermore, the whole state space was sufficiently limited to be completely included in the library. Neither did the model allow for mixtures, nor for a transition of the real gas to an ideal gas. Thus, the thermodynamic structure needed to deal with iterations on the library alone. It could also be assumed that properties change sufficiently smooth to employ multidimensional iteration schemes such as Newton's method. This lead to a design based on a library linear in p and T, chosen because of its direct correspondence to experimental boundary conditions. The thermodynamic main functions $f(\rho,e)$, $f(\rho,T)$, and $f(\rho,p)$, as introduced in Ch. 4.3, needed to be expressed in terms of iterations in a p,T library, Tab. 5.1.

For the desired model here, two demands need to be satisfied which cannot be met with the existing baseline model. First, the real gas component needs to be treated over the whole state space, including ideal gas and supercritical states, critical point, liquid, and the coexistence regime. Second, the real gas component is part of a mixture with ideal gases. Thus, a completely new structure has to be designed from ground up.

There are a number of CFD codes for similar applications, Tab. 5.2 compiles an overview. The table contains work of the pioneering groups, e.g. Bellan and Okong'o [18, 121, 122, 123], Oefelein and Yang [116, 117, 119], Yang et al. [173, 178, 179], and recent work, such as the extension of Stanford's CharlesX code by Hickey et al. [63]. On a first glance, the diversity seems overwhelming. The fidelity of the methods ranges from DNS, over LES to URANS and RANS. Chemistry is treated using everything from finite rate models, flamelet, eddy dissipation, to equilibrium models. However, the apparent variety is misleading. The successful codes are used as stencils, only few try something original, such as Barata et al. [17] with the mixture fraction approach in TEACH, or Pourouchottamane et al. [133] by using an interfacial area density concept in their MSD-DLS code. Really, only few thermodynamics models can be distinguished. Especially the most recent codes follow the identical, proven recipe (Hickey et al. [63], Masquelet et

al. [99], Schmitt et al. [143, 144, 145], Niedermayer et al. [115], Poschner and Pfitzner [131, 132]): They typically employ a PR or SRK EOS, which is evaluated during runtime using van der Waals mixture rules. Costly EOS, such as BWR, remain restricted to groups with massive computational infrastructure, such as Oefelein at Sandia.

However, in this thesis, the initial path of using a high quality equation of state in a precomputed library was to be followed further. The literature does not give a solution on how a dedicated species library, here of oxygen, can be successfully incorporated into a mixture model. Hosangadi et al. [65] explicitly stated that they did *not* use a library because this would prevent him from extending his code to mixtures in the future. Only for pressure-based solvers, such as FDNS-RFV of Farmer et al. [45] and CFX used by Poschner and Pfitzner [131] apply a so-called additive volumes model, where species contributions are summed up instead of using a single EOS. However, Poschner and Pfitzner are not satisfied with this approach: They commented on the the model probably not conserving momentum in a pressure based framework.

Thus for the present thesis, a new real gas model for a compressible solver is developed. Its components will be discussed in the following top-down order:

Arbitrary Phase Euler-Euler Model The code needs to accommodate the additional real gas phase. In order to take full advantage of the library, this real gas phase may represent an additional liquid phase, a liquid-vapor mixture, a supercritical fluid, or an ideal gas.

Thermodynamics Architecture The logical layout of the thermodynamic functions needs to be designed, i.e. which variables are computed from which in which order. This design needs to be numerically robust and efficient.

Multi-Fluid Mixing Model This new mixing model allows to use different EOS simultaneously in a compressible code. It requires a logic to decide which EOS to solve and how to blend to the baseline ideal gas treatment. The numerical design of the iterative functions with an emphasis on robustness needs to be carried out. Finally, the actual mixing model, determining mixture states from individual species states and vice versa, needs to be developed.

Real Gas Library Real gas properties need to be stored in an appropriate manner to allow for a resolution of the complete fluid state space. This has to be consistent with the thermodynamics architecture.

Source	Name	Type	Dims	Turbulence	Spray	EOS	Mixing	Combustion	Dampening	Pressure
[104, 23]	'CFD-ACE'	incomp	axi	k-ε	SEE	n/a	x	x	n/a	BC
[119]	Oefelein	compr	2D	LES	SEE, SEL	BWR/SRK	ECS	FR9S24R	n/a	BC
[116]	Oefelein	compr	axi	DNS/LES	SEE	PR	ECS	FR nS	n/a	nozzle
[117]	Oefelein	compr	axi	DNS/LES	SEE	PR	ECS	FR9S19R	n/a	n/a
[173]	Yang	n/a	2D	LES	SEE, SEL	BWR/SRK	ECS	x	n/a	BC
[178]	Zong	FV compr	axi	LES	SEE	SRK, BWR (t)	ECS	x	AD/TVD	BC
[179]	Zong	FV compr	axi	LES	SEE	SRK, BWR (t)	ECS	x	AD/TVD	BC
[45, 35]	'FDNS-RFV'	FD incomp	axi	k-ε	SEE/SEL	HBMS	additive volume	FR6S10R	n/a	BC
[121, 122, 123]	Bellan	pressure	3D	DNS	SEE	mPR	vdW	x	n/a	BC
[133]	'MSD+DLS'	struct FV	axi	k-ε	SEL/IATE	iG	iG	EQU,PDF	n/a	nozzle
[17]	'TEACH'	incomp	axi	k-ε	SEE	iG/Z eq	iG	x	UR	n/a
[168]	'ROCFLAM'	FV compr	axi	k-ε	SEL	iG	iG	FR	n/a	nozzle
[52]	'CryoROC'	FV compr	axi	k-ε	SEL	iG	iG	FR5S1R ED	n/a	nozzle
[79]	'Rocflam II'	FV compr	axi	k-ε	SEL*	iG	iG	EQU,PDF, FR ED	n/a	nozzle
[37, 38]	Cutrone	compr	axi	k-ε	SEE	PR. iG	vdW	Flamelet, PV	n/a	BC
[131, 132, 71]	'CFX'	pressure	axi	k-ε	SEE	RK, PR	vdW, ECS	ED1S, Flamelet	RO	BC
[65]	'CRUNCH'	FV compr	3D	RANS/LES	SEE	SRK, HBMS	x	x	n/a	BC
[144, 145, 143]	'AVBP'	compr	3D	LES	SEE	PR	vdW	FR4S2R	AD	BC
[99]	Masquelet	FV compr	axi	LES	SEE	PR	vdW	EBU, EQU, FR2S	AD	nozzle
[77]	Kim	FV incomp	axis	k-ε	SEE	mSRK. PR	vdW	Flamelet	n/a	BC
[63]	'CharlesX'	FV compr	2D	LES	SEE	PR	vdW	x	RO	BC
[112, 115]	'INCA'	FV compr	3D	LES	SEE	PR	vdW	x	n/a	BC

Table 5.2: Overview of CFD codes for real gas injection. Abbreviations: n/a: not given, x: not used, incomp: incompressible, compr: compressible, FV: finite volume,, pressure: pressure based, FD: finite difference, struct: structured, axi: 2D axisymmetric, 2D: 2D planar, k-ε: RANS, SEL*: statistical Eulerian-Lagrangian where particles are converted to continuum immediately after injection, BWR (t): BWR EOS used for transport coefficients, HBMS: Hirschfelder-Buehler-McGee-Sutton EOS, mPR: modified PR EOS, Z eq: mixture fraction transport equation, mSRK: modified SRK EOS, iG: ideal gas EOS or mixing rules,FRnSmR: finite rate chemistry with n species and m reactions, EQU: equilibrium, PDF: flame turbulence interaction based on probability density function, ED: eddy dissipation, PV: progress variable, ED1S: eddy dissipation one species, EBU: eddy break-up, AD: artificial dissipation, TVD: total variation diminishing, RO: reduced order, UR: underrelaxation of momentum equations, BC: pressure set as boundary condition, nozzle: pressure is part of solution and determined by flow through defined nozzle.

The scope of a thesis is necessarily limited. Topics which will not be addressed are

Flux solvers The standard approximate Riemann flux solvers are based on the ideal gas equation. Regarding a real gas instead, the solution to the Riemann problem changes (Toro [158]). However, for the very low Mach numbers encountered in coaxial rocket injectors, these effects will be neglected.

Chemistry Reactions are computed using finite rate models based on an Arrhenius ansatz. Possible alterations include turbulence-flame interaction models, special high pressure reaction mechanisms, or adaptation of the law of mass action for real gases. With the assumption that mixing and reaction only occurs in the hot flame, real gas effects are assumed to be negligible.

Turbulence Established turbulence models typically stem from the assumption of an incompressible fluid. Thus, the extreme variations of specific volume of a vaporizing liquid or a supercritical fluid clearly does not fulfill the assumptions.

Adaptation of physical models The Soret effect (molecular diffusion due to temperature gradient) is not taken into account. This is found valid for real gas reacting cases (Oefelein [117]) but to a lesser extent for inert mixing cases (Bellan [19]).

5.2 Arbitrary Phase Euler-Euler Model

A multiphase description of a fluid is sought which needs to be valid for the intended application of injection of cryogenic oxidizer into a gaseous environment. It has been argued and shown that the Eulerian approach is not only applicable to the task of injection modeling, but that it is, in fact, in many ways superior to a Lagrangian modeling of the injected oxygen for the cases regarded in this thesis.

First of all, it has been shown that physically, the oxidizer is injected as a compact, continuous stream and not as a disperse cloud of individual droplets. In fact, experiments show that droplets do not play a significant role in liquid rocket engine injection.

Eulerian modeling is a more natural way to treat injection processes. Inflow boundary conditions correspond to data directly accessible in the experiment, such as temperature, pressure, mass flow. Using a fluid state (by knowing pressure and temperature) and an injection velocity (from mass flux, density, and injector cross section) directly produces qualitatively reasonable results, without further tuning the model to the specifics of the experiment. The approach has successfully been used for sub- and supercritical injection by several researchers, e.g. Cheng and Farmer [35] or Jay et al. [72]. In this way, estimations even for unknown facilities are possible. This stands in contrast to Lagrangian methods, which require an assessment of a priori unknown (and unphysical) droplet size and velocity distributions if the model is to perform satisfactorily.

An Eulerian method allows to capture the interaction between fluid and injector. This works in both directions: e.g. wall heat transfer inside the injector allows to capture preheating of the fluid. In the other direction, upstream influence within the injector can be taken into account by resolving the injector in the desired region, allowing to capture coupling important for combustion instability[2].

Methods of this nature are called *Statistical Eulerian Eulerian* (SEE), as both injected and surrounding fluids are described as Eulerian continua, averaged over time (much like RANS or URANS). This Statistical-Eulerian-Eulerian model must not be confused with other multiphase models such as

[2] While using a Dirichlet inflow boundary condition mathematically violates the characteristic theory of boundary conditions, the effect was found to be small. In a Lagrangian method, the droplets are introduced *inside* the chamber, thus a physical coupling with the injector is inherently impossible.

Volume of Fluid (VOF) or levelset methods which strive to resolve the phase surface.

The required model sophistication needs to be addressed. Dependent on the degree of interaction between the phases, three main types can be distinguished (Wörner [171]):

Homogeneous In the homogeneous multiphase model, a mechanical and thermodynamic equilibrium is assumed in each cell. This means that both phases have identical velocity, temperature, and pressure. The flow field of the carrier phase is computed from the governing equations (e.g. Navier-Stokes). The homogeneous model has two applications: first, it is valid for cases in which one phase is disperse and follows the carrier phase without slip, e.g. aerosols. Second, it can be applied when the two phases are clearly separated, e.g. at open surfaces. It can then be assumed that, while two phases are treated in the simulation, in a given computational cell there is either one *or* the other phase present.

Drift Flux The drift flux model allows for some relative velocity between the phases if the relation is known. E.g., the terminal velocity of a droplet falling in a quiescent atmosphere can be calculated from the equilibrium between its aerodynamic drag and its weight. The method computes the velocity field of the mixture, the respective phase velocities are then calculated from the relation. Its application is limited to cases in which the model of relative motion is applicable.

Two Fluid The two fluid model treats two independent phases in a computational cell. The complete set of governing equations is duplicated, as two velocity, temperature, and pressure fields are solved. Coupling between the phases is carried out via source terms, i.e. drag from one phase moving relative to the other in an assumed spherical shape, acts as force source terms in the momentum equations of both phases. The method is the most general but also most complicated model. In addition, it constitutes a mathematically ill-posed problem (Ishii and Hibiki [66]), requiring additional damping terms which have mathematical rather than physical motivation.

In transcritical injection, described as resembling turbulent mixing in the literature, no relative velocity between the phases exists - if one can actually speak of phases. A homogeneous SEE model is hence deemed appropriate. The thermal and mechanical equilibrium assumption can be translated as same pressure and same temperature in a cell for all components.

5.3 Thermodynamics Architecture

The initial question to be answered is the choice of spanning variables for the library, as this determines its structure. The tasks of the thermodynamics functions have been introduced in Ch. 4.3. Three functions are essential to the working of TAU, when the reservoir boundary condition is not used: $f(\rho, e)$, $f(\rho, T)$, $f(\rho, p)$. As in all three the density ρ is assumed known, it is beneficial to use it as one of the library keys. In this way, there is always one parameter known when solving the problems, extending the choice of available iteration schemes to more stable algorithms. This is already an advantage over Calvo's original implementation [28], summarized in Tab. 5.1. As second key variable, the temperature is chosen, because this is one of the primitive variables measured in the experiments. Choosing density ρ and temperature T will resolve the coexistence regime. For consistency it is important to perform the iteration on a single 'master' library and not have a dedicated library for each of the thermodynamic functions.

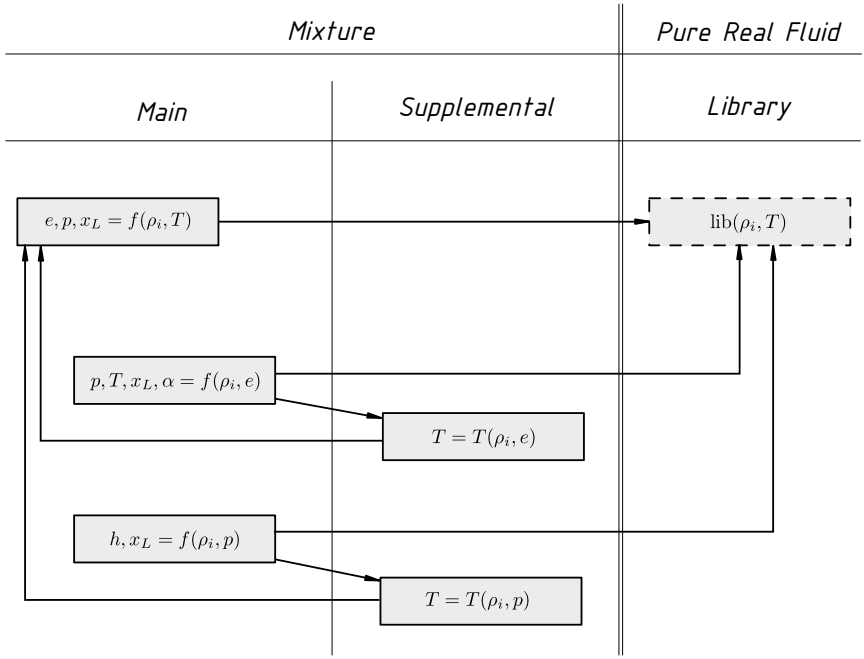

Figure 5.1: Thermodynamic structure of TAU real gas extension.

Function	Knowns	Iteration	Subcalls
$e = f(\rho, T)$	ρ_s, T	-	$(\rho_s, T)_{\text{lib}}$
$p = f(\rho, e)$	ρ_s	-	$T(\rho, e)$, $(\rho_s, T)_{\text{lib}}$
$h = f(\rho, p)$	ρ_s	-	$T(\rho, p)$,$(\rho_s, T)_{\text{lib}}$
$T = f(\rho, e)$	ρ_s	Regula-falsi	(ρ, T)
$T = f(\rho, p)$	ρ_s	Regula-falsi	(ρ, T)
$(\rho_s, T)_{\text{lib}}$	ρ_s, T	-	-

Table 5.3: Numerics for ρ, T based Library

The resulting structure is illustrated in Fig. 5.1. It can be interpreted in several ways. First, from a program point of view, there are the main functions $p, T = f(\rho, e)$, $e, p = f(\rho, T)$, $h = f(\rho, p)$. These can be called from anywhere in the solver, keeping the ideal gas TAU interface design. Underneath, the problems are subdivided further. The supplemental functions $T = f(\rho, e)$ and $T = f(\rho, p)$ are called only from $f(\rho, e)$ and $f(\rho, p)$, respectively. The supplemental functions are the only iterative functions and operate by calling $f(\rho, T)$ in turn. Thus, $f(\rho, T)$, not needing a supplemental function itself, is the head function. Finally, once T and ρ are known in every function, the real gas values can be drawn from the library using $\text{lib}(\rho_s, T)$. It is important in terms of numerical efficiency that the head function, which is called in every main function call, works without using iterations. This is summarized in Tab. 5.3.

From a physical point of view, main and supplemental functions operate on the mixture level, i.e. mixture rules are implemented here. The library function deals instead with a single pure real gas.

Treatment of an ideal gas mixture, a pure ideal gas, and a pure real gas are contained as special cases. The new model thus encompasses the ideal gas TAU model and Calvo's pure supercritical fluid model. Furthermore, the structure is generally designed to be capable of accommodating a mixture involving several real gases, although this is not the topic of this work and neither pursued nor tested further.

5.4 Multi-Fluid Mixing

Single fluid mixing (SFM) models have been discussed in Ch. 3.1.4. They remain state of the art, see Tab. 5.2. A SFM model determines the properties of a virtual pure fluid which is assumed to exhibit the mixture behavior. Its properties are determined by evaluating the fluid coefficients a, b and the specific volume v as a weighting factor in a single EOS. Fig. 5.2(a) illustrates this.

Using a pure fluid real gas library, determining the mixture properties has to be done differently. A dedicated EOS needs to be evaluated for each species, the mixture properties are then computed afterwards, see Fig. 5.2(b). This is called two-fluid mixing by Pfennig [128]. As it will be applied here for a s-species mixture, the mixing model will be referred to as *Multi-Fluid-Mixing* (MFM).

In summary, the difference is illustrated in Fig. 5.2(c).

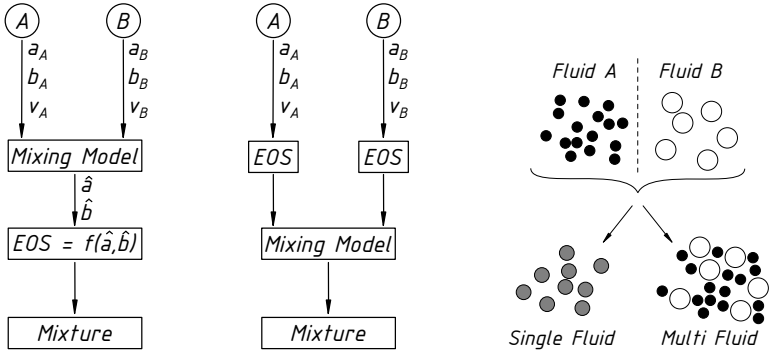

(a) SFM model flow chart.

(b) MFM model flow chart.

(c) Phenomenology: SFM virtual pure fluid vs. MFM heterogeneous mixture.

Figure 5.2: Single fluid mixing (SFM) vs. multi fluid mixing (MFM).

5.4.1 Mixture Rules for Coaxial Injection

A first set of mixture rules is devised for the targeted simulation of reactive coaxial injection processes. These kinds of flows were discussed in Ch. 2.3.5.

It could be concluded that in cryogenic diffusion flames, non-negligible mixing occurs only where fluids behave as ideal gases. Then, simple ideal gas mixing rules may be applied for cryogenic coaxial injection.

It is necessary to define mixture rules in two directions:

1. How do individual species thermodynamic states combine to the mixture state?

2. How can the individual species partial properties be determined from the mixture value?

The mixture density is the sum of the partial densities. As an equation is solved for each partial density, they are known at any point in the flow field and need not be determined[3],

$$\rho = \sum_s \rho_s. \tag{5.1}$$

Having chosen a homogeneous Euler-Euler model in thermal equilibrium, the species temperatures and the mixture temperature are identical,

$$T = T_s. \tag{5.2}$$

The mixture inner energy is known at any point in the flow field, either from solving the energy equation, or from evaluating $f(\rho, T)$ or $f(\rho, p)$ at a boundary. It equals the sums of the partial energies. Assuming ideal mixing, no contribution of mixing to the energy state is made,

$$e = \frac{\sum_s \rho_s e_s}{\sum_s \rho_s}. \tag{5.3}$$

Calculating the species partial inner energies thus requires an iterative approach. In an ideal gas, the inner energy is only a function of the temperature. In a real gas, density also has an influence, the partial energies need to be found as a function of two variables. By design, the library takes advantage of the partial densities always known. Thus, the iteration can be reduced to the iteration of a single variable. The partial inner energies $e_s(T)$ can be determined by finding the temperature T, for which the sum of the partial energies equals the mixture inner energy. As $e_s(T)$ is strictly

[3] This is not true for the reservoir inflow boundary condition which solves for the density when enthalpy and entropy are given. As stated earlier, this particular boundary condition is not regarded in this thesis.

monotonous, this is mathematically unique,

$$e_s = \left\{ e_s(T) \left| \sum_s \rho_s e_s(T, \rho_s) = e \sum_s \rho_s \right. \right\}. \tag{5.4}$$

The pressure is determined as the sum of the species partial pressures.

$$p = \sum_s p_s. \tag{5.5}$$

This is effectively Dalton's law for the case of ideal gas mixing and Raoult's law of additive vapor pressures for the case of liquid mixing. The partial pressures are calculated from the mole fraction of each component,

$$p_s = \frac{\rho_s R_s}{\sum_s \rho_s R_s}. \tag{5.6}$$

As a first approximation, the mixture speed of sound (SOS) is calculated as the mass weighted average of the library stored real gas SOS and the ideal gas SOS:

$$a_{\mathrm{iG}} = \sqrt{\frac{c_{p,\mathrm{iG}}}{c_{v,\mathrm{iG}}} R_{\mathrm{iG}} T}, \tag{5.7}$$

with $\phi_{\mathrm{iG}} \in \{c_{p,\mathrm{iG}}, c_{v,\mathrm{iG}}, R_{\mathrm{iG}}\}$ summed over the ideal gas species s_{iG}

$$\phi_{\mathrm{iG}} = \frac{\sum_{s_{\mathrm{iG}}} \rho_{s_{\mathrm{iG}}} \phi_{s_{\mathrm{iG}}}}{\sum_{s_{\mathrm{iG}}} \rho_{s_{\mathrm{iG}}}}. \tag{5.8}$$

Other auxiliary variables α need only be determined in one direction, i.e. from the species to the mixture.

$$\alpha = \frac{\sum_s \rho_s \alpha_s}{\sum_s \rho_s}, \qquad \alpha \in \{s, c_p, c_v, \}. \tag{5.9}$$

Transport coefficients are calculated using TAU's ideal gas mixing models, as discussed in Ch. 4.

5.4.2 Main Functions

Figure 5.3 shows the logical structure of $f(\rho, e)$ in the form of a Nassi-Shneiderman diagram[4]. As discussed before, $f(\rho, p)$ and $f(\rho, e)$ need to call a subroutine to determine the temperature. Apart from this, the structure of all main functions is similar, looping over all states and species i. Crucial to the model is the splitting depending on whether the regarded species needs to be treated as a real or as the baseline ideal gas. This is decided based on limiting values which need to be set by the user. The ideal gas treatment is used when

- no library exists for the specific species,
- the species partial density ρ_i is smaller than the limit $\rho_{\text{min}}^{\text{lib}}$,
- the temperature T exceeds the limit $T_{\text{max}}^{\text{lib}}$,
- only $f(\rho, p)$: the partial pressure p_i is smaller than the limit $p_{\text{min}}^{\text{lib}}$.

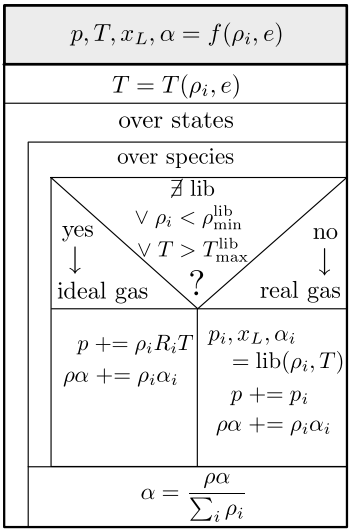

Figure 5.3: Main function $f(\rho, e)$.

[4]Nassi-Shneiderman diagrams of all main functions are shown in Fig. 1 in Appendix 3.

5.4.3 Supplemental Functions

The main functions $f(\rho, e)$ and $f(\rho, p)$ require an additional determination of the temperature. This is done in the supplemental functions. Looping over all states, the highest and lowest temperatures expected in the computation are set by the user as limits of the algorithm. The iteration stops when either a maximum iteration count $c_{\max}$ is exceeded or the target values match the iterated values sufficiently close. The logical structure of the supplemental functions is again shown in the form of Nassi-Shneiderman diagrams in Fig. 2 of Appendix 3.

In the TAU real gas extension, the supplemental functions are the only iterative thermodynamics functions. A method is sought to solve $T = f(\rho, e)$ and $T = f(\rho, p)$, which primarily needs to be robust and desirably efficient. Three root finding methods are discussed in detail, despite being textbook knowledge (e.g. Dahmen and Reusken [39]) because of the utter significance to the model. The algorithms are introduced in a general form, where for a known f_{it} an x_{it} is sought for which $f(x_{\text{it}}) = f_{\text{it}}$. Afterwards, they are analyzed for the actual problem of finding the temperature which corresponds to a given inner energy, $e_{\text{it}} = e(T_{\text{it}})$. The index k denotes the iterative step.

Newton's Method

Newton's method of finding the root of a function f has a straightforward geometric interpretation. Evaluate the function f and its derivative $\mathrm{d}f/\mathrm{d}x = f'$ at a starting point x_k. The next point x_{k+1} is then the intersection of the tangent at x_k and the abscissa. It can be calculated from

$$x_{k+1} = x_k - \frac{f(x_k)}{f'(x_k)}. \tag{5.10}$$

Newton's method comes with a number of advantages. The local convergence order is 2, it can be applied to functions of several dimensions, only one start point needs to be given. However, each point requires two evaluations, $f(x_k)$ and $f'(x_k)$. Convergence furthermore requires the starting point to be sufficiently close to the root for the method to converge. The convergence progress is thus strongly dependent on the evaluated function $f(x_k)$ itself.

This is illustrated in Fig. 5.4(a) using the example of a $T = f(\rho, e)$ iteration. For a known e_{it}, the temperature T_{it} is sought. Starting at an initial value

of T_0, the tangent intersects e_{it} at T_1. This will be a problem if the lowest library bound $T_{\min}$ is larger than T_1. Now, the tangent at T_1 is almost identical for all liquid values of e and will generally lead to a point close to T_2. A different problem arises in the vicinity of the critical point or the coexistence curve where the tangent is vertical and hence iterative progress negligible. Applying Newton's method to the problem of finding the temperature $T(e)$ from a given specific internal energy e, following Eq. (5.10) leads to the iteration scheme

$$T_{k+1} = T_k - \frac{e(T_k)}{e'(T_k)} = T_k - \frac{e(T_k)}{(\partial e(T_k)/\partial T)_v} = T_k - \frac{e(T_k)}{c_{\mathrm{v}}(T_k)}. \tag{5.11}$$

However, as discussed in Ch. 3, the specific heat capacities diverge in the vicinity of the critical point and the coexistence region. Then, $T_{k+1} \equiv T_k$ and convergence stalls.

Bisection

As an alternative, the less efficient but more robust bisection method is regarded. The main disadvantages are the first order global convergence rate, the restriction to one dimensional problems, and the need of two pairs of initial values. First, two starting points $x_{0,\mathrm{left}}$, $x_{0,\mathrm{right}}$ need to be chosen such that $f(x_{0,\mathrm{left}})f(x_{0,\mathrm{right}}) < 0$, i.e. $x_{0,\mathrm{left}}$ and $x_{0,\mathrm{right}}$ enclose the sought root. Correspondingly, $f(x_{0,\mathrm{left}})$ and $f(x_{0,\mathrm{right}})$ have different signs. This requires knowledge about the expected flow phenomena, such as minimum and maximum temperature. Then, the interval is divided

$$x_k = \frac{1}{2}(x_{k,\mathrm{left}} + x_{k,\mathrm{right}}) \tag{5.12}$$

and the function evaluated at x_k. The constrained interval is chosen according to

$$x_{k+1,\mathrm{left}} = \begin{cases} x_{k,\mathrm{left}} & \text{if} \quad f(x_k)f(x_{k,\mathrm{left}}) < 0 \\ x_k & \text{else} \end{cases} \tag{5.13}$$

and

$$x_{k+1,\mathrm{right}} = \begin{cases} x_k & \text{if} \quad f(x_k)f(x_{k,\mathrm{left}}) < 0 \\ x_{k,\mathrm{right}} & \text{else.} \end{cases} \tag{5.14}$$

The algorithm is illustrated in Fig. 5.4(b), $x_{0,\mathrm{left}} = T_l$ and $x_{0,\mathrm{right}} = T_r$ are the left (minimum) and right (maximum) start values of the problem, containing the sought root. T_1 is determined as next step between T_{l} and T_{r}. T_1 is chosen as the new right boundary because it now encloses the root. Then,

T_2 is computed to replace T_1 and so on until the method has sufficiently converged. By choosing the starting values as the minimum and maximum values of the library, it is ensured that the iteration will unconditionally remain within bounds. As the iterated function is strictly monotonous, the algorithm will also unconditionally converge to a unique solution.

Regula Falsi

This is acceptable when applied to continuously differentiable functions. However, in the present application, the library poses a lower boundary on smoothness below which the function is approximated piecewise linearly: Using a bisection algorithm on a library with $n = 1024$ rows, it takes a maximum of $\log_2(n) = 10$ steps to find the right cell. After reaching the cell, no accuracy can be gained beyond the inherent linear approximation. An algorithm with the robustness of the bisection which takes advantage of the piecewise linear structure is the regula falsi algorithm. Again, $x_{0,\text{left}}$ and $x_{0,\text{right}}$ are the bounds. But now, x_k is not simply chosen as the middle value but as the root if the function were linear:

$$x_k = x_{k,\text{right}} - \frac{x_{k,\text{right}} - x_{k,\text{left}}}{f(x_{k,\text{right}}) - f(x_{k,\text{left}})}. \tag{5.15}$$

In this way, once the right cell is found, the underlying assumption of the regula falsi is fulfilled, convergence is reached after one or two subsequent steps. The method has become dependent on the library values again but not on its derivatives. Regula falsi is illustrated in Fig. 5.4(c), $x_{0,\text{left}} = T_l$ and $x_{0,\text{right}} = T_r$ are the left and right bounds.

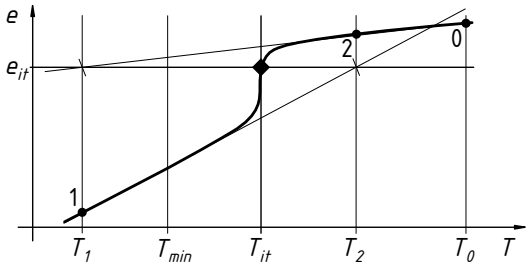

(a) Newton iteration.

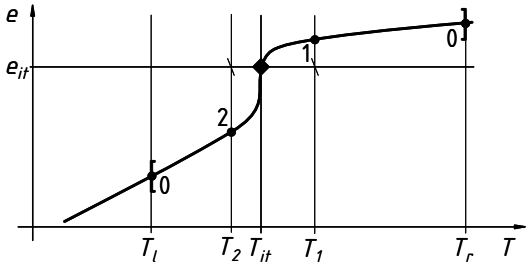

(b) Bisection algorithm.

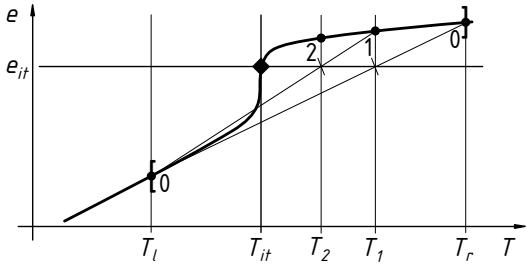

(c) Regula falsi algorithm.

Figure 5.4: Comparison of different iteration algorithms. While being potentially less efficient, the bisection algorithm prevents from leaving the library during iteration and is independent on local gradients. Regula falsi combines both, approximating linearly between steps.

5.5 Real Gas Library

The form of the library has to fulfill several demands. An appropriate range is determined by the required simulation boundary conditions: Injection of cryogenic oxygen in a fuel rich combustion chamber means that as all oxygen is consumed, oxygen partial density and partial pressure will vanish in the course of the simulation. Maximum values correspond to the injection conditions, temperatures reach from injection to the combustion temperature. Over the whole range, a sufficient resolution is required. In order to allow for a smooth transition to ideal gas, the coexistence region has to be completely enclosed in the library. Particularly this latter demand suggests a logarithmic scaling of the density, such that a parameter space of $\rho \in [1.0 \times 10^{-5},\, 1.2 \times 10^{3}]$ kg/m^3 is sufficiently resolved. The temperature domain is less sensitive, however a higher resolution in the coexistence region is desirable. All this is fulfilled by a representation in terms of ln(ρ)-ln(T).

5.5.1 Computing the MBWR Equation of State

Now an appropriate EOS has to be chosen to be evaluated for the library. As discussed in Ch. 3.1.2, there is a big variety of accuracy among the most commonly used EOS. According to Oefelein [116] and Pfennig [128], the Soave-Redlich-Kwong EOS is particularly suited for $p_\mathrm{r} < 1$, because it is fit to vapor pressure data. The Peng-Robinson EOS instead is the preferred EOS for $p_\mathrm{r} > 1$. Oefelein [117] characterized the MBWR EOS to be accurate over the widest range of pressures and temperatures, especially in near-critical conditions. The major disadvantage is said to be its high computational cost. Other authors share this view (Kuo [81], Yang [173]). Table 5.2 showed that most codes rely on SRK or PR EOS. For demonstrative purposes, the numerically expensive but accurate Modified Benedict Webb Rubin (MBWR) EOS by Younglove [176] has been chosen. It is repeated here for convenience from Eq. (3.18). In Appendix 1, the functions F_n are listed in Tab. 1, numerical values of the parameters for nitrogen and oxygen are compiled in Tab. 2.

$$p\left(\rho,T\right) = \sum_{n=1}^{9} \rho^{n} F_{n-1} + e^{-\delta^2} \sum_{n=10}^{15} \rho^{2n-17} F_{n-1} \tag{3.18}$$

Thermodynamic variables such as entropy, enthalpy, internal energy, specific heat at constant volume and at constant pressure, speed of sound are

calculated consistently from the EOS. The coexistence region is computed using a correlation of the vapor pressure,

$$\ln p_{\mathrm{sat}} = \ln p_{\mathrm{tr}} + \sum_{i=1}^{4} V_i x^i + V_5 x (1-x)^{V_6}, \tag{5.16}$$

with

$$x = \frac{1 - \dfrac{T_{\mathrm{tr}}}{T}}{1 - \dfrac{T_{\mathrm{tr}}}{T_{\mathrm{cr}}}}. \tag{5.17}$$

Necessary parameters are given in Tab. 3 in App. 1. The vapor density along the coexistence line is given by

$$\rho_{\mathrm{V}} = \rho_{\mathrm{cr}} + (\rho_{\mathrm{tr,V}} - \rho_{\mathrm{cr}}) \exp(f(T)) \tag{5.18}$$

where $\rho_{\mathrm{tr,V}}$ is the vapor density at the triple point and $f(T)$ is

$$f(T) = A_1 \ln(x) + \sum_{i=2}^{4} A_i (1 - x^{(i-5)/3}) + \sum_{i=5}^{13} A_i (1-x)^{(i-4)/3}, \tag{5.19}$$

using

$$x = \frac{T - T_{\mathrm{cr}}}{T_{\mathrm{tr}} - T_{\mathrm{cr}}}. \tag{5.20}$$

The corresponding liquid densities are fitted using

$$\rho_{\mathrm{L}} = \rho_{\mathrm{cr}} + (\rho_{\mathrm{tr,L}} - p_{\mathrm{cr}}) \exp(f(T)) \tag{5.21}$$

with the liquid density at the triple point $\rho_{\mathrm{tr,L}}$ and

$$f(T) = A_{14} \ln(x) + \sum_{i=15}^{17} A_i (1 - x^{(i-18)/3}) + \sum_{i=18}^{20} A_i (1 - x^{(i-17)/3}). \tag{5.22}$$

Coefficients for the density fits along the coexistence line are compiled in Tab. 4 in App. 1. The liquid mass fraction can be calculated from the fluid density ρ and the vapor (ρ_{V}) and liquid (ρ_{L}) densities at the coexistence line

$$x_{\mathrm{L}} = \frac{\rho - \rho_{\mathrm{V}}}{\rho_{\mathrm{L}} - \rho_{\mathrm{V}}}. \tag{5.23}$$

Vapor-liquid mixture properties are then interpolated from the respective

vapor or liquid values,

$$\phi = x_L \phi_L + (1 - x_L)\phi_V. \tag{5.24}$$

Specific enthalpy, specific inner energy, specific heat capacity, specific entropy, and speed of sound are calculated thermodynamically consistent from the relations Eqs. (3.31-3.36) as introduced in Ch. 3.1.5. The solution of the differentials found in Eqs. (3.31-3.36) for the MBWR EOS is discussed in Appendix 1.

5.5.2 Transport Coefficients

Real gas laminar viscosity μ and thermal conductivity k are calculated using the model of Lemmon and Jacobsen [91]. The laminar viscosity is split into a dilute gas part μ_{iG} and the real gas contributions μ_{rG}

$$\mu = \mu_{iG}(T) + \mu_{rG}(T_r, \rho_r). \tag{5.25}$$

The dilute part is calculated by

$$\mu_{iG}(T) = \frac{0.0266958\sqrt{MT}}{\sigma^2 \exp\left(\sum_{i=0}^{4} b_i \left[\ln(T^*)\right]^i\right)} \tag{5.26}$$

where σ is the Lennard-Jones size parameter. T^* is the temperature nondimensionalized with the Lennard-Jones energy parameter

$$T^* = \frac{T}{\epsilon/k}. \tag{5.27}$$

Parameters for Eqs. (5.26) and (5.27) are listed in Tabs. 5 and 6 in App. 2. The real gas departure function is

$$\mu_{rG}(T_r, \rho_r) = \sum_{i=1}^{n} N_i T_r^{-t_i} \rho_r^{d_i} \exp(-\gamma_i \rho_r^{l_i}), \tag{5.28}$$

with

$$\gamma_i = \begin{cases} 0 & \text{when } l_i = 0 \\ 1 & \text{otherwise.} \end{cases} \tag{5.29}$$

Tab. 8 in App. 2 lists the parameters t_i, d_i, and l_i. Parameters N_i are listed in Tab. 9 in App. 2. Thermal conductivity is expressed similarly as the departure from dilute behavior - here, Lemmon and Jacobsen did include a critical

enhancement parameter

$$k = k_{\mathrm{iG}}(T) + k_{\mathrm{rG}}(T_{\mathrm{r}}, \rho_{\mathrm{r}}) + k_{\mathrm{cr}}(T_{\mathrm{r}}, \rho_{\mathrm{r}}). \tag{5.30}$$

The dilute part can be computed from

$$k_{\mathrm{iG}} = N_1 \left[\frac{\mu^0(T)}{1\mu\mathrm{Pas}} \right] + N_2 T_{\mathrm{r}}^{-t_2} + N_3 T_{\mathrm{r}}^{-t_3} \tag{5.31}$$

The residual real gas contribution is

$$k_{\mathrm{rG}} = \sum_{i=4}^{n} N_i T_{\mathrm{r}}^{-t_i} \rho_{\mathrm{r}}^{d_i} \exp(-\gamma_i \rho_{\mathrm{r}}^{l_i}). \tag{5.32}$$

Parameters N_i are listed in Tab. 9 in App. 2. Finally, the critical enhancement is

$$k_{\mathrm{cr}} = \rho c_p \frac{k R_0 T}{6\pi\xi\mu(T,\rho)} (\Omega - \Omega_0) \tag{5.33}$$

with

$$\Omega = \frac{2}{\pi} \left[\left(\frac{c_p - c_v}{c_p} \right) \tan^{-1}(\xi/q_D) + \frac{c_v}{c_p} (\xi/q_D) \right] \tag{5.34}$$

and

$$\Omega_0 = \frac{2}{\pi} \left[1 - \exp\left(\frac{-1}{(\xi/q_D)^{-1} + \frac{1}{3}(\xi/q_D)^2 \rho_{\mathrm{r}}^{-2}} \right) \right]. \tag{5.35}$$

Younglove calculates ξ as

$$\xi = \xi_0 \left[\frac{\chi(T,\rho) - \chi(2T_{\mathrm{cr}}, \rho)(2T_{\mathrm{cr}}/T)}{\Gamma} \right]^{\nu/\beta} \tag{5.36}$$

where

$$\chi(T,\rho) = \frac{p_{\mathrm{cr}}\rho}{\rho_{\mathrm{cr}}^2} \left(\frac{\partial\rho}{\partial p} \right)_T. \tag{5.37}$$

Parameters for Eqs. (5.33) - (5.37) are listed in Tab. 7 in App. 2.

5.5.3 Library Function

The library is spanned as an equidistant grid in terms of ln (ρ) and ln (T). At any point in the simulation when information from the library is sought, both the real gas partial density and the temperature are given. Thus, the problem is essentially reduced to finding the right entry in the library. By

knowledge of the minimum and maximum value, $x_{\min}$, $x_{\max}$ as well as the number of points, the increment per cell Δx is calculated. The corresponding cell index is determined by

$$i_x = \text{floor}\left(\frac{x - x_{\min}}{\Delta x}\right). \tag{5.38}$$

The exact values are then determined by bilinear interpolation in the cell. The numerical cost of calling a value within the library should thus be essentially independent of library resolution and actual size.

5.5.4 Conclusion

Finally, the implemented library takes the shape shown in Fig. 5.5. For a

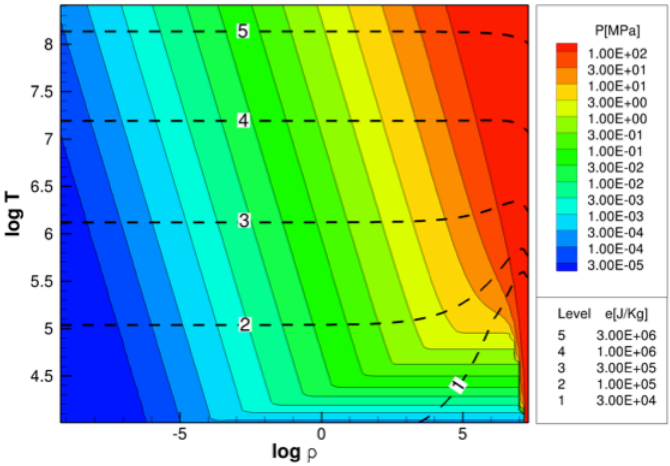

Figure 5.5: Oxygen equation of state in terms of $\ln T$, $\ln \rho$.

known density ρ and given either temperature T, specific inner energy e, or pressure p, the solution is unique and the problem well posed. Consistency is achieved by allowing only for one library, instead of providing a library for each problem $f(\rho,e)$, $f(\rho,T)$, $f(\rho,p)$. Thus, a T found for given ρ and e, will yield the identical value for e in turn when evaluating the corresponding ρ,T problem. While the implemented regula falsi algorithm merely shows sub-second order convergence, its unconditional stability and independence of convergence behavior on library content are preferred to the more efficient Newton algorithm for the present application.

5.6 Verification and Validation

In order to check whether the designed and implemented model is capable of fulfilling the requirements, benchmark problems are treated. First, the implementation of the model will be verified before it can be validated against physical problems.

5.6.1 Verification

Initially, a consistency check of the thermodynamics structure has been carried out. Starting with an initial state of density and temperature, the specific inner energy is computed using the $f(\rho,T)$ problem. This is then used in the $f(\rho,e)$ problem to determine p, which in turn is used to compute h from the $f(\rho,p)$ problem. From h, e can be computed to be used in $f(\rho,e)$ to compute T. The loop is complete, computed variables need to be identical to the initial values. The differences in T and the other state variables can be set with the convergence criteria in the thermodynamics iterations. The error could thus be adjusted to negligible values with the appropriate convergence criteria.

Then, TAU tabulated oxygen fluid data are compared to reference data from the NIST database [94], EOS from Schmidt and Wagner [142], transport coefficients from Laesecke et al. [84]. Figure 5.6 shows results for a number of fluid properties, namely density ρ, isobaric specific heat capacity c_p, specific enthalpy h, specific entropy s, viscosity μ, and thermal conductivity k. Fig. 5.6 also underlines the initial assessment of the quality of the MBWR EOS. Virtually no difference can be seen in the thermodynamic data derived from it. Merely the Lemmon-Jacobsen transport coefficients show minor deviations in the vicinity of the critical point.

Figure 5.7 shows a more detailed comparison between the MBWR equations of state with NIST data and the PR EOS for three pressures very close to the critical pressure. The specific enthalpy is matched very well by the MBWR EOS (Fig. 5.7(a)), the corrected PR EOS of Harstad et al. [62] deviates particularly below the respective pseudo-boiling temperatures. The derivative, the isobaric specific heat capacity c_p, exhibits some discrepancy mainly at the respective pseudo-boiling points, see Fig. 5.7(b). Both EOS show a comparable qualitative behavior. However, the error of the MBWR EOS is smaller and has almost vanished at a pressure of 7 MP, while the error of the PR EOS remains significant.

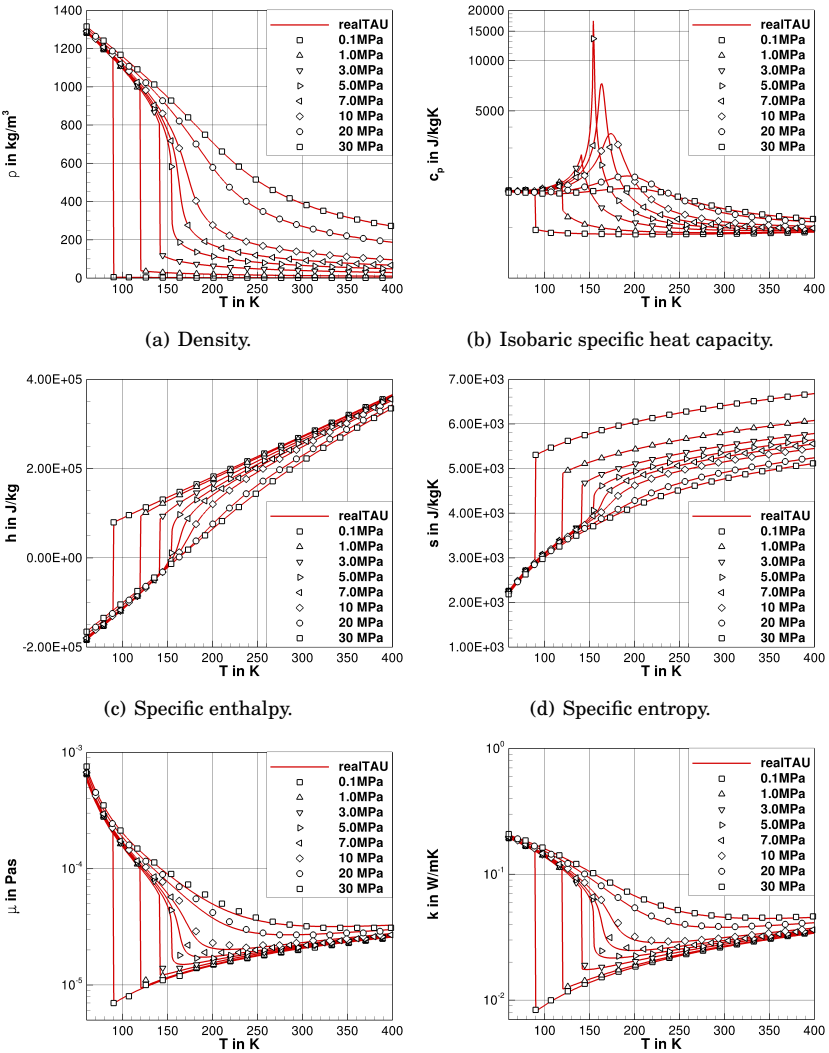

(a) Density.

(b) Isobaric specific heat capacity.

(c) Specific enthalpy.

(d) Specific entropy.

(e) Viscosity.

(f) Heat conductivity.

Figure 5.6: Comparison of TAU real gas library values (lines) with NIST (symbols) for oxygen at various sub- and supercritical pressures.

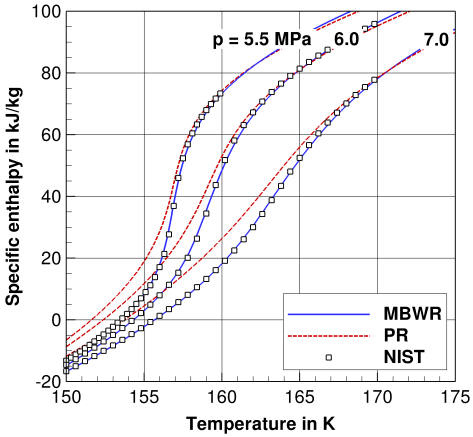

(a) Specific enthalpy.

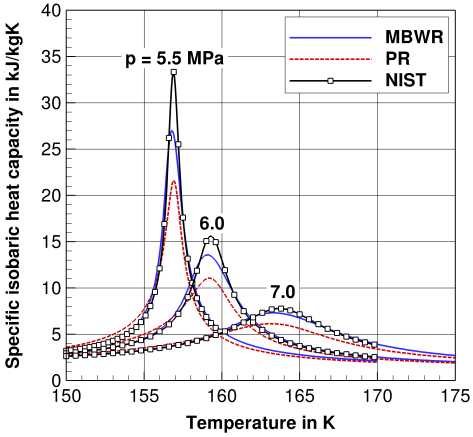

(b) Isobaric specific heat capacity.

Figure 5.7: Comparison of MBWR, PR EOS (Miller et al. [62]) with NIST for oxygen at near-critical conditions.

5.6.2 Validation

Once it has been shown that the values in the library do indeed model oxygen properties in an acceptable accuracy, the capability of TAU with real gas extension to solve physical problems needs to be validated. As the main task consists of developing a new thermodynamics model, the representation of fluid thermodynamics over all states is to be tested. 0D numerical simulations of standard idealized experiments, namely isobaric and isochoric heat addition, have been carried out. Illustrations are shown in Fig. 5.8. Heat

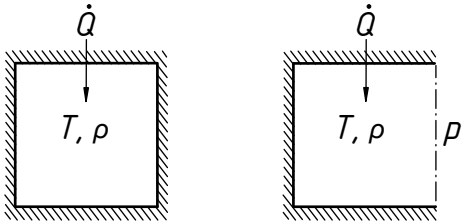

(a) Isochoric. (b) Isobaric.

Figure 5.8: 0D heat addition test cases.

addition is simulated by a volumetric energy source term [13], modified to supply a homogeneous energy distribution. Interestingly, the theoretical demand for existence of a homogeneous phase in equilibrium, ensured by solely allowing for quasi-static changes becomes a very real demand in CFD simulations. Inhomogeneous heat addition will lead to nonequilibrium pressure and heat distributions, in turn leading to undesired convection inside the cell. Too strong heat addition will lead to rapid expansion in the isobaric case, in turn leading to strong convection and again undesired pressure distributions inside the control volume.

Table 5.4 summarizes the initial states of the different test cases where P and V denote isobaric and isochoric cases, respectively. Figure 5.9 shows an overview of the computational results. Symbols correspond to CFD output, lines denote equal pressures or liquid mass fractions in the MBWR based library. On a first glance, isochoric cases run perfectly vertical, isobaric cases follow the EOS isobars. In the following, this will be discussed in more depth.

Case	T in K	ρ in kg/m^3	p in MPa	State
P1	70.0	1250.00	9.6	$p_\mathrm{r} = 1.9$
P2	69.0	1250.00	6.4	$p_\mathrm{r} = 1.3$
P3	100.0	1100.00	3.7	liquid
P4	80.0	1193.00	1.7	liquid
P5	80.0	1191.00	0.6	liquid
V1	70.0	1000	6.3e-3	vapor-liquid coexistence
V2	70.0	500	6.3e-3	vapor-liquid coexistence
V3	70.0	200	6.3e-3	vapor-liquid coexistence

Table 5.4: Initial states for 0D volumetric heating. P and V denote isobaric and isochoric cases, respectively.

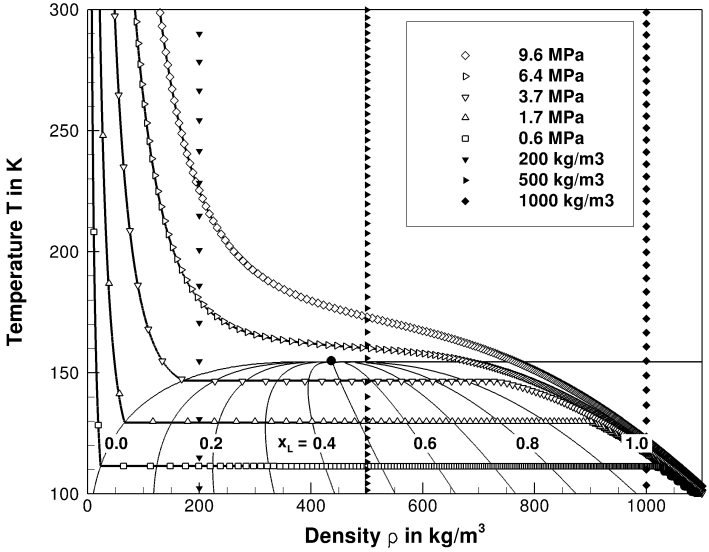

Figure 5.9: Results of 0D heat addition computations in ρ -T diagram. Initial states are compiled in Tab. 5.4.

Isochoric Heat Addition

The isochoric numerical computation is a rather verbatim implementation of the thought experiment. The idealized 0D control volume is closed with adiabatic walls. The fluid stays at rest during the state transition, mass and volume (and thus density) remain constant. Heat is added homogeneously, at constant volumetric power. The state change is thus expected to be

$$U_2 = U_1 + Q = U_1 + \Delta t \dot{Q}. \tag{5.39}$$

As a first step, time accurate heat addition is tested, to see whether the new thermodynamics model conserves energy. A cubic meter of a vapor-liquid mixture of oxygen is heated for 10 s with nominal $\dot{Q}_{\mathrm{nom}} = 2.0e7$ W. Figure 5.10 shows the evolution of temperature, inner energy, and specific inner energy for three different densities. The close-up to temperature in a one second interval in Fig. 5.10(a) shows a change in slope when leaving the vapor-pressure dome. The inner energy shows a behavior expected from a volumetric source term: regarding the specific value, the change is density dependent but Fig. 5.10(c) shows that the energy difference appears equal in all cases. Table 5.5 evaluates this in more detail. It compiles the inner energy at the beginning (U_1) and the end (U_2) of the ten second interval. $\dot{Q}_{\mathrm{act}} = (U_2 - U_1)/\Delta t$ is the actual heat added per unit time in the simulation. This is finally compared to the nominal value of $\dot{Q}_{\mathrm{nom}}$ for all densities: The relative error is $\Delta\dot{Q}_{\mathrm{rel}} = (\dot{Q}_{\mathrm{nom}} - \dot{Q}_{\mathrm{act}})/\dot{Q}_{\mathrm{nom}}$.

ρ in kg/m^3	Δt in s	U_1 in J	U_2 in J	$\dot{Q}_{\mathrm{act}}$ in W	$\Delta\dot{Q}_{\mathrm{rel}}$
200	10.0	8.6204e+06	2.0862e+08	2.0000e+07	0.00000
500	10.0	-2.7207e+06	1.9728e+08	2.0000e+07	0.00000
1000	10.0	-8.8255e+07	1.1172e+08	1.9997e+07	0.00015

Table 5.5: Time accurate results of isochoric heat addition with $\dot{Q}_{\mathrm{nom}} = 2.0e7$ W.

Next, specific inner energy is chosen as independent variable to demonstrate the process change merely in terms of thermodynamic state variables. Results are shown in Fig. 5.11, intervals are chosen to highlight the temperature range between 70 and 300 K. All three plots show that the computations started with a vapor-liquid mixture as start state. By adding heat, temperature and pressure rise. This leads to an increase in liquid mass fraction in all cases until the coexistence region is left, marked by reaching an x_{L} of either 1 or 0. Only for supercritical densities, as in Fig. 5.11(c), x_{L} diminishes

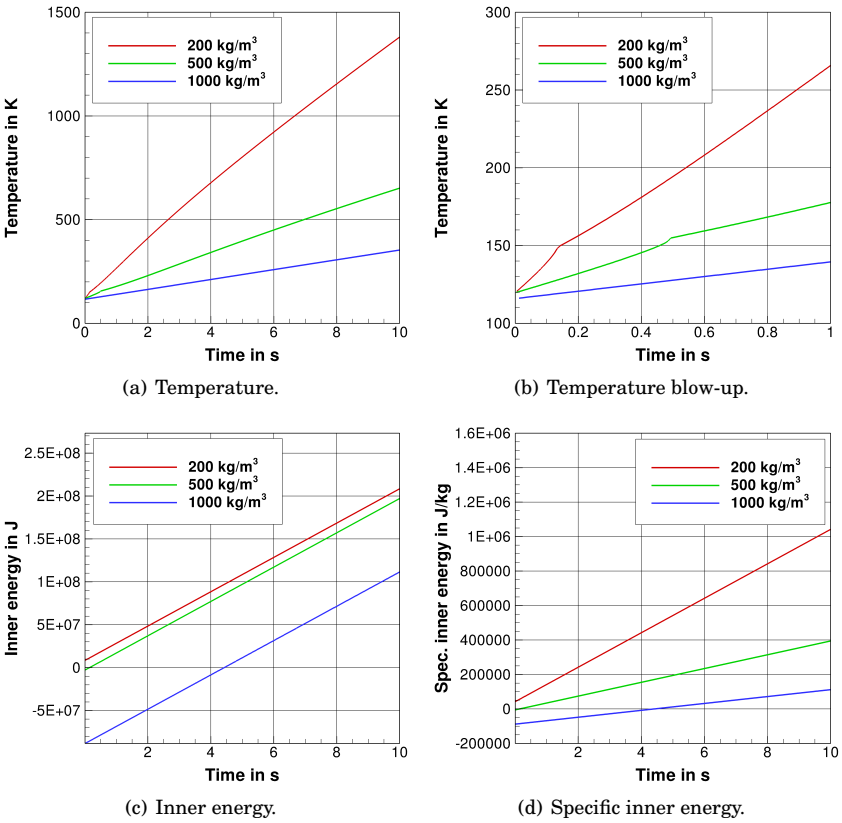

(a) Temperature.

(b) Temperature blow-up.

(c) Inner energy.

(d) Specific inner energy.

Figure 5.10: Time accurate computations of isochoric heat addition.

again before the vapor pressure dome is left. In all cases, leaving the coexistence region goes along with a distinct change in the pressure slope. The change in temperature slope reduces with growing density, until it is hardly discernible in the 1000 kg/m^3 case in Fig. 5.11(a).

Isobaric Heat Addition

Unlike the isochoric computation, the isobaric case is merely an approximation of the classical experiment. The experiment is set up as a closed system, involving a piston to allow for the fluid to expand. Similarly to Eq. (5.39) but

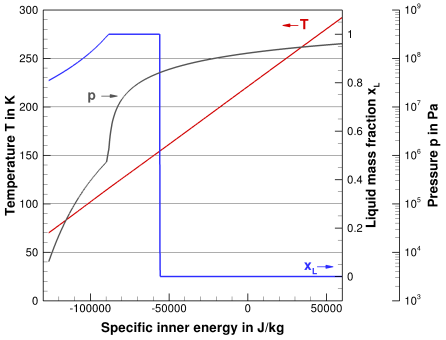

(a) V1: Isochoric 1000 kg/m^3.

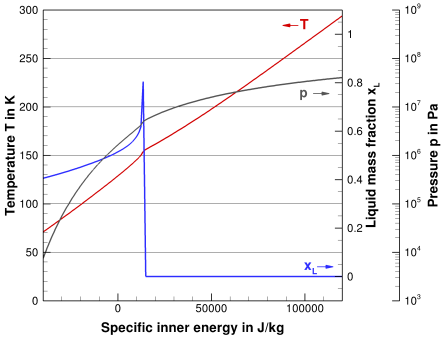

(b) V3: Isochoric 500 kg/m^3.

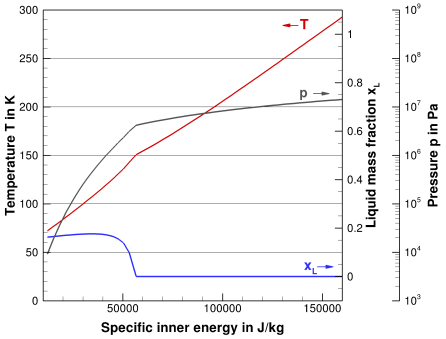

(c) V3: Isochoric 200 kg/m^3.

Figure 5.11: Development of temperature, liquid mass fraction, and pressure during isochoric heating in 0D computations.

taking into account the isobaric expansion, the energy balance is

$$H_2 = H_1 + Q = H_1 + \Delta t \dot{Q}. \tag{5.40}$$

Modeling this system including the moving piston, while possible, is beyond the scope of this work. Instead, a simplified numerical experiment has been set up. The constant pressure is not ensured by a moving piston but by a constant pressure outflow boundary condition, Fig. 5.8(b). Again, heat is added homogeneously into the system. By choosing a sufficiently low heating power, the flow stays essentially at rest, i.e. can be assumed quasi steady. Fig. 5.12 compares the effect of three different heating powers on the state development. It shows that for the three displayed levels, no effect on T and

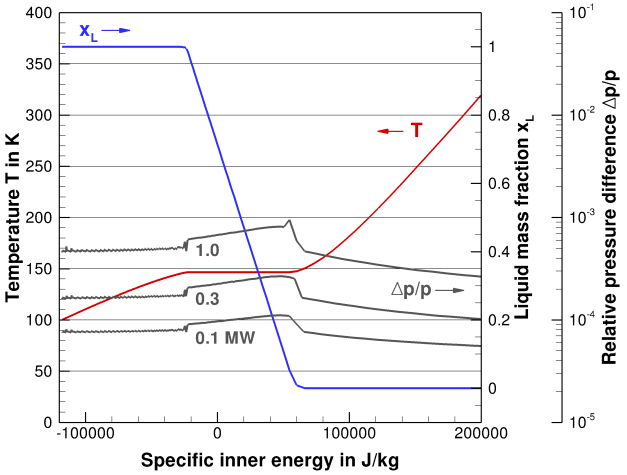

Figure 5.12: Influence of deposited power during heat addition.

x_L is discernible. The pressure difference $\Delta p/p$

$$\frac{\Delta p}{p} = \frac{p_\mathrm{cell} - p_\mathrm{boundary}}{p_\mathrm{boundary}} \tag{5.41}$$

is the relative difference between the pressure in the cell and the imposed boundary condition, necessary to induce the mass flow leaving the computational domain. In the limit, an infinitesimal difference follows the thermodynamic argument of a quasi steady process. It is hence a measure of nonequilibrium of the system.

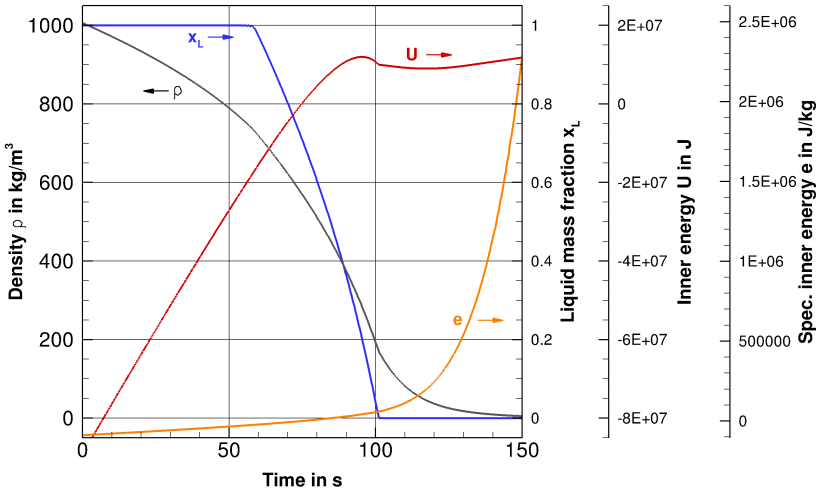

Figure 5.13: Reduction of inner energy in control volume during isobaric heat addition.

The mass leaving the system takes energy with it. This leads to the curious phenomenon that the inner energy inside the control volume, $U = \rho V e$, can be seen to actually *diminish* during heat addition: Figure 5.13 shows how density, liquid mass fraction, inner energy and inner specific energy change over time under volumetric heating at constant pressure. The example chosen is case P5. Prior to 100 s, just before all liquid is vaporized, the density (and thus mass) in the control volume changes fastest, causing a net outflux of inner energy. After 120 s, the density does not change strongly anymore, added heat mostly stays within the system - the inner energy rises again. As constant heating power is added to lesser and lesser mass, the specific inner energy e rises drastically after vaporization is complete.

Hence, Eq. (5.40) is not applicable, since the numerically regarded system is not closed. Figure 5.14 illustrates the difference. Initially, the ideal and the numerical system are identical, Fig. 5.14(a). As heat is added and the fluid expands, the numerical volume does not grow and hence does not contain all of the mass anymore, Fig. 5.14(b). The volumetric energy source now only acts on the part of the fluid remaining in the numerical control volume, heating it more than intended.

Two different remedies can be applied. First, the source term could be

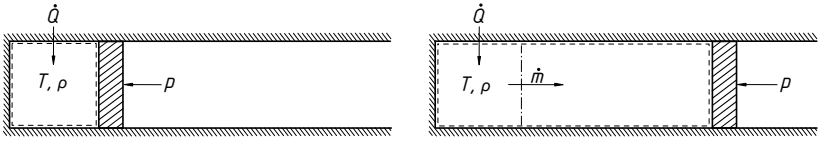

(a) Initial domain. (b) Final domain.

Figure 5.14: Numerical and ideal domain for isobaric 0D heating.

adapted in order to account for mass loss in the simulation. Effectively, a power applied per mass and not per volume would yield the desired effect. The difference in energy addition can then be thought to be applied outside the numerical domain to the mass already having left. The second approach is to account for the energy loss through the boundary, Eq. (5.43).

$$H_2 = H_1 + Q - H_{\text{loss}} \tag{5.42}$$

$$= H_1 + \Delta t \dot{Q} - \int_{\Delta t} \dot{m}(t) h(t)\,\mathrm{d}t \tag{5.43}$$

Again, there are two ways. First, the mass passing through the boundary can be integrated. However, this differential way will be error prone, as the mass fluxes are very small; added errors will lead to overall summed up errors. Instead, an integral way is followed: by regarding the change in density *inside* the computational cell, the mass difference can be estimated $\dot{m}_{\text{cell}} = -\dot{m}_{\text{loss}}$, summation errors can be avoided this way. The exact mass having left the system between two time steps is known, the enthalpy is approximated by an arithmetic mean, applying the trapezoidal rule,

$$H_{\text{loss}} = \int_{\Delta t} \dot{m}(t) h(t)\,\mathrm{d}t = \int_{\Delta t} h(t)\,\mathrm{d}m \approx \sum_{n=1}^{N} \frac{1}{2}(h^n + h^{n-1}) V(\rho^n - \rho^{n-1}). \tag{5.44}$$

Here, n denotes the current time step, $n-1$ accordingly the previous step. Now, H_2 is determined twice. First, $H_{2,\text{int}}$ can be integrated from the simulation log file using Eq. (5.44). It can then be compared to $H_{2,\text{act}}$, the actual value from the numerical simulation. The relative deviation is computed as $\Delta H_{2,\text{rel}} = (H_{2,\text{int}} - H_{2,\text{act}})/H_{2,\text{act}}$. The computation was executed for 650,000 time steps. The number of intervals of evaluation is N, i.e., $N = 100$ corresponds to an evaluation every 6,500 steps. The result of the numerical integration approaches the simulated value with increasing resolution of intervals.

	$N = 100$	1000	2166
Δt in s	186.423	187.144	187.294
Δm_{loss} in 10^3 kg	1.0960	1.0961	1.0962
Q_{nom} in MJ	186.42	187.14	187.29
H_{loss} in MJ	44.649	44.713	44.815
$H_{2,\text{act}}$ in MJ	15.677	16.333	16.382
$H_{2,\text{int}}$ in MJ	16.234	16.355	16.381
$\Delta H_{2,\text{rel}}$	$3.4e-02$	$1.3e-03$	$-5.2e-05$

Table 5.6: Time accurate results of isobaric heat addition with a nominal $\dot{Q}_{\text{nom}} = 1.0e6$ W and an initial $H_1 = -126.1$ MJ, case P3.

This evaluation is summarized in Tab. 5.6. More than a quarter of the added energy is found to leave the numerical system.

Again, after having shown the time accurate computation to work, the abscissa variable is replaced by inner energy as the runtime variable. Figure 5.16 shows results for 0D isobaric heat additions for sub-, Figure 5.15 for supercritical pressures. The supercritical cases Figs. 5.15(a) and 5.15(b) show a smooth rise in temperature for rising specific inner energy. Passing through the Widom line, the temperature rise slows down, the closer to the critical point, the more pronounced. By definition, the liquid mass fraction drops to zero as the critical temperature is surpassed. Figures 5.16(a) and 5.16(b) show the heating process at subcritical pressures. The characteristic temperature plateau when passing through the coexistence region is captured, the temperature continues to increase once all liquid oxygen is vaporized.

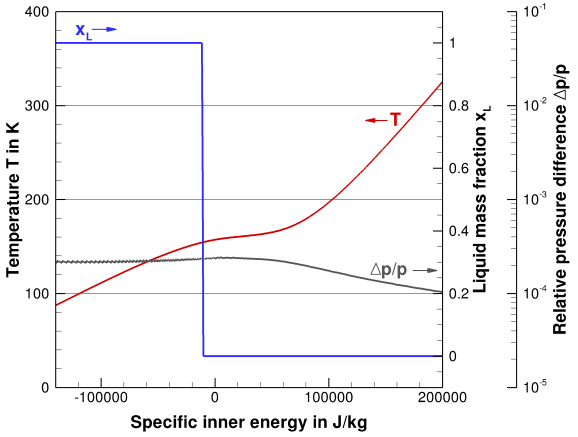

(a) P2: Isobaric 6.9 MPa.

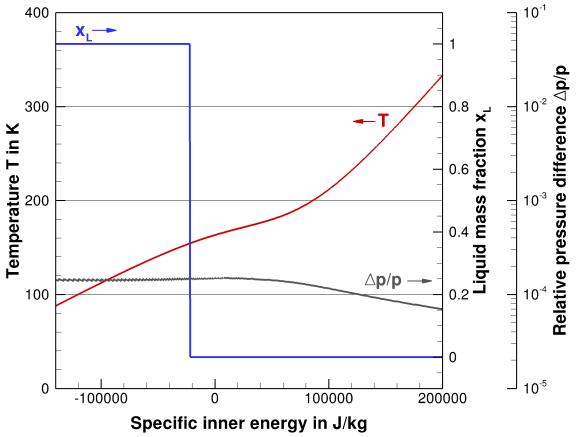

(b) P1: Isobaric 9.6 MPa.

Figure 5.15: Development of temperature, liquid mass fraction, and pressure during heating in 0D computations at supercritical pressures.

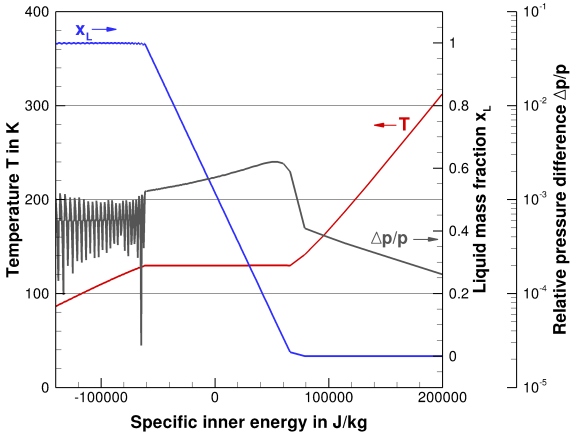

(a) P4: Isobaric 1.7 MPa.

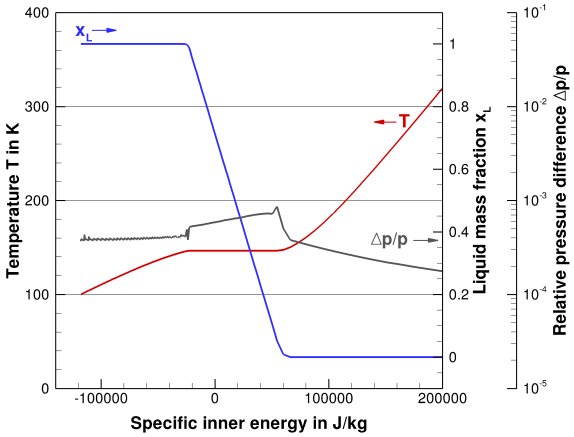

(b) P3: Isobaric 3.7 MPa.

Figure 5.16: Development of temperature, liquid mass fraction, and pressure during heating in 0D computations at subcritical pressures.

Influence of Library Resolution

It could be shown that the model is capable of calculating vaporization of liquid oxygen; now the question arises how the model performs out of its intended application. The performance needs to be measured in terms of computational cost, accuracy, and memory demands. Four libraries with varying resolutions have been tested for P3, the 0D isobaric heating case at 3.7 MPa. Data are compiled in Tab. 5.7. The libraries span from 13 MB to 1.8 GB in size. After the libraries are loaded, no correlation between size and runtime could be found[5].

Resolution	Low	Medium	High	Very high
# Data points	100,000	500,000	4,500,000	15,000,000
# T points	500	1,000	3,000	5,000
# ρ points	200	500	1,500	3,000
Filesize	13 MB	62 MB	550 MB	1.8 GB
Runtime	126.9 s	130.5 s	119.2 s	108.7 s

Table 5.7: Comparison of library resolutions for isobaric heating of oxygen at 3.7 MPa.

Figures 5.17 and 5.18 compare the results of libraries with different resolutions. Similar to what Fig. 5.16(a) shows, pressure oscillations can be seen in liquid states, particularly for the lower two resolutions, Figs. 5.18(a) and 5.18(b). The results of the two higher resolutions, Figs. 5.17(a) and 5.17(b) are virtually identical. It can be concluded that the oscillations are indeed a resolution effect and can be avoided by appropriately choosing the resolution in the state space of interest. Thus, the high resolution library has been chosen for the subsequent computations. It is important to point out that this inclination to oscillations is an effect of the deliberate choice of EOS discretization and by no means inherent in the model. If instead an approach is used which uses refined cells in the liquid domain, as opposed to coarse cells as in the present implementation (due to the logarithmic scaling), the effect is expected to be much less pronounced.

[5] Shown is the average over three runs. The CPU run times for the medium resolution library varied between 117 s and 139 s, encompassing all found variation between library sizes.

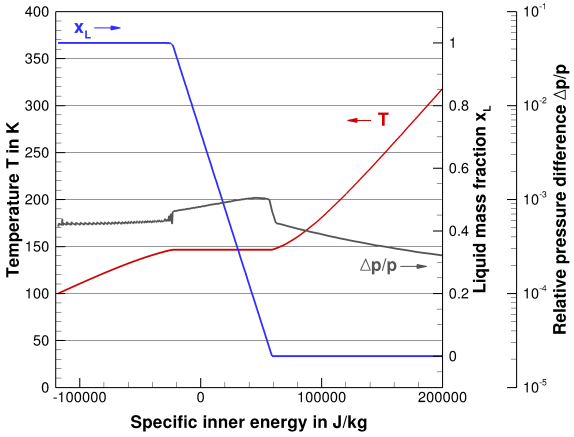

(a) High.

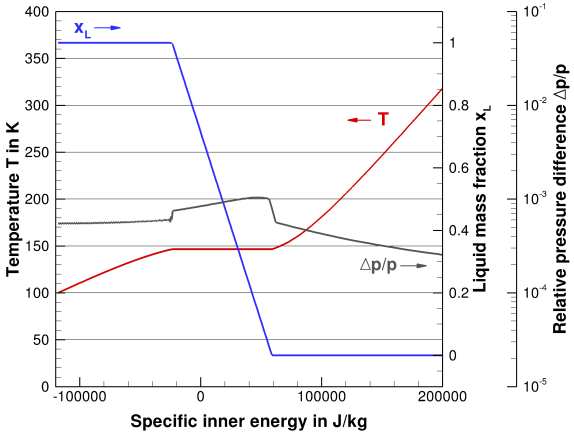

(b) Very high.

Figure 5.17: Higher library resolutions on 0D isobaric computations at 3.7 MPa.

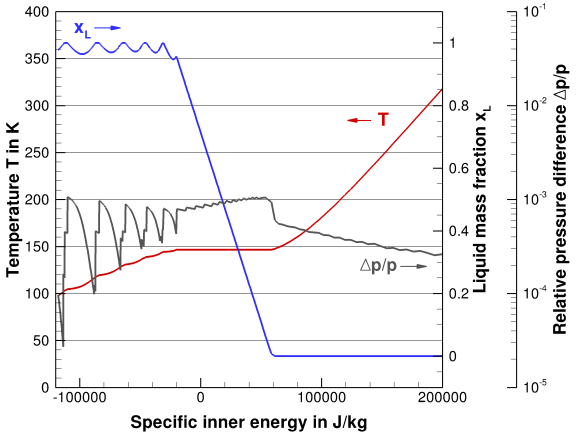

(a) Low.

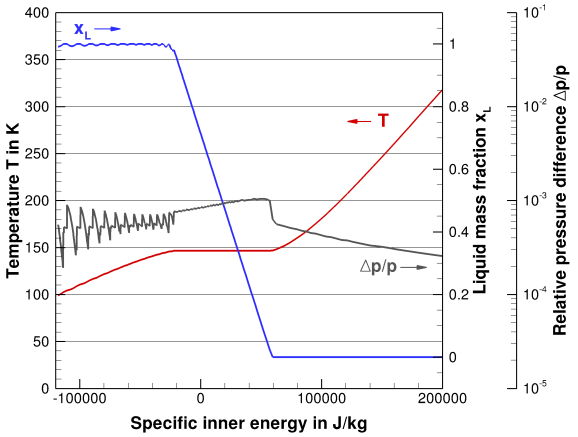

(b) Medium.

Figure 5.18: Lower library resolutions on 0D isobaric computations at 3.7 MPa.

1D Premixed Combustion

The implemented model has been tested in a pure fluid application, the next step is to regard a mixture. In accordance with Oefelein's assessment for a coaxial injector, the mixing and combustion test case is carried out at a high temperature ideal gas state. The non equilibrium chemistry infrastructure is tested along with the EOS library infrastructure in a quasi-1D test case, Fig. 5.19. In this Mach 3 inviscid channel flow, a stoichiometric mixture of oxygen and hydrogen is provided at 1200 K and 1 bar, sufficient to ensure auto-ignition. Figure 5.19(b) shows how after a certain ignition delay combustion occurs with the associated temperature rise.

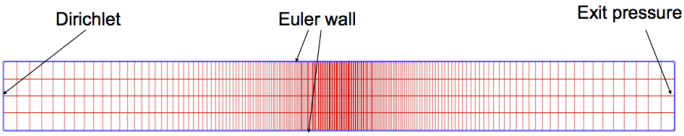

(a) Quasi 1D grid.

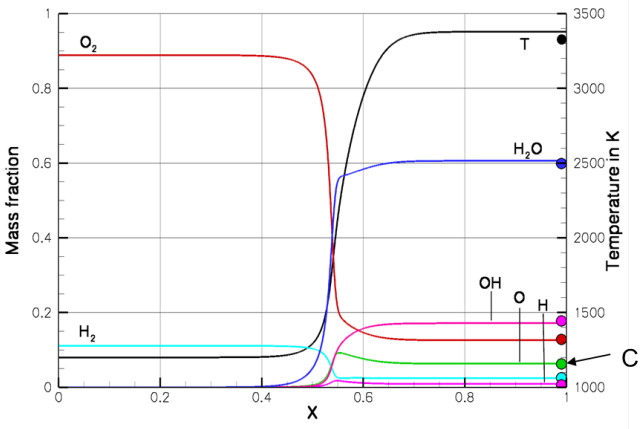

(b) Spatial 1D flame structure. Lines denote mass fractions and temperature. Symbols represent CEA chemical equilibrium results.

Figure 5.19: 1D combustion validation

The TAU equilibrium composition eventually attained is compared with a CEA [110] computation for the given composition and the channel outflow pressure. Figure 5.19(b) shows the results, CEA data are marked with symbols. Agreement is very well.

5.7 Conclusion

A new Eulerian real gas model has been developed and implemented into the TAU code. Primary application is reactive coaxial injection in cryogenic liquid propellant rocket engines. Physically, this corresponds to a diffusion flame, isolating the cryogenic oxygen from the surrounding flow. It could be shown that mixing in these conditions is essentially an ideal gas process. The introduced model has been designed to take full advantage of this. Two main differences distinguish real gas TAU from state of the art codes: First, by employing a multi-fluid mixing model, a different equation of state can be used for each species. A state equation for a real gas only needs to be solved for the species which acts as a real gas, i.e. oxygen. Beyond, the new model simply reverts to applying the appropriate ideal gas equation of state, significantly reducing computational time and improving stability. Using several equations of state allows the second main difference: Thermodynamic real gas data are stored in a precomputed library. Then, accurate but numerically costly equations of state can now be used without runtime penalty; in fact using the real gas version virtually introduces no penalty over ideal gas computations. Furthermore, computationally expensive and potentially unstable iterations of thermodynamic states in the multiphase region or the vicinity of the critical point are carried out during a preprocessing step, further accelerating and stabilizing the model during runtime.

Initially limiting the application to diffusion flames allows for a step-wise validation/verification process: As mixing occurs in an ideal gas state only, the transition from a real gas to an ideal gas takes place before mixing. It follows that encountered real gas effects are pure fluid phenomena, restricted to the pure oxygen dense core. Then, real fluid behavior can be verified/validated as a pure fluid; mixing can be verified/validated as ideal gas processes.

The new real gas model has been verified against the NIST database and validated by simulating idealized quasi 0D and 1D processes, involving heat addition, phase change, and combustion. The last step of the validation process is the initially envisioned application: reactive coaxial injection using cryogenic oxygen. This case will be discussed in Ch. 6.3.

6 Applications

6.1 Cryogenic Injection Experiment

A new perspective on injection processes at supercritical pressures, especially dia-Widom processes, has been developed in Ch. 3. This can now be applied to the questions raised in Ch. 1.3, concerning the nature of the axial density distributions of the cryogenic nitrogen injection experiments. The experiments have been carried out at DLR Lampoldshausen. Results have been published by Mayer, Tamura, Telaar, Branam, Hussong, and Schneider in [22, 23, 104, 108, 109]. Different aspects and data are discussed in each paper. Here, this information is combined to gain extended insight.

The experiments are of high practical value as they remain popular for CFD code validation. Despite ambiguities in results and experimental conditions, the campaign remains one of the most thoroughly documented of pure fluid cryogenic injection at high pressures. Furthermore, the data have been used to design a numerical test case within the 2001 Rocket Combustion Modeling workshop (RCM) [56], in turn spawning a number of numerical results which serve as benchmarks for other CFD codes.

The published properties of the experiment are summarized in Ch. 6.1.1. The experimental findings are analyzed in Ch. 6.1.3, using the results of Ch. 3. The hypothesis of thermal atomization is tested in Ch. 6.2 by a CFD computation using the model introduced in Ch. 5.

6.1.1 The Experiment

Facility

Figure 6.1 is a schematic of the test chamber. It consists of a circular cylinder with 122 mm diameter and 1 m length. Optical access is given through windows at opposing sides. The injector plate is moved in axial direction in order to allow measurements of jet properties at different distances from the face plate. The cylinder wall is heated to 298 K; the injector, faceplate, and windows are not heated. Nitrogen is injected at the center of the faceplate

through a cylindrical injector with 2.2 mm diameter. The injector is 90 mm long, preceded by a 6 mm diameter tube. The pressure in the chamber is controlled via a pressure valve.

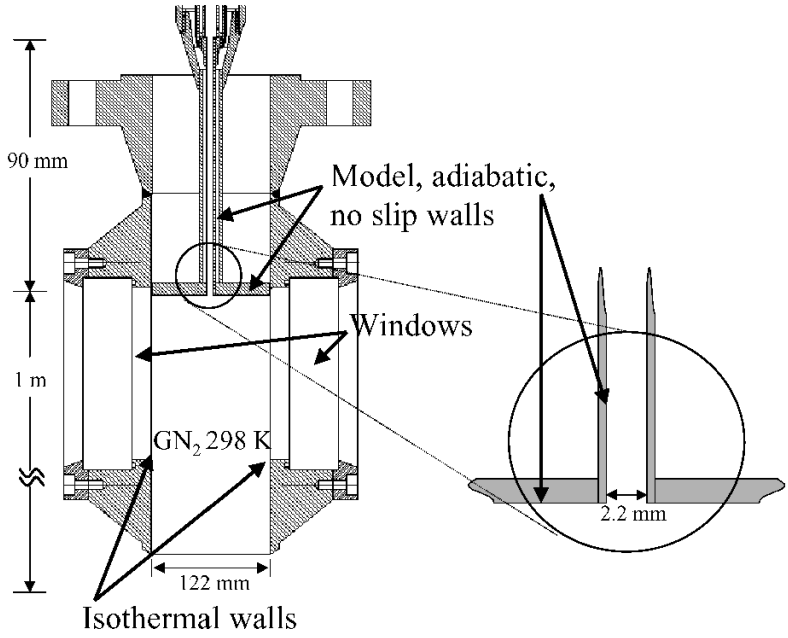

Figure 6.1: Nitrogen injection test chamber, from Branam and Mayer [23].

Procedure

The experiment was conducted as follows. The chamber was pressurized with nitrogen and kept at 298 K. Cryogenic nitrogen was fed through the injector, the mass flux was controlled. As shown in Fig. 6.2(a), the temperature was measured immediately in front of the convergent part of the injector, i.e. 90 mm upstream of the injector exit. The cryogenic nitrogen cools the structure of the injector. When the measured temperature T1 reached the nominal temperature of the experiment, the Raman density measurements were carried out through the windows. In order to measure the temperature of the injected fluid, a subsequent experiment was carried out in the very same manner, except that instead of the Raman measurement, a thermocouple of

1 mm diameter was introduced into the free jet in two orientations: radially, 1 mm downstream of the injector exit (T2a), see Fig. 6.2(b), and axially, reaching 1 mm inside the injector (T2b).

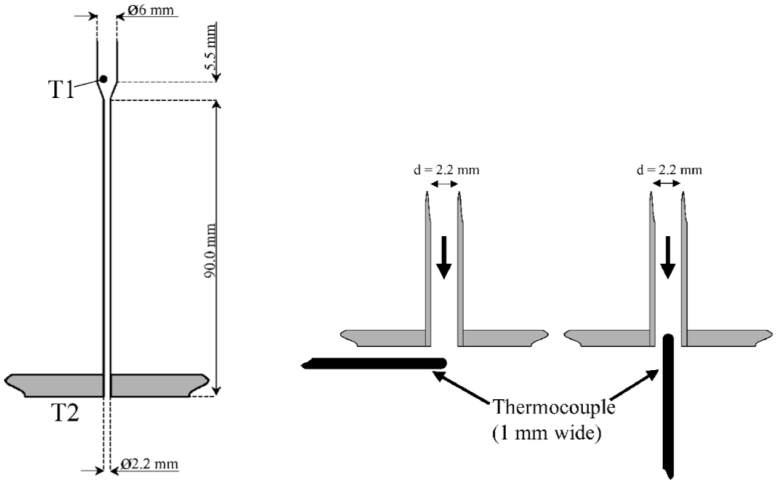

(a) Positions of T1 and T2 temperature measurements.

(b) Difference in orientation of T2a (left) and T2b (right) measurements.

Figure 6.2: Temperature measurement positions, from Mayer et al. [109].

Test Matrix

The target test matrix of the experiments is compiled in Tab. 6.1, case numbering follows Mayer et al. [109]. The test matrix comprises injection temperatures of 120 and 130 K, pressures of 4.0, 5.0, and 6.0 MPa, and injection velocities of 2.0 and 5.0 m/s. Originally, injection at 100 K has been carried out as well but axial density data are not published. The 100 K cases are listed in Branam and Mayer [23] only and differ from Mayer's list. Further, no axial density distributions are published for cases 1, 2, 11, and 12. Only nondimensional axial results are published for case 4, dimensional values need to be reconstructed from radial density data.

Results

Owing to the mode of conductance of the experiments, the target temperature was measured as T1. Temperature measurements T2a and T2b were found to deviate from this value. Furthermore, the achieved chamber pressure differs slightly from the intended value. The obtained test matrix is compiled in Tab. 6.2. Along with p and T, a velocity is published which has been calculated from the mass-flow using the continuity equation. The density for the continuity equation was calculated from temperature T1 and the chamber pressure using the MBWR EOS.

Obtained axial density distributions are shown in Fig. 6.3, repeated from the introduction. Interruptions in the data can be seen at $X/D = 10$ and at $X/D = 20$. This is due to the limited optical access which required two translations of the faceplate to measure as far downstream as 30 D.

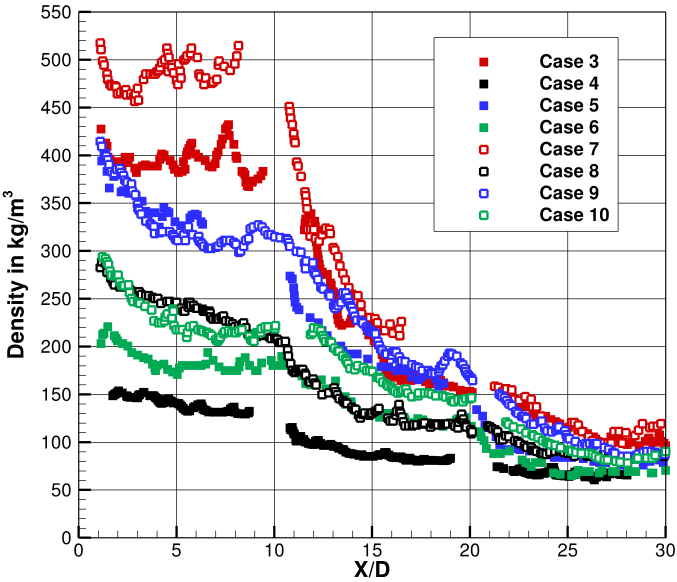

Figure 6.3: N_2-N_2 axial density distributions (Mayer et al. [109]).

Case	Target pressure in MPa	Target velocity in m/s	Target temp. in K
1	4.0	2.0	120.0
2	4.0	2.0	130.0
3	4.0	5.0	120.0
4	4.0	5.0	130.0
5	5.0	2.0	120.0
6	5.0	2.0	130.0
7	5.0	5.0	120.0
8	5.0	5.0	130.0
9	6.0	2.0	120.0
10	6.0	2.0	130.0
11	6.0	5.0	120.0
12	6.0	5.0	130.0

Table 6.1: Target test matrix (Mayer et al. [109]).

Case	Measured pressure in MPa	Computed velocity in m/s	Meas. T1 in K	Meas. T2a in K	Meas. T2b in K
1	3.96	1.8	120.4	130.0	122.2
2	3.95	2.7	129.4	140.0	131.9
3	3.97	4.9	120.9	126.9	122.9
4	3.98	5.4	130.7	137.0	133.3
5	4.90	2.0	120.7	131.0	122.6
6	4.90	1.9	129.8	140.0	131.5
7	5.01	4.5	120.7	126.2	122.5
8	5.00	4.9	130.2	135.7	131.7
9	5.85	2.0	120.7	135.0	122.8
10	5.88	1.9	129.9	140.5	131.9
11	5.98	4.9	121.7	128.7	123.3
12	5.96	4.9	130.8	135.4	132.3

Table 6.2: Experimentally obtained test matrix (Mayer et al. [109], T1 from Branam and Mayer [23]).

6.1.2 The Experiment in CFD

The 2001 RCM1 Test Cases

Within the Rocket Combustion Modeling workshop RCM in 2001 [56, 103], pure fluid nitrogen injection was defined as a numerical test case before data were published otherwise. In order to ensure a comparability of the CFD results submitted to the workshop, a set of numerical boundary conditions was specified for the participants to follow. The chamber is assumed to be axisymmetric. All wall boundary conditions are no-slip. The injector and faceplate are treated as adiabatic, the chamber walls are isothermal at 297 K. Initial conditions in the chamber are the specified pressure and a temperature of 297 K. Tab. 6.3 summarizes the conditions for the two test cases. Figure 6.4 demonstrates how sensitive with regard to the temperature the test cases were chosen. Furthermore, it can be seen that the fluids no longer behave like ideal gases.

		RCM1A	RCM1B
Chamber pressure in	MPa	3.97	5.98
Injection temperature in	K	126.9	128.7
Injection density in	kg/m^3	457.5	514.0
Mass flow in	kg/s	0.00995	0.01069
Injection velocity in	m/s	0.769	0.736
Corresponding Mayer case		3	11

Table 6.3: RCM1 numerical boundary conditions (Mayer [103]).

Comparing the specified pressure and temperature with the measured values in Tab. 6.2, we can conclude that RCM1 A and B are based on Cases 3 and 11, respectively. Furthermore, T2a appears to have been chosen as RCM1 reference temperature.

CFD in the Literature

Being a dedicated test case for CFD, the Mayer and Branam experiments have been simulated by numerous researchers (e.g. Kim et al. [77], Müller et al. [112], Niedermeier et al. [115], Branam et al. [24], Schmitt et al. [144, 145], Hickey et al. [63], Cutrone et al. [37, 38], Cheng and Farmer [36],

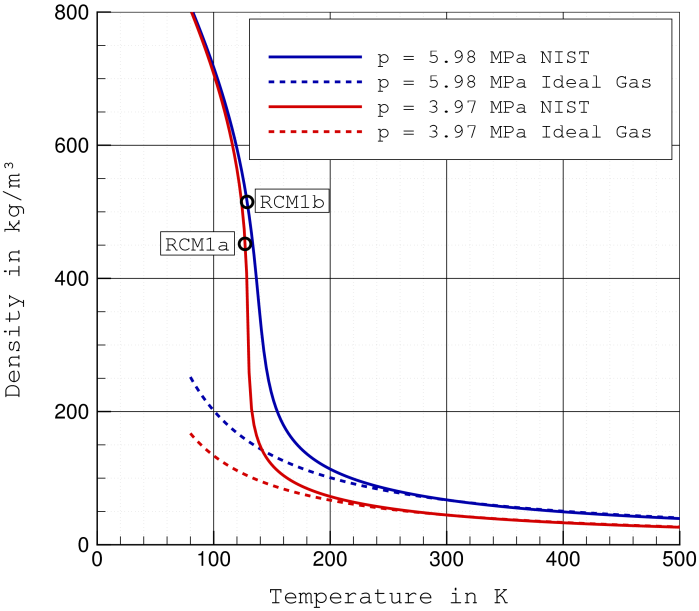

Figure 6.4: Nitrogen density for RCM1 pressures, real gas data from NIST [94], Span et al. [152].

Jarczyk et al. [71]). Exemplarily, two sets of results are shown in Fig. 6.5; the left and right plots show results for cases 3 and 4, respectively. The first row is from Mayer himself, Fig. 6.5(a). The CFD model is incompressible steady RANS, using an axisymmetric grid. The second row, Fig. 6.5(b), stems from a recent high fidelity, unsteady, 3D LES computation by Schmitt et al. [145]. Note that Schmitt's plots are extended to $X/D = 40$ compared to Mayer's $X/D = 30$.

Case 3 is matched very well by both approaches. The dilution of the dense jet in axial direction was computed excellently. Both models predict the correct length of the dense core. Had the initial density been rather chosen to equal 400 kg/m^3, agreement might be even better[1]. The picture looks different for case 4. While Mayer's RANS matches the axial decline in density

[1]Unlike Mayer, Schmitt used a density lower than the 457.5 kg/m^3 suggested in the RCM description, choosing instead what appears to be the highest measured density.

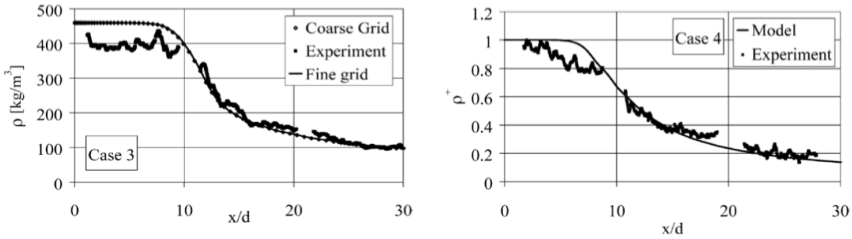

(a) RANS from Mayer et al. 2003 [109]. Case 3 (left), case 4 (right).

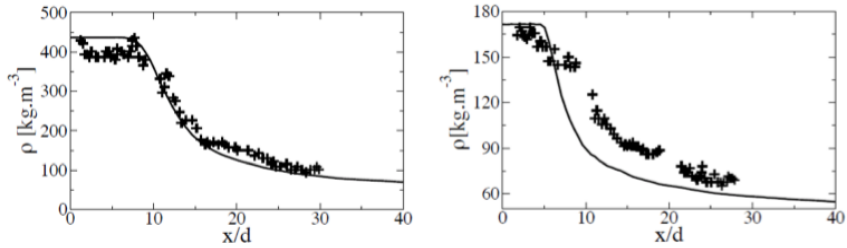

(b) LES from Schmitt et al. 2010 [145]. Case 3 (left), case 4 (right).

Figure 6.5: Comparison of numerical and experimental results for Mayer nitrogen injection cases 3 (left column) and 4 (right column). Thick symbols denote experimental results, the CFD solution is the thin line.

after $X/D = 10$ very well, this is not true for the LES computation. Both CFD methods again predict the same dense core length. However, this time, the experimental data is not matched at all. Instead of exhibiting a distinct dense core, as introduced in Ch. 2.2.1, the measured density appears to drop right upon entering the chamber. Other researchers who carried out CFD simulations of case 4 are Kim et al. [77], Müller [112], Niedermeier [115]. *All* found a constant density core in case 4 which is not supported by experimental results. Two main conclusions can be drawn:

1. No general superiority of LES compared to RANS for the addressed cases is found. This might be attributed to the possibility of tuning RANS turbulence models to particular cases which does not exist to this extent in LES models.

2. There exists a systematic discrepancy between CFD results and experimental data for case 4 for *all* numerical models.

Thus, a more in-depth analysis of the injection experiment is in order.

6.1.3 Analysis

Uncertainties and Ambiguities

Not all idealizations and assumptions were actually fulfilled in the experiment. The mass flow rate is only published for the two RCM1 cases. The chamber state was not known for the specific time when the density was measured: Cryogenic nitrogen was injected into the chamber for an unspecified time until T1 matched the target temperature. It can be assumed this reduced the temperature and increased the density in the chamber. While chamber walls were heated to 297 K, this was not the case for the windows. The chamber cross section enclosed by the windows is quadratic and not axisymmetric.

Injector Wall Heat Flux Hypothesis

The least valid simplification in the RCM CFD boundary conditions is probably the negligence of heat flux in the injector. Analyzing the different temperatures measured for a single case, Mayer et al. [104] already suggested that heat transfer, somewhat unexpectedly, played a role. Both they and Kim et al. [77] speculated about neglecting injector heat flux to be responsible for discrepancies between numerical and experimental results. Figure 6.6 compares experimental data with numerical axial density distributions associated to the different temperatures measured at T2. Neither matches the measured density close to the injector which can hence be associated with yet another temperature. Furthermore, the target temperature T1 is different from all three temperatures. Thus, there are four different temperatures associated with each experiment.

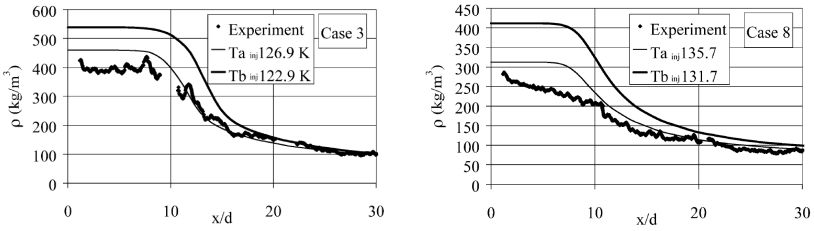

(a) Case 3.

(b) Case 8

Figure 6.6: Ambiguity of measured temperatures from Mayer et al. [109].

If heat transfer in the injector is relevant, the variations must not be random but a temperature increase must be visible following the injector downstream. T1 needs to be the lowest, the temperature upon entering the chamber the highest temperature. The difference between T2a and T2b is less straightforward. However, the thermocouple T2b is fully immersed in the center of the stream which would be heated last from the injector walls. It is also placed a bit upstream compared to T2a. The thermocouple oriented perpendicular to the jet flow, T2b, is more likely to entrain fluid from the heated boundary layer or even measure the heating of the thermocouple itself being immersed in warmer flow. This order is in fact seen in the results. Case 3 can be used as an illustrative example, see Fig. 6.6(a) and Tab. 6.2. Nitrogen enters the injector at T1 = 120.4 K. Flowing downstream, it is slowly heated from the injector wall. Close to the injector exit, the stream center has been heated to T2b = 122.9 K, T2a has already reached 126.9 K. The constant density core seems to oscillate around a mean of 400 kg/m^3, corresponding to a temperature of 128.6 K. This supports the notion of a finite injector wall heat flux.

Axial Density Distributions

So far, there appears to be no systematic analysis of the measured density distributions by other authors [2]. To make them comparable, the data are first expressed in nondimensional form using Eq. (6.1),

$$\rho^+ = \frac{\rho - \rho_\infty}{\rho_{\text{in}} - \rho_\infty}. \tag{6.1}$$

The injection density ρ_{in} corresponds to the highest, the background density ρ_∞ to the lowest measured density. The results are then grouped in terms of injection velocity and temperature. Each of the plots in Fig. 6.7 shows the distribution at two pressure levels with otherwise comparable parameters. The distributions in each figure clearly resemble each other. Furthermore, a categorization can be carried out depending on the density distribution characteristics. Three types can be distinguished. Figure 6.7(a) shows a region of constant density after injection, resembling a liquid or potential core, corresponding to Fig. 6.8(a). Second, a strictly monotonous slope with density dropping off immediately upon injection, as shown in Fig. 6.8(b), can be found in the experiments of Fig. 6.7(b). Finally, a density slope followed

[2] Banuti and Hannemann [15]

by a plateau, illustrated in Fig. 6.8(c) is exhibited by experiments shown in Figs. 6.7(c) and 6.7(d).

Of the eight shown density distributions, only two exhibit a dense core as expected from classical mechanical jet break-up theories. For the other cases, a constant density core is not seen.

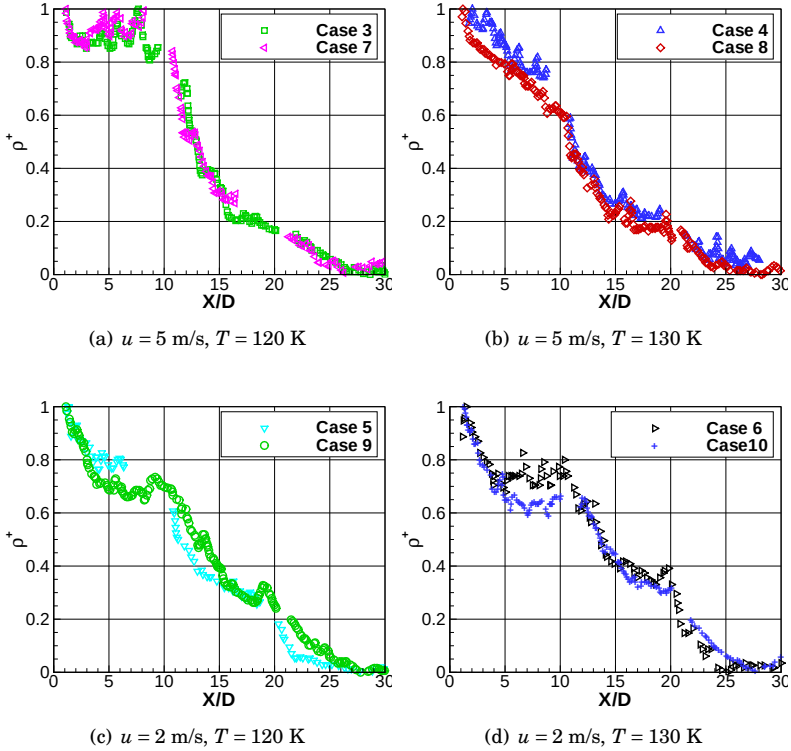

(a) $u = 5$ m/s, $T = 120$ K

(b) $u = 5$ m/s, $T = 130$ K

(c) $u = 2$ m/s, $T = 120$ K

(d) $u = 2$ m/s, $T = 130$ K

Figure 6.7: Nondimensionalized axial density distributions.

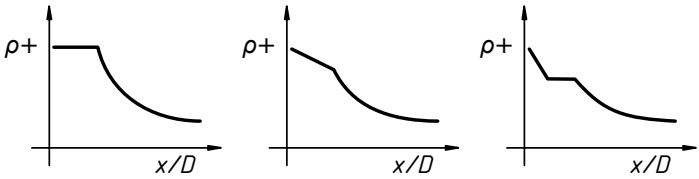

(a) Dense core (c). (b) Slope (s). (c) Plateau (p).

Figure 6.8: Axial density distribution types.

Classical Mechanical Analysis

Correlations for liquid core lengths have been introduced in Ch. 2.2.2. For injection into stagnant environments, two functional forms of equations were found:

1. $L_C = \text{const}$
2. $L_C = f\left((\rho_l/\rho_g)^{1/2}\right)$

As the question at hand concerns differences in length of the liquid core, version 1. is of no use. Expression 2 requires the evaluation of the respective densities. The procedure is as follows: The density in the chamber can be determined assuming the temperature of 297 K is kept. It is evaluated as $\rho_{c,iG}$ using the ideal gas law and as $\rho_{c,rG}$ using real gas data from the NIST database [94, 151]. With T1, T2a and T2b, three temperatures are known. Additionally using the measured chamber pressure, a density can be determined from the NIST data base for each temperature. Finally, the square root of the density ratio is calculated using the ideal gas density of the chamber. Tab. 6.4 shows the results.

The difference between ideal and real gas density of the chamber is negligible. The density in the injector drops for all cases as they are slowly heated from T1 to T2a. Cases 1, 3, 5, 7, 9, and 11 enter the injector with similar densities exceeding 550 kg/m^3. With rising chamber pressures the chamber density grows, the square root of the density ratio decreases. The results do not clearly single out cases 3 and 7 as exhibiting the most pronounced dense cores: the density ratio with respect to ρ_{T1} and ρ_{T2b} of case 5 actually exceeds that of case 7. No indication for this can be seen in the axial density plots. Merely when T2a is picked as reference do the data predict a longer dense core for cases 3 and 7. However, no indication can be found as to why the dense core would collapse to naught in the other experiments. In fact,

Case	$\rho_{c,iG}$	$\rho_{c,rG}$	ρ_{T1}	ρ_{T2a}	ρ_{T2b}	$\left(\frac{\rho_{T1}}{\rho_c}\right)^{\frac{1}{2}}$	$\left(\frac{\rho_{T2a}}{\rho_c}\right)^{\frac{1}{2}}$	$\left(\frac{\rho_{T2b}}{\rho_c}\right)^{\frac{1}{2}}$	Type
1	44.92	45.13	559.74	281.32	538.81	3.53	2.50	3.46	n/a
2	44.81	45.02	325.31	147.44	212.48	2.69	1.81	2.18	n/a
3	45.04	45.24	554.44	457.82	530.03	3.51	3.19	3.43	c
4	45.15	45.36	252.40	164.37	195.83	2.36	1.91	2.08	s
5	55.59	55.84	573.90	433.27	555.63	3.21	2.79	3.16	p
6	55.59	55.84	458.31	224.71	421.46	2.87	2.01	2.75	p
7	56.83	57.09	575.65	517.89	558.74	3.18	3.02	3.14	c
8	56.72	56.98	456.64	315.07	425.38	2.84	2.36	2.74	s
9	66.36	66.63	587.75	420.94	570.28	2.98	2.52	2.93	p
10	66.70	66.97	498.13	320.80	471.73	2.73	2.19	2.66	p
11	67.84	68.11	581.43	515.08	567.99	2.93	2.76	2.89	n/a
12	67.61	67.88	489.44	420.92	469.35	2.69	2.50	2.63	n/a

Table 6.4: Densities and density ratios for measured temperatures. All densities in kg/m^3. Data from NIST database [94].

neither entrainment nor mass shedding, both of which rely on the image of a spreading mechanical interaction with the surrounding stream, can explain a decline in density beginning right upon entering the chamber.

Thermodynamic Analysis

An alternative analysis of the transcritical nitrogen dense core is carried out based on the discussion on pseudo-boiling and its influence on jet break-up in Ch. 3.4. Following Bellan [18], the boundary of a supercritical fluid is situated at the position of the maximum density gradient. As shown in Ch. 3.4, this is equivalent to reaching the pseudo-boiling temperature T_{pb}. In mechanical break-up, all interactions take place within the chamber. In thermal break-up, there are two contributions: heat transfer from the surroundings in the chamber and injector wall heat flux prior to injection.

In Ch. 3.3.5, it was shown that in order to heat a fluid isobarically across the pseudo-boiling line (i.e. a dia-Widom process), a substantial amount of energy is needed beyond the mere temperature increase. Thus, it can be hypothesized that the more energy is required to reach T_{pb}, the more stable the dense core would be.

In order to heat a stream with the mass flow $\dot{m}$ from a temperature T_{in} to T_{pb}, its enthalpy needs to be raised continuously by

$$\Delta\dot{H}_{\mathrm{bu},T_{\mathrm{in}}} = \dot{m}\left(h(T_{\mathrm{pb}}) - h(T_{\mathrm{in}})\right). \tag{6.2}$$

Tab. 6.5 lists this value for $T_{\mathrm{in}} \in \{\mathrm{T1}, \mathrm{T2a}, \mathrm{T2b}\}$ associated with each case. The pressure dependent pseudo-boiling temperature is shown, as well as the temperature interval T^-, T^+ of the supercritical state transition. The mass flow $\dot{m}$ is calculated from the injection velocity in Tab. 6.2, the injector cross-section, and the density corresponding to T1 and chamber pressure from the NIST database. Finally, the supercritical boiling parameter B_1, a nondimensional heat capacity of vaporization defined in Eq. (3.70), is evaluated.

Comparing the temperatures T1, T2a, and T2b with T_{pb}, it can be seen that cases 3 and 7 initially do not reach the pseudo-boiling line. However, this is not a sufficient condition: case 5 for example is also injected at sub-T_{pb} temperature but does not exhibit a dense core.

Case	T1 in K	T2a in K	T2b in K	T^- in K	T_{pb} in K	T^+ in K	$\Delta\dot{H}_{bu,T1}$ in W	$\Delta\dot{H}_{bu,T2a}$ in W	$\Delta\dot{H}_{bu,T2b}$ in W	$\dot{m}$ in g/s	B_1 -	Type
1	120.40	130.00	122.20	127.12	129.52	134.58	215.71	-35.90	193.06	3.83	3.55	n/a
2	129.40	140.00	131.90	127.11	129.46	134.42	4.38	-202.09	-100.57	3.34	3.61	n/a
3	120.90	126.90	122.90	127.13	129.57	134.73	566.18	310.88	496.09	10.33	3.48	c
4	130.70	137.00	133.30	127.14	129.63	134.89	-90.39	-265.30	-190.34	5.18	3.42	s
5	120.70	131.00	122.60	127.76	134.41	148.83	270.63	103.59	246.35	4.36	1.25	p
6	129.80	140.00	131.50	127.76	134.41	148.83	99.08	-113.30	69.08	3.31	1.25	p
7	120.70	126.20	122.50	127.81	134.93	150.43	616.73	448.72	565.50	9.85	1.15	c
8	130.20	135.70	131.70	127.81	134.89	150.28	249.84	-51.88	183.80	8.51	1.16	s
9	120.70	135.00	122.80	128.16	138.56	162.14	297.00	81.22	271.69	4.47	0.67	p
10	129.90	140.50	131.90	128.17	138.68	162.54	140.71	-34.27	114.23	3.60	0.66	p
11	121.70	128.70	123.30	128.20	139.07	163.87	696.63	474.73	649.57	10.83	0.63	n/a
12	130.80	135.40	132.30	128.19	138.99	163.61	332.89	162.50	281.92	9.12	0.63	n/a

Table 6.5: Thermal analysis of cryogenic injection experiments.

Only a certain amount of heat can be supplied by the apparatus to the injected fluid.[3] Evaluating $\Delta\dot{H}_{\mathrm{bu},T_{\mathrm{in}}}$ is more conclusive. Regardless of the chosen T_{in}, cases 3 and 7 have a substantially higher power demand to reach T_{pb} than the other cases. The mass flow of case 5 compared to cases 3 and 7 is halved, the break-up power is accordingly lower.

B_1 is a measure of how much energy is required to overcome intermolecular attraction in relation to mere heating of the liquid. Thus, in cases 1 to 4 ($p_{\mathrm{c}} \approx 4$ MPa), to heat the fluid through the pseudo-boiling line, 3.5 times more energy is needed to overcome intermolecular attraction than for temperature increase. For cases 9 to 12, two thirds of the liquid heating energy are required additionally.

6.1.4 Conclusion

The majority of measurements did not find a dense core as expected by theory: of the eight cases, a mere two did. An analysis based on a mechanical jet break-up process did not conclusively single out the two dense core cases. This suggests a break-up mode different from the classical view of mechanical jet disintegration. Instead, a thermal analysis shows a correlation between peak required pseudo-boiling power and dense core existence. This supports the hypothesis of an additional thermal jet disintegration mode.

A literature study showed that high fidelity LES computations do not systematically outperform RANS. This might be attributed to the greater number of adjustable parameters of a RANS code which allow for an optimization for a particular application.

It has to be emphasized that *not a single* CFD result in the literature reviewed for this thesis was able to reproduce the non dense core experimental results.

[3] A nondimensional parameter relating required enthalpy difference to supplied heat flow $\Delta\dot{H}_{\mathrm{bu},T_{\mathrm{in}}}/\dot{Q}_{\mathrm{supplied}}$ might be the most suitable way to characterize a process like this. Unfortunately, the heat supplied in the injector is not known, nor are the bulk temperatures and thus enthalpies of the injected fluid.

6.2 Exemplary CFD of Thermal Atomization

6.2.1 Rationale

The hypothesis of a possible thermal jet disintegration mechanism has been introduced in Ch. 2.3, experimental evidence to support this has been discussed in Ch. 6.1. Induced by heat flux inside the injector, this would lead to cryogenic jets which exhibit no constant density core.

The exact thermal conditions of the experiment are unknown. While an extensive numerical parameter study might identify thermal boundary conditions which match experimental findings, this does not necessarily mean that these thermal conditions were actually present in the experiment.

Thus, the reproduction of an experiment is not sought here. Instead, an exemplary computation is carried out on a case related to the Mayer experiments. The question is, whether it is possible in CFD to compute non-dense-core injection, comparable to what Mayer, Branam and coworkers [23, 109] found in experiments, when injector heat flux is accounted for.

6.2.2 Literature

Literature of CFD simulations of Mayer cases 3 and 11 was discussed in the previous chapter. Other authors treating the Mayer experiments all assume adiabatic injectors, i.e. Kim et al. [77], Müller et al. [112], Niedermeier et al. [115], Branam et al. [24], Schmitt et al. [144, 145], Hickey et al. [63], Cutrone et al. [37, 38], Cheng and Farmer [36], Jarczyk et al. [71].

6.2.3 Numerical Setup

The numerical case study [14] is based on Mayer experiment 11, corresponding to the RCM1B test case [24]. Only radial density profiles at few axial locations have been published for this case. The numerical domain has been created to match the geometry of the nitrogen injection experiment, see Fig. 6.9(a). The chamber, including the 90 mm constant area part of the injector, has been modeled as 2D axisymmetric. A Dirichlet boundary condition is used to impose an inflow of constant density and temperature, using top hat profiles. The injector wall is modeled as a no-slip turbulent viscous wall, either adiabatic or isothermal at the reference temperature of 298 K. The faceplate is treated as an adiabatic no-slip wall. Figure 6.9(b) shows the

grid resolution for the injector region. Fluid properties are evaluated using the real gas model described in this thesis, based on the MBWR equation of state evaluated for nitrogen. Turbulence is accounted for using the one equation Spalart-Allmaras [150] model. The low Mach number AUSM+up Riemann solver by Liou [96] is employed.

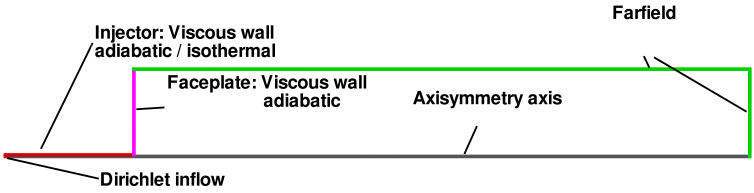

(a) Numerical domain and boundary conditions.

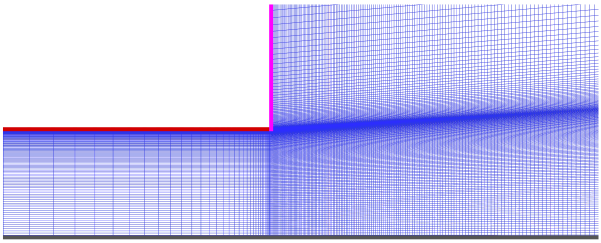

(b) Grid detail of injector region.

Figure 6.9: Numerical setup of thermal break-up computation.

The main deviation from the experiment is the chamber wall boundary being replaced by a farfield boundary. The motivation mainly arose from the unknown state of the chamber at an unknown time of measurement. Figure 6.10 illustrates how the chamber temperature changes during the computation. While this is no time-accurate computation, and hence strictly speaking, intermediate results are unphysical, the overall phenomenon is not: injecting a cryogenic fluid into a chamber at ambient temperature will cool the enclosed fluid. The exact time is essential to determine the chamber state.[4] By providing a farfield boundary instead of a wall, these ambiguities are resolved. The environment is unique and definite. Furthermore, avoiding the recirculation zone at the faceplate enhances convergence significantly.

[4]Unless a steady state has been reached - which has not been ensured in the experiment.

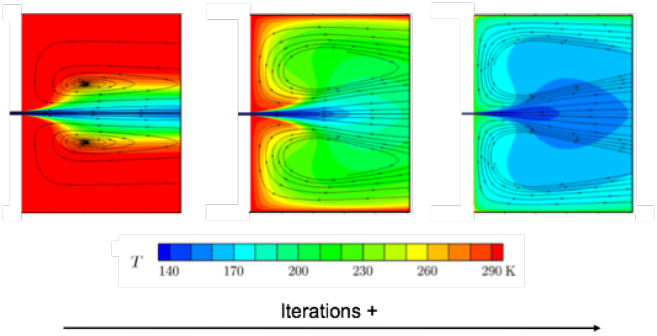

Figure 6.10: Development of chamber temperature with progressing iteration.

Two computations are carried out: the first using the conventional adiabatic injector, the second with an isothermal injector at ambient temperature.

6.2.4 Results

Figure 6.11 shows the resulting density and temperature distributions in the near injector region for an adiabatic injector. A dense core is clearly visible, interaction of the jet with its surroundings begins in the shear layer. As expected, slight variations in temperature around the pseudo-boiling point lead to significant variations in density.

Allowing for heat flux inside the injector changes the injection pattern substantially. Figure 6.12 compares density distributions of the adiabatic and the isothermal injector. In the latter, a thermal boundary layer builds up prior to injection. The density of the jet is diminished, starting from the walls and progressing towards the center. While the adiabatic dense core reaches to $X/D \approx 7$, it ends some five D *before* entering the chamber in the heated case.

Figure 6.13(a) shows axial density profiles of both computations, starting inside the injector at $X/D = -5$. While the adiabatic computation shows the familiar dense core, the isothermal injector shows a sloped density profile right from inside the injector. After the initial core, the isothermal case's density falls off less steeply. The experimental values already start at a density much higher than the imposed inflow density, comparing the other points is

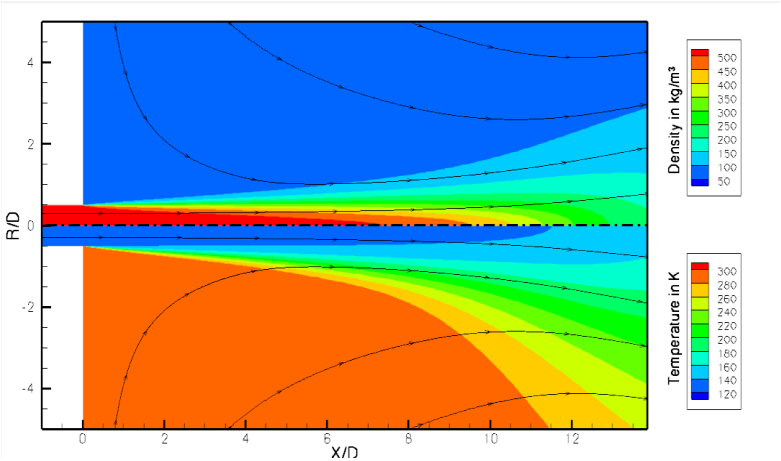

Figure 6.11: Density (top) and temperature (bottom) distributions for conventional adiabatic injector.

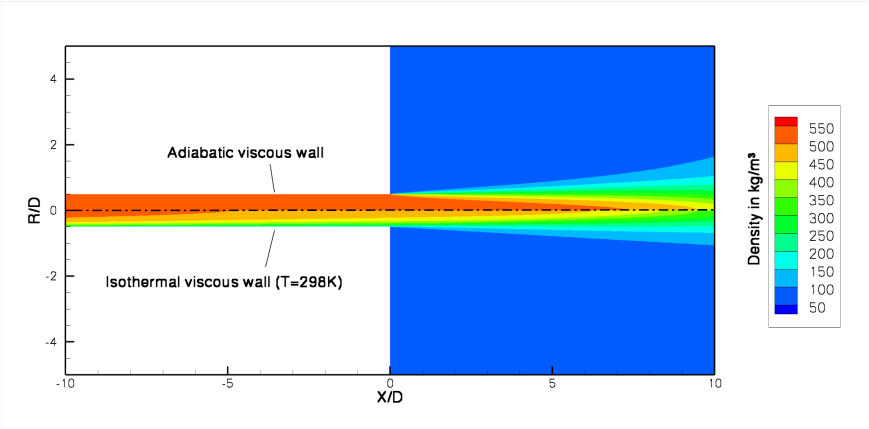

Figure 6.12: Comparison of density distributions for adiabatic (top) and isothermal (bottom) injector wall.

hence of questionable value. The density drop off is however matched rather well, given the simplicity and lack of tuning of the used model.

Radial density distributions for two axial positions are shown in Fig. 6.13(b), namely right at the injector exit $X/D = 0$, and downstream at $X/D = 1.2$. In the adiabatic case, the jet enters with a temperature and density top hat profile.[5] Downstream, the shear layer has smoothed the distribution between $0.35 < R/D < 0.65$. The density profile of the isothermal injector instead is fully developed, the temperature rise reaches all the way to the center. At $X/D = 0$, the density has already dropped from the initial value of 514.0 kg/m^3. As the profile is already fully developed at $X/D = 0$, the shear layer does not affect the flow inside the jet. It does, however, smooth the interface to the surroundings similarly to what is seen in the adiabatic case. Again, the density in the center is too low compared to the experiment, as it is in the surroundings of the chamber. However, the shape of the experimental data clearly resembles the fully developed profile more than a top hat.

6.2.5 Conclusion

Thermal influence on cryogenic jet break-up has successfully been reproduced in a CFD computation using the real gas version of TAU. Accounting for heat transfer in the injector does produce a density profile that resembles experimental data more than the conventional treatment. This has not been found before in the literature reviewed for this thesis.

The calculated density contours do resemble thermal break-up as suggested in Fig. 3.13(c), L_D was found to be smaller than zero in the computed case.

Comparison of numerical and experimental results again emphasizes the ambiguity of the available data. Ultimately, the density and temperature distributions inside the injector are unknown, as is the state inside the chamber. This supports the approach of using a definite, if deviating, numerical setup with farfield boundary conditions. Again: the purpose of this chapter was to provide an exemplary simulation of a thermal break-up process; the reproduction of the experiment was not sought.

All CFD evaluations found in the literature assumed a top hat temperature inflow profile. It could be shown that this is not valid when injector wall heat flux is not negligible.

[5] A slight variation in density can be attributed to viscous dissipation in the boundary layer.

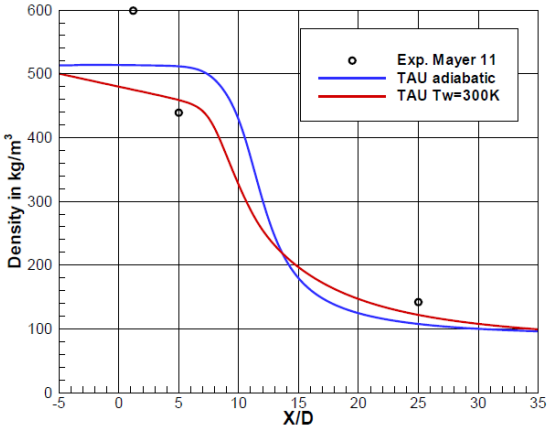

(a) Axial density profiles.

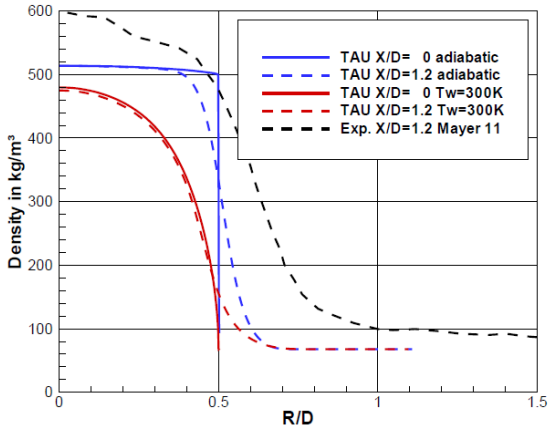

(b) Radial density profiles.

Figure 6.13: Comparison of density profiles for adiabatic and isothermal injector wall with experimental results.

6.3 Reactive Single Injector

6.3.1 Mascotte A60 Testcase

A test case more relevant for rocket engine applications is the Mascotte A60 [55] of the RCM workshop in 2001 [56]. It is operated at nominally 6 MPa, using a single, coaxial injector. Cryogenic oxygen is injected in the center, surrounded by gaseous hydrogen. Tab. 6.6 summarizes the test conditions.

		H_2	O_2
Mass flux	g/s	70	100
Injection velocity	m/s	236	4.35
Temperature	K	287	85
Density	kg/m^3	5.51	1177.8
Viscosity	Pa s	8.67e-6	12.34e-4

Table 6.6: Injection conditions of 2001 RCM3 test case.

Two injector geometries are specified, dependent on the publication, compared in Tab. 6.7. The naming is according to Fig. 1.1. The original 2001 RCM3 geometry [56] is a simplified injector without taper, i.e. $D_0 = D_1$, $\alpha = 0$. Poschner and Pfitzner [131] report that the actual 2001 RCM3 A60 injector is tapered and in fact identical to the one used in the 2006 workshop [164].

Case	D_0 in mm	D_1 in mm	D_2 in mm	D_3 in mm	L_R in mm	δ in mm	α in deg
RCM3 [55]	5.0	5.0	5.6	10.0	0	0.3	0
A60 [131]	3.6	5.0	5.6	10.0	0	0.3	8.0

Table 6.7: Comparison of RCM injector geometry with actual A60 experimental geometry.

The chamber is of square cross section with 100 mm width, closed by a nozzle with a throat diameter of 9.3 mm. Helium is injected as film cooling for the windows in the original facility. Again, the 2001 RCM3 test case chooses to neglect this for simplicity.

6.3.2 Numerical Setup

In this work, the RCM specifications are used as target data in order to allow for comparison with CFD results by other authors. To reduce computational cost, a quasi-2D computational grid has been created, assuming axisymmetry. The grid represents a one degree slice of an equal cross section area cylinder. As the main objective is to test the thermodynamics for mixing and combustion, a hybrid grid has been created with a refined hexahedral region in the mixing zone. Figure 6.14(a) shows the structure of the grid. A is the structured subgrid plus a fine unstructured interface grid, B is the surrounding unstructured grid. Finally, the downstream region C beyond the flame is comprised of a coarser unstructured grid. Figure 6.14(b) shows a detail of the structured grid at the injector exit, including the interface to the structured grid and the surrounding unstructured grid.

(a) Grid structure.

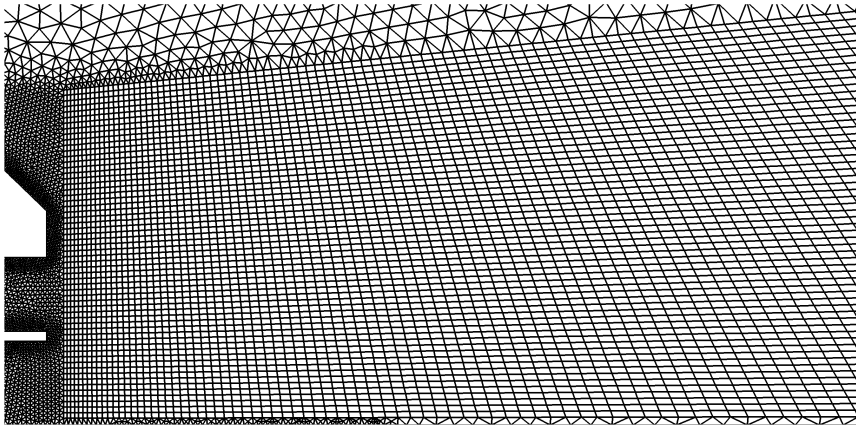

(b) Close up of structured and unstructured grid at injector.

Figure 6.14: Grid for A60 case.

Walls are considered as slip boundaries. The computation is carried out as a RANS simulation, using the one equation Spalart-Allmaras [150] turbu-

lence model. Rossow's MAPS+ [138] Riemann solver is used for its low Mach number behavior and numerical stability. The finite rate combustion mechanism of Jachimowski [69] accounts for 17 reactions and 8 species. To avoid instabilities of the shear layer, the spatial order is reduced to 1.88 when necessary.

6.3.3 Experimental Results

Because of the extreme experimental conditions, not much data could be gathered. One widely referenced result is the contour plot of the spontaneous OH* chemiluminescence shown by Candel et al. [31], originally obtained by Tripathi [159]. The image has been created by Abel-inverting a time averaged result. Juniper et al. [73] superimposed a shadowgraph of the liquid oxygen core, seen in Fig. 6.15(a). Furthermore, the axial coordinate is shown, allowing for comparison with CFD results.

The optical access for the shadowgraph did not capture the end of the LOX core, it extends beyond 13 injector diameters downstream. The regions of OH* emissions enclose the oxygen jet. Their maximum value is concentrated in a very thin region in the shear layer between oxygen and hydrogen. The highest emission level starts approximately one D_1 downstream of the injector exit and extends to $X/D_1 \approx 7$. The reaction zone has widened at that point, the intensity drops off before the shoulder of the flame is reached. The experimental picture is inconclusive with regards to a possible local emission maximum on the axis. While the bottom half might suggest something like this, the top half shows a monotonous reduction in OH* emissivity towards the closing of the flame. Nonetheless, a substantial reduction compared to the shear layer is shown.

The published chamber pressure for the emission plot ranges from 6.0 MPa (RCM specifications [56]) to 6.6 MPa (Candel et al. [31]) and 7.0 MPa (Juniper et al. [73]).

6.3.4 Numerical Results

Chemiluminescence intensity is roughly proportional to the number of molecules involved, hence it needs to be compared to a variable that behaves likewise. Both molar concentration and partial density, i.e. moles and mass per volume, do so. The OH* molar concentration in Fig. 6.15(b) has been

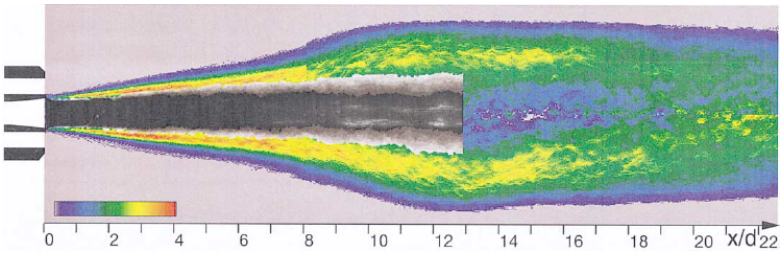

(a) Abel transformed experimental OH* chemiluminescence intensity and liquid core shadowgraph, from Juniper et al. [73].

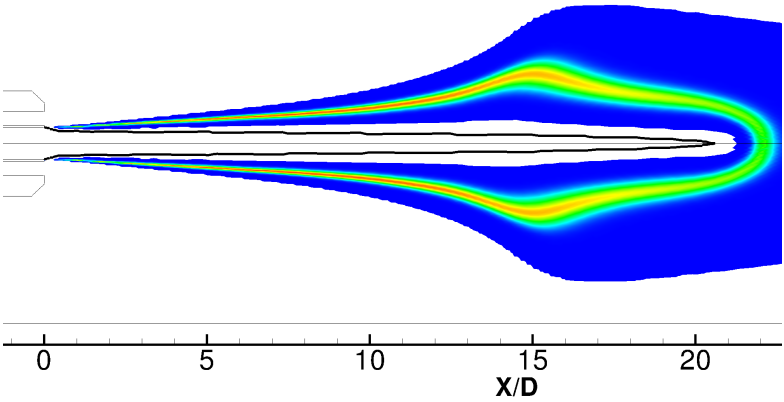

(b) realTAU.

Figure 6.15: Comparison of experimental time-averaged and Abel-inverted OH* emission (top) and numerical OH* molar concentration (bottom).

calculated from OH and temperature distribution following Fiala and Sattelmeyer [46]. The innermost grey line denotes the change of liquid mass fraction to zero once the oxygen stream reaches the critical temperature - it is thus the outline of the liquid core. The maximum OH* concentration is found in the shear layer close to the LOX core. It reduces before the shoulder of the flame and reaches the minimum on the axis. The reaction layer is very thin alongside the LOX core and spreads slightly towards the shoulder and the end of the flame.

In both results, the major OH* occurrence can be seen in a similarly thin reaction zone close to the LOX core, reducing towards the shoulder and the

closing end of the flame. The maximum width of the maximum OH* concentration is situated at 15 X/D_1, the experimental result at around 13 D. With the caveat that only qualitative data are available, agreement is very good. Full quantitative contour plots of temperature, OH* mass fraction, and OH* molar concentration are shown in Fig. 3 in App. 5.

The chamber pressure is determined to be 6.4 MPa.

Prior experience showed that liquid core break-up could be provoked by a sudden change in grid resolution. The structured sublayer in the grid was thus designed to completely enclose the flame, as plotted in Fig. 6.16(a). The close-up in Fig. 6.16(b) furthermore demonstrates the very thin flame front, as resolved by real gas TAU.

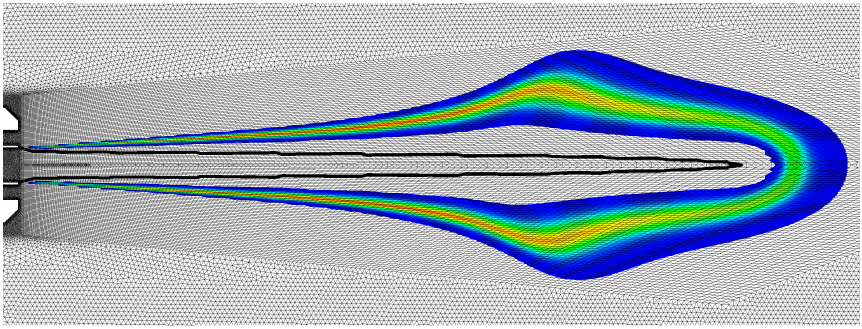

(a) Full flame.

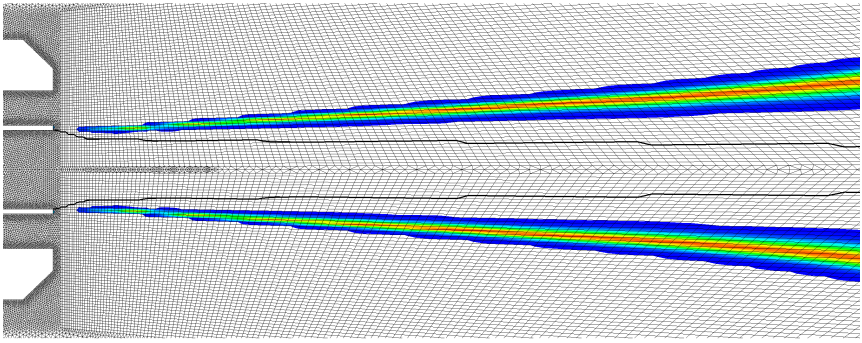

(b) Close-up of shear layer.

Figure 6.16: OH* molar concentration in grid.

A second set of data, the central axial distribution of temperature, has been

published by Poschner and Pfitzner [131], as provided by Vingert. Figure 6.17 compares experimental and numerical results. The maximal temperature as well as its position is very well matched. However, it seems unlikely that the data actually stems from the centerline: the initial measurements of $T \approx 350$ K are clearly too high for the LOX core.

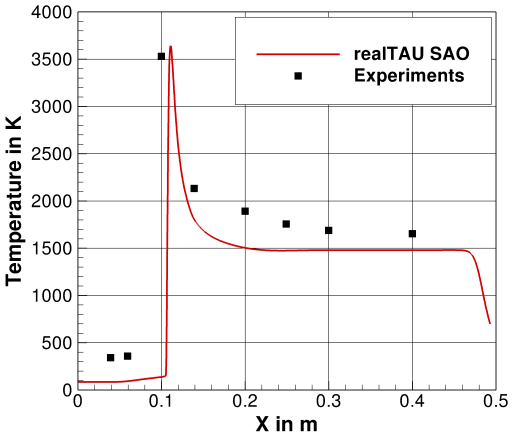

Figure 6.17: Temperature distribution along central axis (Poschner and Pfitzner [131]), comparison of experiment and real gas TAU.

6.3.5 Comparison with other CFD Codes

A comparison with other modeler's results is shown in Figs. 6.18 and 6.19. Details on the used codes are summarized in Tab. 5.2. Fig. 6.18 shows the temperature distribution, again compared to the reference OH* image for lack of other data. Images are scaled and cropped to align with the reference picture. With $D_1 = 0.005$ m, a X coordinate of 0.1 corresponds to $X/D_1 = 20$. Axes are kept where available. While there is some variation, results overall resemble each other. The results of Poschner and Cutrone exhibit maxima at the shoulder and at the axis where the flame closes. The position of the shoulder sees the biggest variation. Poschner's results Fig. 6.18(d) show the influence of the variation of $C_{\varepsilon 1}$ coefficient in the $k-\varepsilon$ turbulence model. The top picture represents the standard coefficients. Enhanced turbulent mixing leads to lower maximal temperatures and wider reaction zones. Furthermore, the LOX core is consumed more rapidly, the flame is shorter.

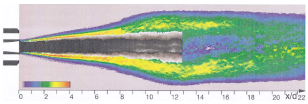

(a) OH* from experiment, Juniper et al. [73].

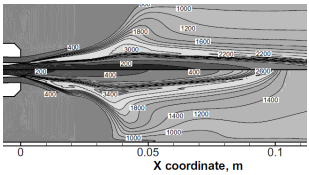

(b) Cutrone et al. [38].

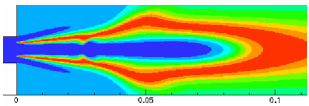

(c) Cheng and Farmer [36].

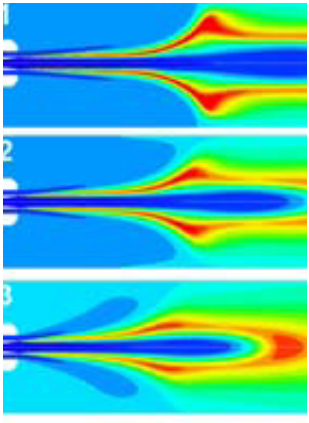

(d) Poschner and Pfitzner [131].

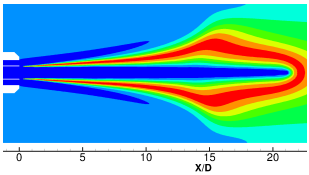

(e) Real gas TAU.

Figure 6.18: Qualitative comparison of temperature distribution from different CFD codes with experimentally determined flame shape. Same scale.

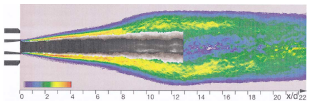

(a) OH* from experiment, Juniper et al. [73].

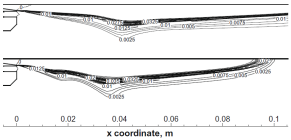

(b) Cutrone et al. [38]

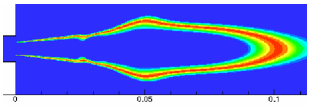

(c) Cheng and Farmer [36].

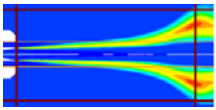

(d) Poschner and Pfitzner [131].

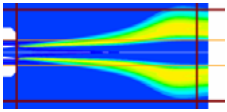

(e) Poschner and Pfitzner [131].

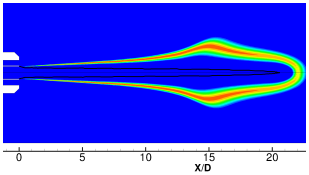

(f) Real gas TAU.

Figure 6.19: Qualitative comparison of OH mass fraction distribution from different CFD codes with experimentally determined flame shape. Same scale.

The second set of results, Fig. 6.19, shows OH mass fractions which is often found in the literature. As discussed above, the mass fraction does not necessarily correspond to emission intensity. Furthermore, OH is shown instead of OH*. The results of Cutrone and Cheng show a local maximum at the flame tip and at the shoulder which is not seen in the experiment. The enhanced mixing in Poschner's lower figure leads to an overall shorter flame which is closer to the experimental result. However, the thin reaction zone in the shear layer is smeared out wide, contrary to experimental results.

6.3.6 A Posteriori Assessment of MFM Assumptions

Now that the case of a coaxial injector with a real-gas mixture has been computed, one can evaluate whether the initial assumptions have been met a posteriori. In Ch. 5.4.1 it is has been discussed that, while oxygen is injected as a real gas, there is evidence in the literature that mixing only occurs under ideal gas conditions. I.e., the transition from real gas behavior to ideal gas behavior takes place inside a pure oxygen shell.

The real gas factor Z, Eq. (3.4), is a measure of deviation from ideal gas behavior. Thus, all mixing, i.e. presence of different species in the same computational cell, should ideally occur only in regions where $Z = 1$.

Figure 6.20 shows a contour plot of oxygen mole fraction along with the $Z = 0.999$ isoline. It turns out the initial assumption is actually rather well met. Merely in the region behind the LOX post and the flame tip is the O_2 mole fraction mildly reduced. Hence, in the investigated case, mixing does essentially occur only in ideal gases, the model is shown to be applicable.

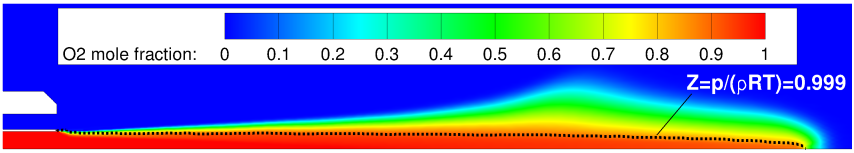

Figure 6.20: Isoline real gas factor $Z = 0.999$ (dotted line) and color contours of oxygen mole fraction.

6.3.7 Conclusion

The real gas TAU results are very promising, despite having used only baseline models. Characteristic features of the experimental flame could be reproduced which have not been shown by other researchers. This includes features such as maximum OH* concentration in the shear layer, no maximum at shoulder and flame tip. The axial temperature profile matches the experimental data very well. As Poschner and Pfitzner [131, 132] demonstrated, better accuracy can be expected from finding suitable values for the turbulent Prandtl number and the turbulence models in the future.

7 Summary and Conclusion

Three main tasks were identified for this thesis, namely

1. develop a real gas mixture model for the DLR TAU code,
2. investigate the thermodynamic process of transcritical injection,
3. analyze the density anomaly in Mayer's injection experiments.

7.1 Real Gas Thermodynamics and Mixture Model

A new real gas thermodynamics model has been developed and implemented into the DLR TAU code. By computing the equation of state (EOS) in a preprocessing step and storing the results in a library, accuracy and efficiency can be decoupled. This allows to use high fidelity EOS which are typically avoided by most modelers for their high computational cost. Liquid, gaseous, supercritical, and multiphase mixture states are then treated in a numerically robust and efficient manner. The developed model includes phase changes; vaporization test cases have been used for validation. A new multi-fluid-mixing (MFM) model had to be developed to solve a dedicated EOS for each species instead of a single mixture EOS as is state-of-the-art. The model has successfully been applied to the canonical A60 Mascotte experiment, a single injector LOX/GH2 case operated at supercritical pressure. The thin reaction zone with a maximum of OH* in the shear layer has been reproduced. A local maximum at the shoulder of the flame, often seen in other CFD but not in the experiment, does not occur.

7.2 Supercritical State Transition and Injection

A thorough literature review is presented that compiles the distributed state of knowledge of supercritical fluid properties into a concise picture: Recent research shows that the supercritical state space is not homogeneous, but splits into a gas-like and a liquid-like region, divided by an extension of the coexistence line. This demarcation is called Widom- or pseudo-boiling-line

in the literature, and can be characterized as the set of supercritical states exhibiting a maximum in the specific heat capacity. In this thesis, a new equation for this line is introduced, which allows to easily assess the state of the fluid at hand. The equation is more accurate than previous equations and does not require fitted parameters. A first quantitative theory of pseudo-boiling has been developed in this thesis: In analogy to subcritical vaporization, it is considered to be a steep transition from a liquid-like to a gas-like fluid, taking place across the Widom- or pseudo-boiling-line. It is shown that for reduced pressures $p_r < 3$, significant excess enthalpy is required in addition to heating, to pass through this line. This is interpreted here as a resemblance to the subcritical latent heat of vaporization. Thus, the critical temperature seizes to be a relevant transition parameter at supercritical pressures and is instead replaced by the pseudo-boiling temperature.

These concepts were than applied to the problem of injection, particularly to determining a liquid core length. Lacking a distinct surface, the extents of a supercritical jet are typically defined somewhat arbitrarily in terms of process values, e.g. the point where the density has dropped to half its injection value. Here, an alternative definition is used, based on the thermodynamic state. Analogous to the vapor pressure curve determining the coexistence between liquid jet and surroundings, the pseudo-boiling-line can be used as a criterion that distinguishes the liquid-like dense core from gas-like surroundings. This point of view in turn implies that heat addition may affect the supercritical dense core length - and this may take place inside the injector, prior to actual injection. This thermal break-up is essentially a way to achieve jet disintegration, additionally to the classical mechanical means. It is found that for a given injection temperature the enthalpy needed to reach the pseudo-boiling point increases with pressure, but for reduced pressures $p_r > 3$ the pseudo-boiling effect will be negligible: The transition between liquid-like and gas-like density becomes nearly linear with respect to temperature.

For the numericist: Thermal boundary layers need to be accounted for in cases where heat flux in the injector cannot be neglected.

For the experimenter: Cryogenic injection is extremely sensitive to temperature variation. Thus a thermally controlled injection will provide disambiguous results. Alternatively, the thermal conditions and heat flux in the injector need to be known in order to allow for a quantitative analysis.

7.3 Axial Density in Transcritical Injection

A review of Mayer's and Branam's injection experiments has been carried out. Three distinctly different axial density distributions can be identified; only two of eight cases show a constant density core as expected by classical mechanical break-up theory and CFD results. The majority of distributions is found to show a decline in density right upon entering the chamber. This difference in core length is not predicted by classical correlations. A thermodynamic analysis, based on the pseudo-boiling concept introduced in this thesis, successfully singles out the dense core cases. Heat flux in the injector is shown to be very likely. All this supports the notion of a thermal break-up mechanism captured in the experiments.

A successful proof of concept computation of thermal break-up in cryogenic injection has been carried out, accounting for injector heat flux. A sloped density distribution similar to what was seen in the experiments could be reproduced for the first time with CFD.

Thus, it appears reasonable to interpret the observed density distributions as follows: Heat flux in the injector led to a preheating of the cryogenic stream. In the majority of the cases, this caused a thermal boundary layer sufficiently thick to reduce the bulk density even before entering the chamber. In the two constant density core cases the supplied heat was not sufficient to cause a thermal break-up, a classical mechanical break-up occurred.

Appendix

1 Modified Benedict-Webb-Rubin Equation

The Modified Benedict-Webb-Rubin equation of state by Younglove [176] is a multiparameter EOS, explicit in pressure. It can be written

$$p\left(\rho,T\right)=\sum_{n=1}^{9}\rho^{n}F_{n-1}+e^{-\delta^{2}}\sum_{n=10}^{15}\rho^{2n-17}F_{n-1}. \tag{1}$$

The functions F_n depend on the temperature, density, and a set of coefficients fit for a particular species. Calvo [28] gives expressions for the derivatives and integrals required to determine real gas thermodynamic state variables. They are repeated here for completeness. The functions and their temperature derivatives are given in Tab. 1. The coefficients G_i for nitrogen and oxygen are compiled in Tab. 2.

In order to calculate values for specific enthalpy, specific internal energy, specific heats, specific entropy, and speed of sound, Eqs. (3.31) - (3.36), certain derivatives and integrals with respect to the EOS need to be evaluated. The partial differential $(\partial p/\partial T)_\rho$ is required to calculate specific isobaric heat capacity c_p, specific enthalpy h, and specific entropy s from their respective Eqs. (3.34), (3.31), and (3.35).

$$\left(\frac{\partial p}{\partial T}\right)_{\rho}=\sum_{n=1}^{9}\rho^{n}\frac{\partial F_{n-1}}{\partial T}+e^{-\delta^{2}}\sum_{n=10}^{15}\rho^{2n-17}\frac{\partial F_{n-1}}{\partial T}. \tag{2}$$

The specific isochoric heat capacity c_v Eq. (3.33) requires

$$\left(\frac{\partial^{2}p}{\partial T^{2}}\right)_{\rho}=\sum_{n=1}^{9}\rho^{n}\frac{\partial^{2}F_{n-1}}{\partial T^{2}}+e^{-\delta^{2}}\sum_{n=10}^{15}\rho^{2n-17}\frac{\partial^{2}F_{n-1}}{\partial T^{2}}. \tag{3}$$

In the real gas equations of the speed of sound c Eq. (3.36) and the specific isobaric heat capacity c_p Eq. (3.34) the partial differential

$$\left(\frac{\partial p}{\partial\rho}\right)_{T}=\sum_{n=1}^{9}n\rho^{n-1}F_{n-1}+e^{-\delta^{2}}\sum_{n=10}^{15}\rho^{2n-18}F_{n-1}\left[2g\rho^{2}+(2n-17)\right] \tag{4}$$

needs to be evaluated.

Similarly, certain integrals need to be solved. The integral I_1 appears in Eq. (3.31) for the specific enthalpy as

$$I_1 = \int_0^{\rho} \left[\frac{p}{\rho^2} - \frac{T}{\rho^2} \left(\frac{\partial p}{\partial T} \right)_{\rho} \right]_T \mathrm{d}\rho. \tag{5}$$

This can be rewritten in terms of the functions F_n of the MBWR EOS,

$$\begin{aligned} I_1 \quad = \quad & \int_0^{\rho} \left[\sum_{n=1}^{9} \rho^{n-2} F_{n-1} + e^{-\delta^2} \sum_{n=10}^{15} \rho^{2n-19} F_{n-1} \right. \\ & \left. -T \sum_{n=1}^{9} \rho^{n-2} \frac{\partial F_{n-1}}{\partial T} - T e^{-\delta^2} \sum_{n=10}^{15} \rho^{2n-19} \frac{\partial F_{n-1}}{\partial T} \right] \mathrm{d}\rho. \end{aligned} \tag{6}$$

The terms with $n = 1$ are equal, i.e.

$$\frac{F_0}{\rho} - \frac{T}{\rho} \frac{\partial F_0}{\partial T} = 0, \tag{7}$$

then

$$\begin{aligned} I_1 \quad = \quad & \int_0^{\rho} \left[\sum_{n=2}^{9} \rho^{n-2} \left(F_{n-1} - T \frac{\partial F_{n-1}}{\partial T} \right) \right. \\ & \left. + e^{-\delta^2} \sum_{n=10}^{15} \rho^{2n-19} \left(F_{n-1} - T - T \frac{\partial F_{n-1}}{\partial T} \right) \right] \mathrm{d}\rho \end{aligned} \tag{8}$$

It is convenient to define a variable g, which appears in the exponential terms of the equations

$$e^{-\delta^2} = e^{\left(-\frac{\rho}{\rho_c}\right)^2} = e^{-g\rho^2}. \tag{9}$$

The integral can be expressed in compact form by integrating the exponential part of the integral term by term as:

$$I_1 \quad = \quad \left[\sum_{n=2}^{9} \frac{\rho^{n-1}}{n-1} \left(F_{n-1} - T \frac{\partial F_{n-1}}{\partial T} \right) \right. \tag{10}$$

$$\left. - e^{-\delta^2} \sum_{n=10}^{15} \left(F_{n-1} - T \frac{\partial F_{n-1}}{\partial T} \right) \frac{1}{2g^{n-9}} \sum_{m=0}^{n-9} \frac{(n-10)!}{m!} \rho^{2m} g^m \right]_0^{\rho} \tag{11}$$

The inner energy can be calculated from specific enthalpy, pressure and density using Eq. (3.32). The expression for the specific heat capacity at constant volume contains the integral

$$I_2 = \int_0^\rho \left[\frac{1}{\rho^2} \left(\frac{\partial^2 p}{\partial T^2} \right)_\rho \right]_T \mathrm{d}\rho. \tag{12}$$

Using Eq. (3), I_2 can be solved analogous to I_1,

$$\begin{aligned} I_2 \quad = \quad & \left[\sum_{n=2}^{9} \frac{\rho^{n-1}}{n-1} \frac{\partial^2 F_{n-1}}{\partial T^2} \right. \\ & \left. -e^{-\delta^2} \sum_{n=10}^{15} \frac{\partial^2 F_{n-1}}{\partial T^2} \frac{1}{2g^{n-9}} \sum_{m=0}^{n-9} \frac{(n-10)!}{m!} \rho^{2m} g^m \right]_0^\rho . \end{aligned} \tag{13}$$

The heat capacity at constant pressure, Eq. (3.34), is calculated from Eqs. (2), (4), and (13). The speed of sound, Eq. (3.36), is calculated using the isentropic exponent

$$\gamma(\rho, T) = \frac{c_p(\rho, T)}{c_v(\rho, T)} \tag{14}$$

and the derivative of the pressure with respect to the density, Eq. (4). The expression furthermore contains the integral

$$I_3 = \int_0^\rho \frac{1}{\rho^2} \left[\left(\frac{\partial p}{\partial T} \right)_\rho - R\rho \right]_T \mathrm{d}\rho. \tag{15}$$

It can be rewritten using

$$\frac{1}{\rho^2} \frac{\partial p}{\partial T}(0) - \frac{R}{\rho} = 0 \tag{16}$$

as

$$\begin{aligned} I_3 \quad = \quad & -\sum_{n=2}^{9} \frac{\rho^{n-1}}{n-1} \frac{\partial F_{n-1}}{\partial T} \\ & +e^{-\delta^2} \sum_{n=10}^{15} \frac{\partial F_{n-1}}{\partial T} \frac{1}{2g^{n-9}} \sum_{m=0}^{n-9} \frac{(n-10)!}{m!} \rho^{2m} g^m . \end{aligned} \tag{17}$$

Index	F_n	$\partial F_n/\partial T$	$\partial^2 F_n/\partial T^2$
0	RT	R	0
1	$G_1T+G_2T^{0.5}+G_3+G_4/T+G_5/T^2$	$G_1+G_2/2T^{0.5}-G_4/T^2-2G_5/T^3$	$G_2/4T^{1.5}+2G_4/T^3+6G_5/T^4$
2	$G_6T+G_7+G_8/T+G_9/T^2$	$G_6-G_8/T^2-2G_9/T^3$	$2G_8/T^3+6G_9/T^4$
3	$G_{10}T+G_{11}+G_{12}/T$	$G_{10}T-G_{12}/T^2$	$2G_{12}/T^3$
4	G_{13}	0	0
5	$G_{14}/T+G_{15}/T^2$	$-G_{14}/T^2-2G_{15}/T^3$	$2G_{14}/T^3+6G_{15}/T^4$
6	G_{16}/T	$-G_{16}/T^2$	$2G_{16}/T^3$
7	$G_{17}/T+G_{18}/T^2$	$-G_{17}/T^2-2G_{18}/T^3$	$2G_{17}/T^3+6G_{18}/T^4$
8	G_{19}/T^2	$-2G_{19}/T^3$	$6G_{19}/T^4$
9	$G_{20}/T^2+G_{21}/T^3$	$-2G_{20}/T^3-3G_{21}/T^4$	$6G_{20}/T^4+12G_{21}/T^5$
10	$G_{22}/T^2+G_{23}/T^4$	$-2G_{22}/T^3-4G_{23}/T^5$	$6G_{22}/T^3+20G_{23}/T^6$
11	$G_{24}/T^2+G_{25}/T^3$	$-2G_{24}/T^3-3G_{25}/T^4$	$6G_{24}/T^4+12G_{25}/T^5$
12	$G_{26}/T^2+G_{27}/T^4$	$-2G_{26}/T^3-4G_{29}/T^5$	$6G_{26}/T^4+20G_{27}/T^6$
13	$G_{28}/T^2+G_{29}/T^3$	$-2G_{28}/T^3-3G_{29}/T^4$	$6G_{28}/T^4+12G_{29}/T^5$
14	$G_{30}/T^2+G_{31}/T^3+G_{32}/T^4$	$-2G_{30}/T^3-3G_{31}/T^4-4G_{32}/T^5$	$6G_{30}/T^4+12G_{31}/T^5+20G_{32}/T^6$

Table 1: Functions and derivatives of the Modified Benedict-Webb-Rubin equation of state.

Index	N_2	O_2
1	1.38029747465691e-04	-4.365859650e-05
2	1.08450650134880e-02	2.005820677e-02
3	-0.247132406436209	-0.4197909916
4	3.45525798080709e+00	1.878215317e+01
5	-4.27970769066595e+02	-1.287473398e+03
6	1.06491156699760e-05	1.556745888e-06
7	-1.14086707973499e-03	1.343639359e-04
8	1.44490249728747e-05	-0.2228415518
9	1.87145756755327e+03	4.767792275e+02
10	8.21887688683079e-09	4.790846641e-08
11	2.36099049334759e-04	2.462611107e-04
12	-5.14480308120135e-02	-1.921891680e-02
13	4.91454501366803e-06	-6.978320847e-07
14	-1.15162716239893e-04	-6.214145909e-05
15	-7.16803724664983e-02	-1.860852567e-02
16	7.61666761949981e-06	2.609791417e-06
17	-1.13093006621295e-07	-2.447611408e-08
18	3.73683116683089e-05	1.457743352e-05
19	-2.03985150758086e-07	-1.726492873e-07
20	-1.71966200898966e+03	-2.384892520e+02
21	-1.21305519974777e+04	-2.301807796e+04
22	-9.88139914142789e+00	-2.790303526e+00
23	5.61988689351085e+03	9.400577575e+03
24	-1.82304396411845e-02	-4.169449627e-03
25	-0.259982649847705	0.2008497853
26	-4.19189342315742e-05	-1.256076520e-05
27	-2.59640667052023e-02	-6.406362964e-02
28	-1.25868320192119e-08	-2.475580168e-09
29	1.04928659940046e-06	1.346309703e-06
30	-5.45836930515201e-11	-1.161502470e-11
31	-7.67451167059717e-10	-1.034699798e-09
32	5.93123287099439e-09	2.365936964e-08
γ	-0.0056	-0.0056

Table 2: Coefficients G_i for the MBWR EOS, Eq. (1) and Tab. 1.

Index	N_2	O_2
1	5.1113192094	7.568956
2	0.6482667539	5.004836
3	-0.15108730916	-2.13746
4	0.0	0.0
5	0.74028493342	3.454481
6	1.5	1.514
T_{tr}	63.15	54.359
T_{cr}	126.26	154.581

Table 3: Coefficients V_i for vapor pressure fit Eqs. (5.16) and (5.17).

Index	N_2	O_2
1	-1.58453465507e+01	5.81394753076e+01
2	4.19136911423e-02	-4.90241196133e-02
3	-1.01965371660e+00	1.68328893252e+00
4	1.34763743799e+01	-3.25161223398e+01
5	-1.09930399087e+02	5.50300989872e+02
6	9.25518835497e+01	-5.10968506115e+02
7	-9.56233831320e+01	3.15091559049e+02
8	1.00104366710e+02	-2.32566659258e+01
9	-7.01857937398e+01	-4.88425479359e+01
10	9.00076998647e+00	-1.50624217523e+02
11	2.86981120347e+01	2.80441603851e+02
12	-2.16767601780e+01	-1.76693896861e+02
13	4.96558226471e+00	4.03247747449e+01
14	2.18307928477e+01	2.52198688365e+00
15	-0.126493309807	-1.36098316472e-02
16	2.41544188633e+00	2.82316159403e-01
17	-2.45256871794e+01	-2.86645905341e+00
18	9.35925207124e+01	6.17024212284e+00
19	-3.60938251632e+01	-8.10220795462e-01
20	7.57453271989e+00	-2.79601068969e-01

Table 4: Coefficients A_i for density fits Eqs. (5.18), (5.19), (5.21), (5.22).

2 Transport Coefficients

Parameters for Viscosity Equation

Index	b_i
0	0.431
1	-0.4623
2	0.08406
3	0.005341
4	-0.00331

Table 5: Coefficients b_i for dilute viscosity, Eq. (5.26).

Parameter	N_2	O_2
M in g/mol	28.01348	31.9988
ϵ/k in K	98.94	118.5
σ in nm	0.3656	0.3428
ξ_0 in nm	0.17	0.24
Γ	0.055	0.055
q_D in nm	0.40	0.51

Table 6: Additional parameters of dilute viscosity, Eqs. (5.26) and (5.27).

Parameters for Thermal Conductivity Equations

k	1.38065	$\times 10^{-23}$ J/K
R_0	1.01	
ν	0.63	
β	1.2415	

Table 7: Thermal conductivity critical enhancement parameters, Eqs. (5.33) - (5.37).

Species	i	N_i	t_i	d_i	l_i
N_2	1	10.72	0.1	2	0
	2	0.03989	0.25	10	1
	3	0.001208	3.2	12	1
	4	-7.402	0.9	2	2
	5	4.620	0.3	1	3
O_2	1	17.67	0.05	1	0
	2	0.4042	0.0	5	0
	3	0.0001077	2.10	12	0
	4	0.3510	0.0	8	1
	5	-13.67	0.5	1	7

Table 8: Parameters of real gas viscosity contribution, Eq. (5.28).

Species	i	N_i	t_i	d_i	l_i
N_2	1	1.511	0	0	0
	2	2.117	-1.0	0	0
	3	-3.332	-0.7	0	0
	4	8.862	0.0	1	0
	5	31.11	0.03	2	0
	6	-73.13	0.2	3	1
	7	20.03	0.8	4	2
	8	-0.7096	0.6	8	2
	9	0.2672	1.9	10	2
O_2	1	1.036	0	0	0
	2	6.283	-0.9	0	0
	3	-4.262	-0.6	0	0
	4	15.31	0.0	1	0
	5	8.898	0.0	3	0
	6	-0.7336	0.3	4	2
	7	6.728	4.3	5	2
	8	-4.374	0.5	7	2
	9	-0.4747	1.8	10	2

Table 9: Parameters of thermal conductivity equations, Eqs. (5.31) and (5.32).

3 Thermodynamics Algorithm Schematics

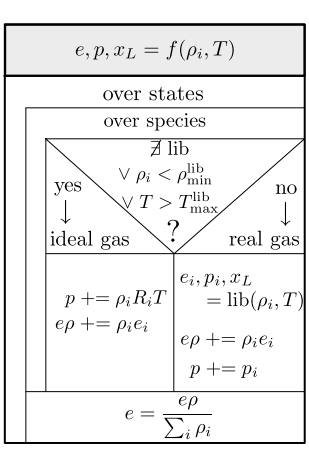

(a) Main function $f(\rho, T)$.

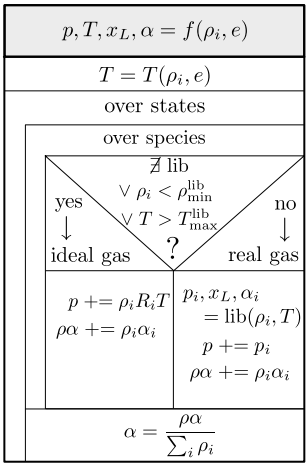

(b) Main function $f(\rho, e)$.

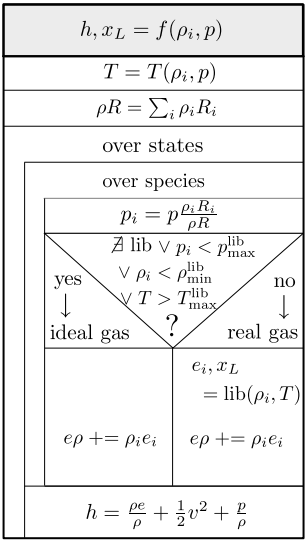

(c) Main function $f(\rho, p)$.

Figure 1: Thermodynamics main functions.

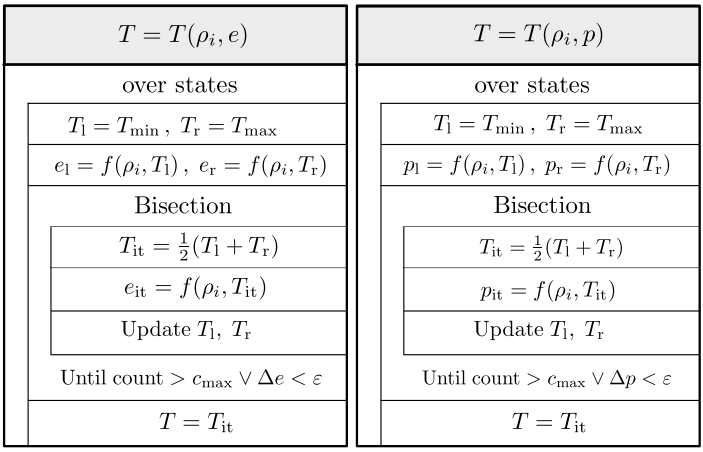

(a) Supplemental: $T(\rho, e)$. (b) Supplemental: $T(\rho, p)$.

Figure 2: Thermodynamics supplemental functions.

4 Reaction Mechanism of H_2 - O_2 Combustion

r	Reaction	a_r^f in m^3/mol, m^9/mol^2	b_r^f	c_r^f in K
1	$H_2 + O_2 \leftrightarrow HO_2 + H$	1.0201×10^8	0	18000
2	$H + O_2 \leftrightarrow OH + O$	2.6201×10^8	0	8400
3	$O + H_2 \leftrightarrow OH + H$	1.8201×10^4	1	4450
4	$OH + H_2 \leftrightarrow H_2O + H$	2.2201×10^7	0	2580
5	$OH + OH \leftrightarrow H_2O + O$	6.3201×10^6	0	545
6	$H + OH + M \leftrightarrow H_2O + M$	2.2201×10^{10}	-2	0
7	$H + H + M \leftrightarrow H_2 + M$	12.8201×10^5	-1	0
8	$H + O + M \leftrightarrow OH + M$	6.0201×10^4	-0.6	0
9	$H + O_2 + M \leftrightarrow HO_2 + M$	4.2201×10^3	0	-500
10	$HO_2 + H \leftrightarrow OH + OH$	1.4201×10^8	0	540
11	$HO_2 + H \leftrightarrow H_2O + O$	1.0201×10^7	0	540
12	$HO_2 + O \leftrightarrow O_2 + OH$	1.5201×10^7	0	475
13	$HO_2 + OH \leftrightarrow H_2O + O_2$	8.0201×10^6	0	0
14	$HO_2 + HO_2 \leftrightarrow H_2O_2 + O_2$	2.0201×10^6	0	0
15	$H + H_2O_2 \leftrightarrow H2 + HO_2$	1.4201×10^6	0	1800
16	$O + H_2O_2 \leftrightarrow OH + HO_2$	1.4201×10^7	0	3200
17	$OH + H_2O_2 \leftrightarrow H_2O + HO_2$	6.1201×10^6	0	715
18	$H_2O_2 + M \leftrightarrow OH + OH + M$	1.2201×10^{11}	0	22800
19	$O + O + M \leftrightarrow O_2 + M$	6.0201×10^1	0	-900

Table 10: Jachimowski H_2 - O_2 combustion reaction mechanism [69], as reported by Gerlinger [50].

r	H_2	O_2	H	O	OH	H_2O	HO_2	H_2O_2	N_2
6	1	1	1	1	1	6	1	1	1
7	2	1	1	1	1	6	1	1	1
8	1	1	1	1	1	5	1	1	1
9	2	1	1	1	1	16	1	1	1
18	1	1	1	1	1	15	1	1	1

Table 11: Third body efficiencies for reactions 6, 7, 8, 9, 18. All other third body efficiencies are unity [49].

5 Quantitative A60 CFD Results

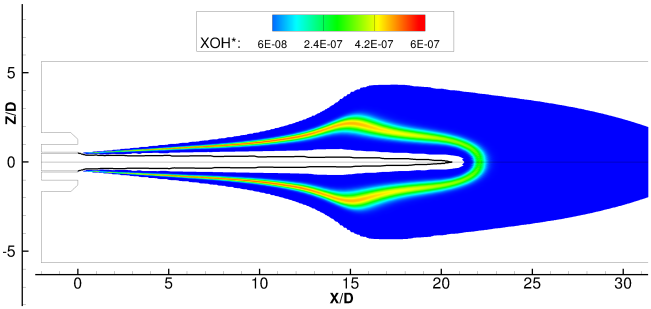

(a) OH* molar concentration.

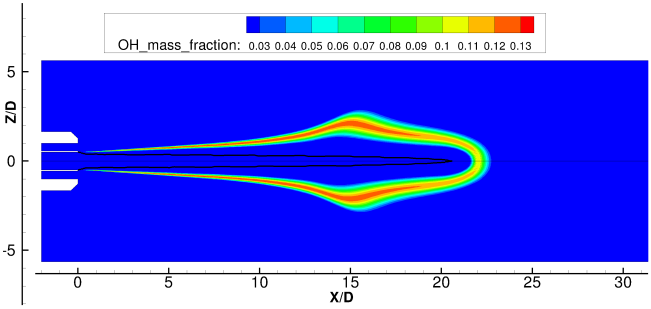

(b) OH mass fraction.

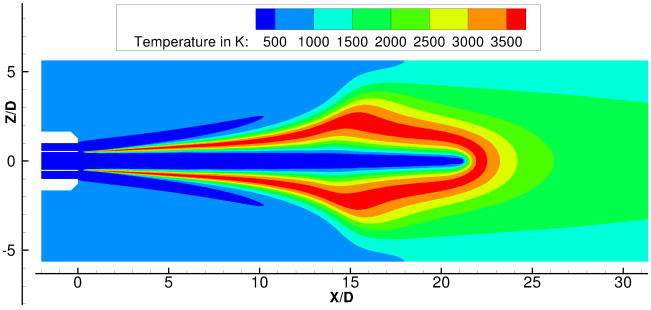

(c) Temperature.

Figure 3: Quantitative A60 results of real gas TAU.

Bibliography

[1] http://cs.astrium.eads.net/sp/launcher-propulsion/rocket-engines/images/vulcain-2-injector-plate.jpg, Retrieved 01.03.2014.

[2] http://cs.astrium.eads.net/sp/launcher-propulsion/rocket-engines/images/vulcain-thrust-chamber-assembly.jpg, Retrieved 01.03.2014.

[3] http://tau.dlr.de, Retrieved 01.03.2014.

[4] J.L.F. Abascal and C. Vega. Widom line and the liquid-liquid critical point for the TIP4P/2005 water model. *The Journal of Chemical Physics*, 133:234502–1 – 234502–8, 2010.

[5] G.N. Abramovich. *The theory of turbulent jets*. MIT Press, Cambridge, 1963.

[6] J.D. Anderson. *Computational Fluid Dynamics*. McGraw-Hill, 1st edition, 1995.

[7] T. Andrews. The Bakerian lecture: On the continuity of the gaseous and liquid states of matter. *Philosophical Transactions of the Royal Society (London)*, (159):575–590, 1869.

[8] H. Ashkenas and F.S. Sherman. Rarefied gas dynamics. volume 2, chapter The structure and utilization of supersonic free jets in low density wind tunnels, pages 84–105. Academic Press, 1966.

[9] P. Atkins and J. de Paula. *Physical Chemistry*. Oxford University Press, 2010.

[10] E. Babinsky and P. E. Sojka. Modeling drop size distributions. *Progress in Energy and Combustion Science*, 28:303–329, 2002.

[11] H.D. Baehr and S. Kabelac. *Thermodynamik: Grundlagen und technische Anwendungen*. Springer, 13th edition, 2009.

[12] D.T. Banuti. Crossing the Widom-line – supercritical pseudo-boiling. *Journal of Supercritical Fluids*, 98:12–16, 2015.

[13] D.T. Banuti and K. Hannemann. Flow control by energy deposition in hypersonic flow - some fundamental considerations. In *Proceedings of the 16th AIAA/DLR/DGLR International Space Planes and Hypersonic Systems and Technologies Conference*, number AIAA-2009-7345, Bremen, Germany, 2009. AIAA/DLR/DGLR.

[14] D.T. Banuti and K. Hannemann. Effect of injector wall heat flux on cryogenic injection. In *Proceedings of the 46th AIAA/ASME/SAE/ASEE Joint Propulsion Conference and Exhibit*, number AIAA-2010-7139, Nashville, USA, 2010. AIAA.

[15] D.T. Banuti and K. Hannemann. Thermodynamic interpretation of cryogenic injection experiments. In *Proceedings of the 47th AIAA/ASME/SAE/ASEE Joint Propulsion Conference and Exhibit*, number AIAA 2011-5620, San Diego, USA, 2011. AIAA.

[16] D.T. Banuti and K. Hannemann. Real gas library in continuous phase propellant injection model for liquid rocket engines. In *Proceedings of the 49th AIAA/ASME/SAE/ASEE Joint Propulsion Conference and Exhibit*, number AIAA 2013-4068, San Jose, USA, 2013.

[17] J.M.M. Barata, I. Gökalp, and A.R.R. Silva. Numerical study of cryogenic jets under supercritical conditions. *Journal of Propulsion and Power*, 19(1):142–147, 2003.

[18] J. Bellan. Supercritical (and subcritical) fluid behavior and modeling: drops, streams and mixing layers, jets and sprays. *Progress in Energy and Combustion Science*, pages 329–366, 2000.

[19] J. Bellan. Theory, modeling and analysis of turbulent supercritical mixing. *Combustion Science and Technology*, 178:253–281, 2006.

[20] M. Benedict, G.B. Webb, and L.C. Rubin. An empirical equation for thermodynamic properties of light hydrocarbons and their mixtures: I. methane, ethane, propane, and n-butane. *Journal of Chemical Physics*, 8(4):334–345, 1940.

[21] F.G. Blottner, M. Johnson, and M. Ellis. Chemically reacting viscous flow program for multi-component gas mixtures. *Sandia Laboratories, Albuquerque*, SC-RR-70-754, 1971.

[22] R. Branam and W. Mayer. Length scales in cryogenic injection at supercritical pressure. *Experiments in Fluids*, 33:422–428, 2002.

[23] R. Branam and W. Mayer. Characterization of cryogenic injection at supercritical pressure. *Journal of Propulsion and Power*, 19(3):342–355, 2003.

[24] R. Branam, J. Telaar, and W. Mayer. Simulation of cryogenic jet injection. In O. Haidn, editor, *Proceedings of the 2nd International Workshop on Rocket Combustion Modeling*, Lampoldshausen, Germany, 2001.

[25] H. Brauer. *Grundlagen der Einphasen- und Mehrphasen-Strömungen*. Sauerländer, 1971.

[26] V.V. Brazhkin, Y.D. Fomin, A.G. Lyapin, V.N. Ryzhov, and E.N. Tsiok. Widom line for the liquid-gas transition in Lennard-Jones system. *The Journal of Physical Chemistry B*, 115:14112–14115, 2011.

[27] Boston University Research Briefs. Water wisdom and Widom. http://www.bu.edu/phpbin/researchbriefs/display.php?id=659, 2003.

[28] J. Bartolome Calvo. *Numerical Simulation of Liquid Rocket Engine Cooling Channels*. PhD thesis, Universitat Politecnica de Catalunya, 2010.

[29] J. Bartolome Calvo and K. Hannemann. Numerical simulation of liquid rocket engine cooling channels. In *Proceedings of the 45th AIAA/ASME/SAE/ASEE Joint Propulsion Conference & Exhibit*, Denver, 2009.

[30] S. Candel, G. Herding, R. Synder, P. Scouflaire, C. Rolon, L. Vingert, M. Habiballah, F. Grisch, M. Péalat, P. Bouchardy, D. Stepowski, A. Cessou, and P. Colin. Experimental investigation of shear coaxial cryogenic jet flames. *Journal of Propulsion and Power*, 14(5):826–834, 1998.

[31] S. Candel, M. Juniper, G. Singla, P. Scouflaire, and C. Rolon. Structures and dynamics of cryogenic flames at supercritical pressure. *Combustion Science and Technology*, 178:161–192, 2006.

[32] M. Chapuis, E. Fedina, C. Fureby, K. Hannemann, S. Karl, and J. Martinez Schramm. A computational study of the hyshot ii combustor performance. *Proceedings of the Combustion Institute*, 34(2):2101–2109, 2013.

[33] B. Chehroudi, D. Talley, and E. Coy. Initial growth rate and visual characteristics of a round jet into sub- and supercritical environment of relevance to rocket, gas turbine, and Diesel engines. In *Proceedings of the 37th Aerospace Sciences Meeting and Exhibit*, Reston, USA, 1999. AIAA.

[34] B. Chehroudi, D. Talley, and E. Coy. Visual characteristics and initial growth rates of round cryogenic jets at subcritical and supercritical pressures. *Physics of Fluids*, 14(2):850–861, 2002.

[35] G.C. Cheng and R. Farmer. Real fluid modeling of multiphase flows in liquid rocket engine combustors. *Journal of Propulsion and Power*, 22(6):1373–1381, 2006.

[36] G.C. Cheng and R.C. Farmer. CFD spray combustion model for liquid rocket engine injector analyses. In *Proceedings of the 40th AIAA Aerospace Sciences Meeting and Exhibit*, number AIAA-2002-785, Reno, USA, 2002. AIAA.

[37] L. Cutrone, P. de Palma, G. Pascazio, and M. Napolitano. A flamelet/progress variable approach for the simulation of turbulent combustion of real gas mixtures. In *Proceedings of the 44th AIAA/ASME/SAE/ASEE Joint Propulsion Conference and Exhibit*, number AIAA 2008-4567, Hartford, USA, 2008. AIAA.

[38] L. Cutrone, P. de Palma, G. Pascazio, and M. Napolitano. A RANS flamelet-progress-variable method for computing reacting flows of real-gas mixtures. *Computers & Fluids*, 39:485–498, 2010.

[39] W. Dahmen and A. Reusken. *Numerik für Ingenieure und Naturwissenschaftler*. Springer, 2nd edition, 2006.

[40] R. Dahms and J.C. Oefelein. Theory and analysis of liquid-oxygen–hydrogen interface dynamics in liquid rockets at supercritical pressures. In *Proceedings of the 49th AIAA/ASME/SAE/ASEE Joint Propulsion Conference and Exhibit*, number AIAA 2013-3716. AIAA, 2013.

[41] J. Eggers. A brief history of drop formation. In P. Alart, O. Maisonneuve, and R.T. Rockafellar, editors, *Nonsmooth Mechanics and Analysis*. Springer, 2006.

[42] J.F. Ely and H.J.M. Hanley. Prediction of transport properties. 1. Viscosity of fluids and mixtures. *Industrial & Engineering Chemistry Fundamentals*, 20:323–332, 1981.

[43] J.F. Ely and H.J.M. Hanley. Prediction of transport properties. 1. Thermal conductivity of pure fluids and mixtures. *Industrial & Engineering Chemistry Fundamentals*, 22:90–97, 1983.

[44] H. Eroglu, N. Chigier, and Z. Farago. Coaxial atomizer liquid intact lengths. *Physics of Fluids*, 3(2):303–308, 1991.

[45] R. Farmer, G. Cheng, and Y.-S. Chen. CFD simulation of liquid rocket engine injectors. In *Proceedings of the 2nd International Workshop on Rocket Combustion Modeling*, 2001.

[46] T. Fiala and T. Sattelmeyer. A posteriori computation of OH* radiation from numerical simulations in rocket combustion chambers. In *Proceedings of the 5th European Conference for Aeronautics and Space Sciences (EUCASS)*, Munich, Germany, 2013.

[47] V. Gautam and A.K. Gupta. Simulation of flow mixing from a cryogenic rocket injector. *Journal of Propulsion and Power*, 23(1):123–130, 2007.

[48] T. Gerhold, M. Galle, O. Friedrich, and J. Evans. Calculation of complex three-dimensional configurations employing the DLR-TAU-code. In *Proceedings of the 35th Aerospace Sciences Meeting and Exhibit*, number AIAA-1997-167, Reno, USA, 1997. AIAA.

[49] P. Gerlinger. An implicit multigrid method for turbulent combustion. *Journal of Computational Physics*, 167:247–276, 2001.

[50] P. Gerlinger. Investigation of an assumed pdf approach for finite rate chemistry. *Combustion Science and Technology*, 175:841–872, 2003.

[51] F. Gorelli, M. Santoro, T. Scopigno, M. Krisch, and G. Ruocco. Liquidlike behavior of supercritical fluids. *Physical Review Letters*, 97:245702–1 – 245702–4, 2006.

[52] J. Görgen and O. Knab. CryoROC - a multi-phase Navier-Stokes solver for advanced rocket thrust chamber design. In *Proceedings of the 4th European Symposium on Aerothermodynamics for Space Applications*, number SP-487, Capua, Italy, 2001. ESA.

[53] F. Grisch, P. Bouchardy, L. Vingert, W. Clauss, M. Oschwald, O.M. Stel'mack, and V.V. Smirnov. CARS measurements at high pressure in cryogenic LOX/GH2 jet flames. In V. Yang, M. Habiballah, J. Hulka, and M. Popp, editors, *Progress in Astronautics and Aeronautics: Liquid Rocket Thrust Chamber: Aspects of Modeling, Analysis, and Design*. AIAA, 2004.

[54] M. Habiballah, M. Orain, F. Grisch, L. Vingert, and P. Gicquel. Experimental studies of high-pressure cryogenic flames on the mascotte facility. *Combustion Science and Technology*, 178:101–128, 2006.

[55] M. Habiballah and S. Zurbach. Test case RCM-3 - Mascotte single injector 60 bar. In O.J. Haidn, editor, *Proceedings of the 2nd International Workshop Rocket Combustion Modeling - Atomization, Combustion and Heat Transfer*, Lampoldshausen, Germany, 2001.

[56] O.J. Haidn, editor. *Proceedings of the 2nd International Workshop Rocket Combustion Modeling - Atomization, Combustion and Heat Transfer*. Lampoldshausen, Germany, 2001.

[57] W.B. Hall. Heat transfer near the critical point. In T.F. Irvine Jr. and J.P. Hartnett, editors, *Advances in Heat Transfer*, volume 7, pages 1–86. Academic Press, 1971.

[58] V. Hannemann. Numerische Simulation von Stoß- Stoß- Wechselwirkungen unter Berücksichtigung von chemischen und thermischen Nichtgleichgewichtseffekten. Technical Report FB 97-07, DLR, 1997.

[59] S. Harrington, R. Zhang, P.H. Poole, F. Sciortino, and H.E. Stanley. Liquid-liquid phase transition: evidence from simulations. *Physical Review Letters*, 78(12):2409–2412, 1997.

[60] D.T. Harrje and F.H. Reardon. Liquid propellant rocket combustion instability. Technical Report SP-194, NASA, 1972.

[61] K. Harstad and J. Bellan. Isolated fluid oxygen drop behavior in fluid hydrogen at rocket chamber pressures. *International Journal of Heat and Mass Transfer*, 41:2426–2449, 1998.

[62] K.G. Harstad, R.S. Miller, and J. Bellan. Efficient high-pressure state equations. *AIChEJournal*, 43(6):1605–1610, 1997.

[63] J.-P. Hickey, P.C. Ma, M. Ihme, and S.S. Thakur. Large eddy simulation of shear coaxial rocket injector: Real fluid effects. In *Proceedings of the 49th AIAA/ASME/SAE/ASEE Joint Propulsion Conference and Exhibit*, number AIAA 2013-4071, San Jose, USA, 2013. AIAA.

[64] J.O. Hirschfelder, C.F. Curtiss, and R.B. Bird. *Molecular Theory of Gases and Liquids*. Wiley, 1954.

[65] A. Hosangadi, C.P. Lee, C. Kannepalli, and S. Arunajatesan. Three-dimensional hybrid RANS/LES simulations of a supercritical liquid nitrogen jet. In *Proceedings of the 44th AIAA/ASME/SAE/ASEE Joint Propulsion Conference & Exhibit*, Hartford, 2008.

[66] M. Ishii and T. Hibiki. *Thermo-Fluid Dynamics of Two-Phase Flow*. Springer, 2006.

[67] B. Ivancic. *Untersuchungen zur Strömung und Verbrennung im Einspritzgebiet von LOX/H2-Raketenbrennkammern*. PhD thesis, University of Stuttgart, 2001.

[68] B. Ivancic, H. Riedmann, M. Frey, O. Knab, S. Karl, and K. Hannemann. Investigation of different modeling approaches for CFD simulation of high pressure rocket combustors. In *Proceedings of the 5th European Conference for Aeronautics and Space Sciences (EUCASS)*, Munich, Germany, 2013.

[69] C.J. Jachimowski. An analytical study of the hydrogen-air reaction mechanism with application to scramjet. Report NASA TP 2791, NASA, 1988.

[70] M.-M. Jarczyk. *Numerische Modellierung von turbulenten Strömungen realer Gasgemische*. PhD thesis, Universität der Bundeswehr München, 2013.

[71] M.-M. Jarczyk and M. Pfitzner. Large eddy simulation of supercritical nitrogen jets. In *Proceedings of the 50th AIAA Aerospace Sciences Meeting including the New Horizons Forum and Aerospace Exposition*, number AIAA 2012-1270, Nashville, USA, 2012. AIAA.

[72] S. Jay, F. Lacas, and S. Candel. Combined surface density concepts for dense spray combustion. *Combustion and Flame*, 144:558–577, 2006.

[73] M. Juniper, A. Tripathi, P. Scouflaire, J-C. Rolon, and S. Candel. The structure of cryogenic flames at elevated pressure. In *Proceedings of the 28th International Combustion Symposium*, volume 28, pages 1103–1109, 2000.

[74] N.L. Kafengauz and M.I. Federov. Excitation of high frequency pressure oscillations during heat exchange with diisopropylcyclohexane. *Inzhenerno-Fizicheskii Zhurnal*, 11(1):99–104, 1966.

[75] N.L. Kafengauz and M.I. Federov. Pseudoboiling and heat transfer in a turbulent flow. *Inzhenerno-Fizicheskii Zhurnal*, 14(6):923–924, 1968.

[76] S. Karl. *Numerical Investigation of a Generic Scramjet Configuration*. PhD thesis, University of Dresden, http://nbn-resolving.de/urn:nbn:de:bsz:14-qucosa-68695, 2011.

[77] T. Kim, Y. Kim, and S.-K. Kim. Numerical study of cryogenic liquid nitrogen jets at supercritical pressures. *The Journal of Supercritical Fluids*, 56:152–163, 2011.

[78] D.N. Klimenko, W. Clauss, M. Oschwald, J. Smith, and W. Mayer. CARS temperature mapping in a cryogenic LOX-H2 rocket combustion chamber under supercritical conditions. *Journal of Raman spectroscopy*, 33:900–905, 2002.

[79] O. Knab, M. Frey, J. Görgen, C. Maeding, K. Quering, and D. Wiedmann. Progress in combustion and heat transfer modelling in rocket thrust chamber applied engineering. In *Proceedings of the 45th AIAA/ASME/SAE/ASEE Joint Propulsion Conference and Exhibit*, Denver, USA, 2009. AIAA.

[80] W. Koschel. Raumfahrtantriebe. Vorlesungsskript, RWTH Aachen, 2002.

[81] K.K. Kuo. *Principles of Combustion (2nd Edition)*. Wiley, 2005.

[82] K.K. Kuo and R. Acharya. *Fundamentals of Turbulent and Multi-Phase Combustion*. Wiley, 2012.

[83] G. Lacaze and J.C. Oefelein. A non-premixed combustion model based on flame structure analysis at supercritical pressures. *Combustion and Flame*, 159(6):2087–2103, 2012.

[84] A. Laesecke, R. Krauss, K. Stephan, and W. Wagner. Transport properties of fluid oxygen. In P.J. Linstrom and W.G. Mallard, editors, *NIST Chemistry WebBook, NIST Standard Reference Database Number 69*. National Institute of Standards and Technology, Gaithersburg MD, 20899, http://webbook.nist.gov, (retrieved November 12, 2010)., 2013.

[85] G. Lamanna, E. Oldenhoff, S. Baab, I. Stotz, and B. Weigand. Disintegration regimes near the critical point. In *Proceedings of the 18th AIAA/3AF International Space Planes and Hypersonic Systems and Technologies Conference*, Tours, France, 2012.

[86] L.D. Landau and E.M. Lifschitz. *Statistische Physik*. Lehrbuch der theoretischen Physik. Akademie Verlag Berlin, 1966.

[87] J.C. Lasheras and E.J. Hopfinger. Liquid jet instability and atomization in a coaxial gas stream. *Annual Review of Fluid Mechanics*, 32:275–308, 2000.

[88] S. J. Laurence, S. Karl, J. Martinez Schramm, and K. Hannemann. Transient fluid-combustion phenomena in a model scramjet. *Journal of Fluid Mechanics*, 722:85–120, 2013.

[89] J.W. Leachman, R.T. Jacobsen, and E.W. Lemmon. Fundamental equations of state for parahydrogen, normal hydrogen, and orthohydrogen. In P.J. Linstrom and W.G. Mallard, editors, *NIST Chemistry WebBook, NIST Standard Reference Database Number 69*. National Institute of Standards and Technology, Gaithersburg MD, 20899, http://webbook.nist.gov, (retrieved November 12, 2010)., 2013.

[90] A.H. Lefebvre. *Atomization and Sprays*. Purdue University, West Lafayette, Indiana, 1989.

[91] E.W. Lemmon and R.T. Jacobsen. Viscosity and thermal conductivity equations for nitrogen, oxygen, argon, and air. *International Journal of Thermophysics*, 25(1):21–69, 2004.

[92] M. Lempke, P. Gerlinger, and M. Aigner. Assumed pdf modeling in rocket combustor simulations. *Progress in Propulsion Physics*, 4:569–582, 2013.

[93] S.P. Lin and R.D. Reitz. Drop and spray formation from a liquid jet. *Annual Review of Fluid Mechanics*, 30:85–105, 1998.

[94] P.J. Linstrom and W.G. Mallard, editors. *NIST Chemistry WebBook, NIST Standard Reference Database Number 69*, chapter http://webbook.nist.gov. National Institute of Standards and Technology, Gaithersburg MD, 20899, (retrieved 2013).

[95] M.-S. Liou. Ten years in the making - AUSM-family. In *Proceedings of the 15th Computational Fluid Dynamics Conference*, Anaheim, USA, 2001. AIAA.

[96] M.-S. Liou. A sequel to AUSM, part II: AUSM+ -up for all speeds. *Journal of Computational Physics*, 214:137–170, 2006.

[97] L. Liu, S.-H. Chen, A. Faraone, C.-W. Yen, and C.-Y. Mou. Pressure dependence of fragile-to-strong transition and a possible second critical point in supercooled confined water. *Physical Review Letters*, 95:117802–1 – 117802–4, 2005.

[98] A. Mack and V. Hannemann. Validation of the unstructured DLR-TAU-code for hypersonic flows. In *Proceedings of the 32nd AIAA Fluid Dynamics Conference and Exhibit*, number AIAA-2002-3111, 2002.

[99] M. Masquelet, S. Menon, Y. Jin, and R. Friedrich. Simulation of unsteady combustion in a LOX-GH2 fueled rocket engine. *Aerospace Science and Technology*, 13:466–474, 2009.

[100] H.-O. May and P. Mausbach. Riemannian geometry study of vapor-liquid phase equilibria and supercritical behavior of the Lennard-Jones fluid. *Physical Review E*, 85(031201), 2012.

[101] E. Mayer. Theory of liquid atomization in high velocity gas streams. *ARS Journal*, 31(12):1783–1785, 1961.

[102] W. Mayer. Coaxial atomization of a round liquid jet in a high speed gas stream: A phenomenological study. *Experiments in Fluids*, 16(6):401–410, 1994.

[103] W. Mayer. Test case RCM-1 - cryogenic injection. In O.J. Haidn, editor, *Proceedings of the 2nd International Workshop Rocket Combustion Modeling - Atomization, Combustion and Heat Transfer*, Lampoldshausen, Germany, 2001.

[104] W. Mayer, B. Ivancic, A. Schik, and U. Hornung. Propellant atomization and ignition phenomena in liquid oxygen/gaseous hydrogen rocket combustors. *Journal of Propulsion and Power*, 17:794–799, 2001.

[105] W. Mayer, A. Schik, V. Vielle, C. Chauveau, I. Gökalp, D. G. Talley, and R. D. Woodward. Atomization and breakup of cryogenic propellants under high-pressure subcritical and supercritical conditions. *Journal of Propulsion and Power*, 14:835–842, 1998.

[106] W. Mayer and J. Smith. Fundamentals of supercritical mixing and combustion of cryogenic propellants. In V. Yang, M. Habiballah, J. Hulka, and M. Popp, editors, *Progress in Astronautics and Aeronautics: Liquid Rocket Thrust Chamber: Aspects of Modeling, Analysis, and Design*. AIAA, 2004.

[107] W. Mayer and H. Tamura. Propellant injection in a liquid oxygen/gaseous hydrogen rocket engine. *Journal of Propulsion and Power*, 12(6):1137–1147, 1996.

[108] W. Mayer, J. Telaar, R. Branam, G. Schneider, and J. Hussong. Characterization of cryogenic injection at supercritical pressures. In *Proceedings of the 37th AIAA/ASME/ASEE Joint Propulsion Conference and Exhibit*, number AIAA 2001-3275, Salt Lake City, 2001. AIAA.

[109] W. Mayer, J. Telaar, R. Branam, G. Schneider, and J. Hussong. Raman measurements of cryogenic injection at supercritical pressure. *Heat and Mass Transfer*, 39, 2003.

[110] B.J. McBride and S. Gordon. Computer program for calculation of complex chemical equilibrium compositions and applications. *NASA Reference Publication*, 1311, 1996.

[111] P.F. McMillan and H.E. Stanley. Going supercritical. *Nature Physics*, 6:479–480, 2010.

[112] H. Müller, C.A. Niedermeier, M. Jarczyk, M. Pfitzner, S. Hickel, and N.A. Adams. Large eddy simulations of trans- and supercritical injection. In *Proceedings of the EUCASS Conference*, Munich, Germany, 2013.

[113] E.P. Muntz. *Rarefied Gas Dynamics*, volume 2, chapter The direct measurement of velocity distribution functions. Academic Press, 1966.

[114] J.A. Newman and T.A. Brzustowski. Behavior of a liquid jet near the thermodynamic critical region. *AIAA Journal*, 9(8):1595–1602, 1971.

[115] C.A. Niedermeier, M.M. Jarczyk, S. Hickel, N. Adams, and M. Pfitzner. Large-eddy simulation of turbulent trans- and supercritical mixing. In *Proceedings of the 21st AIAA Computational Fluid Dynamics Conference*, number AIAA 2013-2950, San Diego, USA, 2013. AIAA.

[116] J.C. Oefelein. Thermophysical characteristics of shear-coaxial LOX–H2 flames at supercritical pressure. *Proceedings of the Combustion Institute*, 30(2):2929–2937, 2005.

[117] J.C. Oefelein. Mixing and combustion of cryogenic oxygen-hydrogen shear-coaxial jet flames at supercritical pressure. *Combustion Science and Technology*, 178:229–252, 2006.

[118] J.C. Oefelein and S.K. Aggarwal. Towards a unified high-pressure drop model for spray simulations. In *Proceedings of the Summer Program*. Stanford Center for Turbulence Research, 2000.

[119] J.C. Oefelein and V. Yang. Modeling high-pressure mixing and combustion processes in liquid rocket engines. *Journal of Propulsion and Power*, 14(5):843–857, 1998.

[120] K. Okamoto, J. Ota, K. Sakurai, and H. Madarame. Transient velocity distributions for the supercritical carbon dioxide forced convection heat transfer. *Journal of Nuclear Science*, 40(10):763–767, 2003.

[121] N. Okong'o and J. Bellan. Direct numerical simulation of O2/H2 temporal mixing layers under supercritical conditions. *AIAA Journal*, 40:914–926, 2002.

[122] N. Okong'o and J. Bellan. Real-gas effects on mean flow and temporal stability of binary-species mixing layers. *AIAA Journal*, 41(12):2429–2443, 2003.

[123] N. Okong'o and J. Bellan. Turbulence and fluid-front area production in binary-species, supercritical, transitional mixing layers. *Physics of Fluids*, 16(5):1467–1492, 2004.

[124] M. Oschwald and M.M. Micci. Spreading angle and centerline variation of density of supercritical nitrogen jets. *Atomization and Sprays*, 11:91–106, 2002.

[125] M. Oschwald, J.J. Smith, R. Branam, J. Hussong, A. Schik, B. Chehroudi, and D. Talley. Injection of fluids into supercritical environments. *Combustion Science and Technology*, 178:49–100, 2006.

[126] D.-Y. Peng and D.P. Robinson. A new two-constant equation of state. *Industrial & Engineering Chemistry Fundamentals*, 15(1):59–64, 1976.

[127] N. Peters. *Turbulent Combustion*. Cambridge, 2000.

[128] A. Pfennig. *Thermodynamik der Gemische*. Springer, 1st edition, 2003.

[129] T. Poinsot and D. Veynante. *Theoretical and Numerical Combustion*. R.T. Edwards, 2005.

[130] P.H. Poole, F. Sciortino, U. Essmann, and H.E. Stanley. Phase behaviour of metastable water. *Nature*, 360:324–328, 1992.

[131] M.-M. Poschner and M. Pfitzner. Real gas CFD simulation of supercritical H2-LOX combustion in the Mascotte single-injector combustor using a commercial CFD code. In *Proceedings of the 46th AIAA Aerospace Sciences Meeting and Exhibit*, Reno, USA, 2008. AIAA.

[132] M.-M. Poschner and M. Pfitzner. CFD-simulations of supercritical LOX/GH2 combustion considerin g consistent real-gas thermodynamics. In *Proceedings of the European Combustion Meeting*, 2009.

[133] M. Pourouchottamane, F. Dupoirieux, and M. Habiballah. Cryogenic dense spray modeling using an interface density equation. In *Proceedings of the 37th AIAA/ASME/SAE/ASEE Joint Propulsion Conference and Exhibit*, number AIAA 2001-3273, Salt Lake City, USA, 2001.

[134] Lord Rayleigh. On the instability of jets. *Proceedings of the London Mathematical Society*, 10(4), 1878.

[135] O. Redlich and J.N.S. Kwong. On the thermodynamics of solutions. *Chemical Review*, 44(1):233–244, 1949.

[136] H. Rehab, E. Villermaux, and E.J. Hopfinger. Flow regimes of large-velocity-ratio coaxial jets. *Journal of Fluid Mechanics*, 345:357–381, 1997.

[137] R.D. Reitz and F.B. Bracco. On the dependence of spray angle and other spray parameters on nozzle design and operating conditions. In *Proceedings of the SAE*, Detroit, USA, 1979. SAE.

[138] C.-C. Rossow. Extension of a compressible code toward the incompressible limit. *AIAA Journal*, 41(12):2379–2386, 2003.

[139] G. Ruppeiner, A. Sahay, T. Sarkar, and G. Sengupta. Thermodynamic geometry, phase transitions, and the Widom line. *Physical Review E*, 86:052103–1 – 052103–4, 2012.

[140] M. Santoro and F.A. Gorelli. Structural changes in supercritical fluids at high pressures. *Physical Review B*, 77:212103–1 – 212103–4, 2008.

[141] C.-A. Schley, G. Hagemann, P. Tucker, S. Venkateswaran, and C. Merkle. Comparison of computational codes for modeling hydrogen-oxygen injectors. In *Proceedings of the 33rd AIAA/ASME/SAE/ASEE Joint Propulsion Conference and Exhibit*, Seattle, USA, 1997. AIAA.

[142] R. Schmidt and W. Wagner. A new form of the equation of state for pure substances and its application to oxygen. In P.J. Linstrom and W.G. Mallard, editors, *NIST Chemistry WebBook, NIST Standard Reference Database Number 69*. National Institute of Standards and Technology, Gaithersburg MD, 20899, http://webbook.nist.gov, (retrieved November 12, 2010)., 2013.

[143] T. Schmitt, J. Rodriguez, I.A. Leyva, and S. Candel. Experiments and numerical simulation of mixing under supercritical conditions. *Physics of Fluids*, 24:055104–1 – 055104–29, 2012.

[144] T. Schmitt, L. Selle, B. Cuenot, and T. Poinsot. Large-eddy simulation of transcritical flows. *Comptes Rendus Mecanique*, 337:528–538, 2009.

[145] T. Schmitt, L. Selle, A. Ruiz, and B. Cuenot. Large-eddy simulation of supercritical-pressure round jets. *AIAA Journal*, 48(9):2133–2144, 2010.

[146] F. Sciortino, P.H. Poole, U. Essmann, and H.E. Stanley. Line of compressibility maxima in the phase diagram of supercooled water. *Physical Review E*, 55(1):727–737, 1997.

[147] G.G. Simeoni, T. Bryk, F.A. Gorelli, M. Krisch, G. Ruocco, M. Santoro, and T. Scopigno. The Widom line as the crossover between liquid-like and gas-like behaviour in supercritical fluids. *Nature Physics*, 6:503–507, 2010.

[148] J. Smith, G. Schneider, D. Suslov, M. Oschwald, and O. Haidn. Steady-state high pressure LOX/H2 rocket engine combustion. *Aerospace Science and Technology*, 11:39–47, 2007.

[149] G. Soave. Equilibrium constants from a modified Redlich-Kwong equation of state. *Chemical Engineering Science*, 27:1197–1203, 1972.

[150] P.R. Spalart and S.R. Allmaras. A one-equation turbulence model for aerodynamic flows. *AIAA Paper*, (92-0439), 1992.

[151] R. Span, E.W. Lemmon, R.T. Jacobsen, W. Wagner, and A. Yokozeki. A reference equation of state for the thermodynamic properties of nitrogen for temperatures from 63.151 to 1000 k and pressures to 2200 mpa. In P.J. Linstrom and W.G. Mallard, editors, *NIST Chemistry WebBook, NIST Standard Reference Database Number 69*. National Institute of Standards and Technology, Gaithersburg MD, 20899, http://webbook.nist.gov, (retrieved November 12, 2010)., 2010.

[152] R. Span, E.W. Lemmon, R.T. Jacobsen, W. Wagner, and A. Yokozeki. A reference equation of state for the thermodynamic properties of nitrogen for temperatures from 63.151 to 1000 k and pressures to 2200 mpa. In P.J. Linstrom and W.G. Mallard, editors, *NIST Chemistry WebBook, NIST Standard Reference Database Number 69*. National Institute of Standards and Technology, Gaithersburg MD, 20899, http://webbook.nist.gov, (retrieved November 12, 2010)., 2013.

[153] H.E. Stanley. *Introduction to Phase Transitions and Critical Phenomena*. Oxford University Press, 1971.

[154] I. Stotz, G. Lamanna, and B. Weigand. Fluid disintegration studies in a specialized shock tube. *Progress in Propulsion Physics*, 2:165–206, 2011.

[155] G. P. Sutton and O. Biblarz. *Rocket Propulsion Elements (7th Edition)*. Wiley, 2001.

[156] G.I. Taylor. *Collected Works of G.I. Taylor, Vol. 3*, chapter Generation of ripples by wind blowing over a viscous fluid. Cambridge University Press, 1940.

[157] C. Tegeler, R. Span, and W. Wagner. A new equation of state for argon covering the fluid region for temperatures from the melting line to 700 k at pressures up to 1000 mpa. In P.J. Linstrom and W.G. Mallard, editors, *NIST Chemistry WebBook, NIST Standard Reference Database Number 69*. National Institute of Standards and Technology, Gaithersburg MD, 20899, http://webbook.nist.gov, (retrieved November 12, 2010)., 2013.

[158] E.F. Toro. *Riemann Solvers and Numerical Methods for Fluid Dynamics: A Practical Introduction*. Springer, 3rd edition, 2009.

[159] A. Tripathi. *Modélisation de la combustion cryotechnique à haute pression*. PhD thesis, Ecole Centrale Paris, 2001.

[160] P.K. Tucker, S. Menon, C.L. Merkle, J.C. Oefelein, and V. Yang. Validation of high-fidelity CFD simulations for rocket injector design. In *Proceedings of the 44th AIAA/ASME/SAE/ASEE Joint Propulsion Conference & Exhibit*, Hartford, USA, 2008. AIAA.

[161] J.D. van der Waals. *Over de Continuiteit van den Gas- en Vloeistoftoestand*. PhD thesis, University of Leiden, 1873.

[162] Bram van Leer. Towards the ultimate conservation difference scheme. V. A second-order sequel to godunov's method,. *Journal of Computational Physics*, 32(1):101– 136, 1979.

[163] E. Villermaux. Mixing and spray formation in coaxial jets. *Journal of Propulsion and Power*, 14:807–817, 1998.

[164] L. Vingert, A. Nicole, and M. Habiballah. Test case RCM-2, Mascotte single injector. In *Proceedings of the 3rd International Workshop on Rocket Combustion Modeling*, Vernon, France, 2006.

[165] W. Wagner and A. Pruss. The iapws formulation 1995 for the thermodynamic properties of ordinary water substance for general and scientific use. In P.J. Linstrom and W.G. Mallard, editors, *NIST Chemistry WebBook, NIST Standard Reference Database Number 69*. National Institute of Standards and Technology, Gaithersburg MD, 20899, http://webbook.nist.gov, (retrieved November 12, 2010)., 2013.

[166] J. Warnatz, U. Maas, and R.W. Dibble. *Combustion*. Springer, 4th edition, 2006.

[167] B. Weigand, J. Köhler, and J.v. Wolfersdorf. *Thermodynamik kompakt*. Springer, 2008.

[168] D. Wennerberg and O. Knab. Effective calculation of multiphase flow fields in liquid rocket thrust chambers. In *Proceedings of the 37th AIAA/ASME/SAE/ASEE Joint Propulsion Conference and Exhibit*, Salt Lake City, USA, 2001. AIAA.

[169] C.R. Wilke. A viscosity equation for gas mixtures. *Journal of Chemical Physics*, 18:517–519, 1950.

[170] R.D. Woodward and D.G. Talley. Raman imaging of transcritical cryogenic propellants. In *Proceedings of the 34th AIAA Aerospace Sciences Meeting and Exhibit*, number AIAA 96-0468, Reno, 1996. AIAA.

[171] M Wörner. A compact introduction to the numerical modeling of multiphase flows. Technical report, Forschungszentrum Karlsruhe, 2003.

[172] L. Xu, P. Kumar, S.V. Buldyrev, S.-H. Chen, P.H. Poole, F. Sciortino, and H.E. Stanley. Relation between the Widom line and the dynamic crossover in systems with a liquid–liquid phase transition. *Proceedings of the National Academy of Sciences of the USA*, 102(46):16558–16562, 2005.

[173] V. Yang. Modeling of supercritical vaporization, mixing, and combustion processes in liquid-fueled propulsion systems. *Proceedings of the Combustion Institute*, 28:925–942, 2000.

[174] V. Yang, M. Habiballah, J. Hulka, and M. Popp, editors. *Progress in Astronautics and Aeronautics: Liquid Rocket Thrust Chamber: Aspects of Modeling, Analysis, and Design*. AIAA, 2004.

[175] V. Yang, N.N. Lin, and J.S. Shuen. Vaporization of liquid oxygen (LOX) droplets in supercritical hydrogen environments. *Combustion Science and Technology*, 97(4-6):247–270, 1994.

[176] B. A. Younglove. Thermophysical properties of fluids. I. argon, ethylene, parahydrogen, nitrogen, nitrogen trifluoride, and oxygen. *Journal of Physical and Chemical Reference Data*, 11:Supplement 1, 1982.

[177] L. Zipperer and F. Herning. Beitrag zur Berechnung der Zähigkeit technischer Gasgemische aus den Zähigkeitswerten der Einzelbestandteile. *Das Gas- und Wasserfach*, 4:49ff, 1936.

[178] N. Zong, H. Meng, and V. Yang. Numerical study of cryogenic fluid injection and mixing under supercritical conditions. *Physics of Fluids*, 16(12):4248–4261, 2004.

[179] N. Zong and V. Yang. Cryogenic fluid jets and mixing layers in transcritical and supercritical environments. *Combustion Science and Technology*, 178:193–227, 2006.

[180] S. Zurbach, editor. *Proceedings of the 3rd International Workshop Rocket Combustion Modeling - Atomization, Combustion and Heat Transfer*. Vernon, France, 2006.